SCUOLA DOTTORALE IN GEOLOGIA DELL'AMBIENTE E DELLE RISORSE

DOTTORATO IN GEOLOGIA DELL'AMBIENTE E GEODINAMICA

CICLO DEL CORSO DI DOTTORATO XXXII

Degree of Doctor of Philosophy in Earth Science

An integrated paleomagnetic, rock magnetic, anisotropy of magnetic susceptibility, stratigraphic and structural study of Miocene synorogenic red beds from NW Iran: Insight into the geologic evolution of the intermontane Tarom Basin at the linkage between the western Alborz Mountains and the northern margin of the Iranian Plateau

Mohammad Paknia

Supervisor: Prof. Paolo Ballato

Co-Supervisor:

Prof. Massimo Mattei

Coordinator:

Prof. Paola Tuccimei

Collaborators:

Prof. Jamshid Hassanzadeh

Dr. Ghasem Heidarzadeh

Prof. Francesca Cifelli

Prof. Joshua Feinberg

Prof. Mike Jackson

Prof. Bruce Moskowitz

Dr. Dario Bilardello

Prof. Andy Wickert

Prof. Majid Mirzaee Ataabadi

Prof. Mohammad Reza Ghassemi

Prof. Jamshid Hassanzade: Division of Geological & Planetary Sciences, California Institute of Technology Pasadena, Pasadena, CA, USA

Dr. Ghasem Heidarzadeh: Institute of Earth and Environmental Sciences, University of Potsdam, Potsdam, Germany

Prof. Francesca Cifelli: Department of Science, University of Roma Tre, Rome, Italy

Prof. Joshua Feinberg, Prof. Mike Jackson, Prof. Bruce Moskowitz, Dr. Dario Bilardello:

Institute for Rock Magnetism, University of Minnesota, USA

Prof. Andy Wickert: Department of Earth and Environmental Sciences, University of Minnesota, USA

Prof. Majid Mirzaee Ataabadi: Department of Geology, Faculty of Science, University of Zanjan, Iran

Prof. Mohamamd Reza Ghassemi: Research Institute for Earth Sciences, Geological Survey of Iran, Tehran, Iran

Reviewers:

Prof. Miguel Garces

Faculty of Earth Sciences, University of Barcelona, Email Address: mgarces@ub.edu

Prof. Giovanni Vezzoli

Department of Earth and Environmental Sciences, University of Milano-Bicocca, Milan, Italy
Email address: giovanni.vezzoli@unimib.it

Abstract

Sedimentary basins represent first-order geological archives that can provide information on the evolution of the sediment source regions, the growth and the erosional history of adjacent topography, as well as the evolution of the depositional settings and the paleoenvironmental conditions. Sedimentary basin can be found in diverse geodynamic settings including continental collision zones, where they can host thick piles of sediments deposited over time scales of 10^5 to 10^7 years. This comprises foreland areas, orogenic plateaus interiors and intermontane areas at the transition between the plateau and its foreland, or within mountain belts. In this study, I focus on the intermontane Tarom Basin at the transition between the Iranian Plateau (IP) and Alborz Mountains. This basin was filled with synorogenic red beds that allow investigating puzzling aspects of this region such as the timing and mechanisms of basin development, and the growth of the adjacent plateau margin and Alborz Mountains.

To tackle this issue, I performed an integrated paleomagnetic, rock magnetic, anisotropy of magnetic susceptibility (AMS), geochronologic, magnetostratigraphic, structural, sedimentologic, and sediment provenance analysis on three major sedimentary sections exposed in the Tarom Basin. This approach allowed documenting for the first time the termination of arc volcanism in this region at 38-36 Ma, an age for the synorogenic red beds of ~16.5 to 7.6 Ma, the occurrence of an early stage of Late Eocene deformation followed by higher magnitude of deformation at least from ~16.5 Ma, a complex evolution of the drainage system with several episodes of efficient and reduced to absent fluvial connectivity with the Caspian Sea, changes in the depositional setting and in the sediment source area or in the sediment routing system, the occurrence of post 7.6 Ma intrabasinal deformation event which had a localized impact in the magnetic fabric of sediments and finally, the recognition of localized Middle-Late Miocene orogen perpendicular extension, which was most likely caused by gravitational instability of the basin margin rather than regional lithospheric stretching. Overall, my data indicate that the northern basin margin accommodated a greater magnitude of deformation and exhumation than the southern one, which experienced limited deformation and erosional exhumation and hence must have been uplifted via deep-seated processes. Finally, my data suggest that the Tarom Basin cannot have been an integral part of the IP because my results does not indicate the presence of a formerly elevated basin likewise in the plateau interior.

Acknowledgements

First and foremost, I thank the almighty God for giving me the strength, ability and opportunity to complete my PhD study.

My sincere gratitude goes to my MSc teachers and colleagues at the plaeomagnetic laboratory and Institute for Earth sciences at the Geological Survey of Iran (GSI); Habib Alimohamadian, Mohammad Reza Ghasemi, Mahmoud Reza Majidifard, Jafar Sabury, Morteza Talebian, who educated and inspired me in geo-science researches.

My special thanks to a friend and colleague of mine Majid Mirzaei Ataabadi (university of Zanjan) for encouraging and helping me to apply as a visiting scholar at the University of Helsinki after my MSc studies. I also want to express my gratitude to Anu Kaakinen and Johanna Salminen for involving me in their paleomagnetic research team during my visit of Helsinki University.

I am so grateful and deeply indebted to my advisor Paolo Ballato for everything I’ve learnt from him during my PhD studies at the University of Roma Tre. I am very grateful for all his encouragement to carry out this multidisciplinary exiting research, for providing every possible opportunity to freely pursue my interests and the freedom that he's given me to explore a wide range of problems. I warmly and deeply thank of him and shall never forget the enormous time and patience he spent on mentoring and training me.

Many thanks to my co-supervisors Massimo Mattei and Francesca Cifelli. I highly appreciate them for sharing their expertise, time and guidance in this study.

I also wish to thank my thesis reviewers, Miguel Garcés Sen and Giovanni Vezzoli for their encouraging comments and nice reports.

I would like to thank of my fellow colleagues, post-docs, PhD students in Roma Tre University, as well as good people in university research office and PhD coordinators who have always been kind and helpful to me.

I would like to thank a big community of my new Iranian, Italian and other new international friends I’ve met in Italy for being helpful on many occasions and shearing my great times.

I am grateful to Aldo Winkler and Chiara Caricchi for their help in the paleomagentic laboratory in National Institute of Geophysics and Volcanology (INGV) of Italy.

I warmly thank of scientists at the University of Torino, University of Milano and Alpine Paleomagnetic laboratory (ALP) members for their support in the lab; Elena Zanella, Evdokia Tema, Giovanni Muttoni, Matteo Maron and thanks to manager of Formont Institute in Peveragno Laura Cavallera and all good people work in this institute to their hospitality during my visit and lab work

I would like to thank Giovanni Vezzoli, Sergio Ando, Alberto, Marta and Maria in the laboratory of sedimentary provenance at the University of Milano-Bicocca, Italy for their help and providing me facilities for doing petrography analysis.

I also would like to thank the Institute for Rock Magnetism (IRM) members at the University of Minnesota, USA. Josh Feinberg, Mike Jackson, Bruce Moskowitz, Dario Bilardello, Peat Solheid and all graduate students and post-docs in the department for shearing their knowledge and experiences, I have benefitted very much from their patient explanations and insights into my work. The Institute for Rock Magnetism has been a wonderful academic during my PhD and I am lucky to have been surrounded by such a collection of estimable colleagues there.

A very special thanks to Andy Wickert and Gene-Hua Crystal Ng for housing me in their beautiful house during my stay in Minneapolis, USA.

I appreciate the financial support from University of Roma Tre which enabled me to live and study for the past more than 3 years in Italy, two months field work in Iran, to participate in national/international conferences, courses, and to conduct research abroad Germany, Austria, and USA.

Many thanks to my Iranian friends Ghasem Hydarzadeh, Meysam Tadayon, and driver Hasan sharifi for their help in the field work.

And finally, I would like to thank of my dear parents, my dear sisters and other family members for their loving support, cheering me on along the way and guidance as I worked to achieve my goals. No words to describe my feelings to them. I dedicate this thesis to them and to the people of Iran.

Table of Contents

……..

Chapter 1: Introduction

Paleomagnetism is a paramount tool in the study of sedimentary rocks that allows constraining the history of the Earth's magnetic field and the evolution of the Earth surface. Specifically, sedimentary rocks provide a nearly continuous record of the geomagnetic field and its intensity. This can be used for age determination, paleolatitude reconstruction, tectonic rotations and consequently for tracking geodynamic processes through time. The reversal in magnetic polarity is considered one of the most distinctive properties of the Earth's magnetic field (see Langereis et al, 2010). The occurrence of a characteristic pattern of reversals in a sedimentary succession allows relative dating by comparing such a pattern with a well-established geomagnetic polarity time scale (magnetostratigraphy). Furthermore, magnetostratigraphic dating allows estimating sediment accumulation rates in sedimentary basins and infer phases of tectonic deformation (Merrill et al. 1996; Dupont-Nivet & Krijgsman, 2012). At the same time, the study of the magnetic mineralogy and the characteristics of magnetic minerals forming sedimentary rocks (e.g., magnetic domain grain size) represents a valuable proxy for reconstructing paleoenvironmental conditions (Paleomagnetism of sedimentary rocks; Kodama, 2012), and also for detecting changes in the sediment source area or the sediment routing system (e.g, Charreau et al., 2005). Another important method is the anisotropy of the magnetic susceptibility (AMS), which allows constraining the strain pattern and the degree of deformation of sedimentary rocks or unconsolidated sediments in different tectonic settings (e.g. Saint-Bezar et al. 2002; Pares 2004; Robion et al. 2007). This method can also be used to measure shape anisotropy changes as well as bulk-preferred orientation of different magnetic minerals (Hrouda 1982; Borradaile, 1988; Tarling and Hrouda 1993; Borradaile and Henry, 1997; Borradaile, 2001; Soto et al., 2009), and hence can provide first other information on lithogenetic (sedimentation and diagenesis) processes. The combination of paleomagnetism, environmental magnetism and AMS with structural and sedimentologic data allows establishing a relative chronology between sedimentation, acquisition of a magnetic fabric patterns of a magnetic remanence and finally on deformation processes (e.g. Larrasoaña et al., 2004).

Orogenic plateaus are morphotectonic provinces consisting of sedimentary basins that have coalesced and filled with thick sedimentary deposits. These basins retain insights into orogenic, sedimentary erosional and geodynamic processes (e.g., Alonso et al, 1990; Meyer et al., 1998; Sobel et al., 2003; Carrol et al., 2010, Strecker et al., 2009; Pingel et al., 2019). The orogenic Iranian Plateau (IP) is one of the best modern examples of a high plateau in a continental collision zone. The IP is NW-SE-oriented, is mainly located on the upper plate of the Arabia-Eurasia collision zone and represent the second collisional plateau in elevation and size after Tibet (see Hatzfeld and Molnar, 2010 for a comparison). The IP is parallel to the Zagros orogenic belt and is characterized by high elevation (average elevation is ~1800 m), low internal topographic relief (few hundred of meters), dry climatic conditions and endorheic sedimentary basins in its interior (four out of six basins are internally drained), and steep and dissected flanks bounded by major reverse faults (Ballato et al., 2013, 2017 Heidarzadeh et al., 2017). In central Iran, the northern margin of the IP is marked by a sharp boundary with the adjacent foreland, which comprises the rigid Central Iranian Block. In NW Iran, the IP approaches the Caspian Sea and it is separated from the intracontinental Alborz and Talesh mountains by an elongated, NW-SE oriented intermontane basin (Tarom Basin). Currently, this basin is drained by the Qezel-Owzan River, the second largest river in Iran that flows from the interior of the IP to the Caspian Sea. The Tarom Basin is at lower elevation than the adjacent Iranian Plateau although in the past it may have been integrated in the IP during phases of internal drainage conditions as suggested in similar basins in the central Andes (broken foreland of NW Argentina, e.g., Strecker et al., 2009). Importantly, the basin is composed of post Eocene, synorogenic red beds that offer the unique opportunity to investigate puzzling aspects of this collision zone, such as the timing and mechanisms of plateau margin uplift, its lateral extension and the link with the adjacent growing Alborz Mountains.

In this thesis, I have performed a multidisciplinary study of the Tarom Basin synorogenic deposits of unknown age (deposition must have occurred any time after Eocene) to better understand the tectono-stratigraphic evolution as well as the paleoenvironmental conditions in this intermontane basins, which is located in a crucial sector of the Arabia-Eurasia collision zone. The methods I used in this study include:

1) A sedimentologic study that provides the basis for an assessment of the depositional environments.

2) A geochronologic study (U-Pb on zircons) of the uppermost volcanics of the Karaj Formation to constrain the termination age of Eocene arc volcanism as well as the age of red beds to provide pinpoints for magnetostratigaphic correlations.

3) A magnetostratigraphic analysis to establish a detailed chronostratigraphic framework for the red beds.

4) A study of the anisotropy of the magnetic susceptibility (AMS) to gain insights into the magnetic fabrics and its linkage with lithogenetic and deformation processes.

5) A fault kinematic analysis of the numerous synsedimentary normal faults observed in the field to constrain the orientation of the paleostress axis at the time of deposition.

6) Rock magnetic measurements to characterize the magnetic mineralogy, the main magnetic properties of the magnetic particles, and the stability of magnetic remanence.

7) A provenance study based on sandstone petrography

Detailed information about the analytical methods will be provided in the following sections and the appendix

The results and conclusions are subdivided into three chapters that are presented in form of manuscripts to be submitted to peer-reviewed journals soon.

In chapter 2, I establish for the first time a chronologic setting for the intermontane Tarom Basin by combining a geochronology (U-Pb on zircons) with magnetostratigraphy for the last 38-36 Ma. Furthermore, I characterize the depositional environments and the sediment provenance during the last 16 Ma. The results allow understanding the tectono-stratigraphic evolution of this intermontane basin and identify the erosional history of its sediment source area.

In chapter 3, I combine an AMS study of the Miocene red beds of the intermontane Tarom Basin with a fault kinematic analysis of synsedimentary normal faults observed in the field. The results allow comparing the magnetic fabrics of the red beds from different sectors of the basin, and investigating their relationship with tectonic deformation and depositional processes.

In chapter 4 a collection of rock magnetic measurements including different type of experiments such as is presented. The work presented in this chapter is still at its preliminary stage because the results were acquired only recently. The aim of this chapter is to study the magnetic properties of the red beds in order to identify the magnetic mineralogy, the size and concentration of magnetic grains. These results will be used as proxies to unravel changes in environmental processes and in the sediment source area and will be combined with paleoclimate analysis that are still in progress (Carbon and Oxygen stable isotopes on paleosols and lacustrine marls).

Chapter 2: Magnetostratigraphy, sedimentology and provenance analysis of Miocene red beds in the intermontane Tarom Basin: insights into the evolution of the Alborz Mountains and the Iranian Plateau at the northern margin of the Iranian Plateau

Abstract

I study the intermontane Tarom Basin at the transition between the Iranian Plateau (IP) to the SW and the Alborz Mountains to the NE to decipher the tectono-stratigraphic evolution of this sector of the Arabia-Eurasia collision zone. The investigation of the basin-fill deposits is crucial for constraining the evolution of the north-western IP margin (Tarom range), which is mainly composed of Eocene volcanic of the Karaj Formation. Furthermore, it allows exploring the connection with the adjacent Alborz Mountains, which consist of metamorphic, sedimentary and volcanic rocks of different age.

To achieve these goals, I have performed a magnetostratigraphic, sedimentologic, geochronologic (zircon U-Pb) and sediment provenance (sandstone petrography) analysis on three stratigraphic sections exposed along the southern basin margin (TV and KA sections) and in proximity of its central sectors (GH section). This integrated study allows reconstructing different depositional environments, dating the basin -fill deposits, and documenting erosional exhumation processes in the adjacent mountain ranges. In particular, I show that the top of Karaj Formation has an age of ∼38-36 Ma and is overlain by unconformable red beds indicating an early episode of uplift and deformation right after the termination of Eocene volcanism. Sedimentation in the basin resumed from ∼16.5 Ma (base of TV section) with the establishment of internal drainage conditions, most likely as flexural response to tectonic loading from the adjacent uplifting mountain ranges. Sediments deposition lasted at least until ∼7.6 Ma (top of GH section), suggesting that these red beds are stratigraphically equivalent to deposition of middle-late of the Upper Red Formation (URF). Sedimentation occurred at nearly uniform rates with a sharp increase at ~12.1 Ma and few additional episodes of acceleration that may reflect thrust loading during enhanced shortening phases along the basin margins. Sometime after ~7.6 Ma, the basin was reintegrated into an external drainage system with the establishment of a new fluvial connection with the Caspian Sea. This appears to coincide with intrabasinal deformation, basin uplift, and erosion. Subsequently, the basin experienced new shorter episodes of basin filling and incision as documented by the occurrence of Pliocene

conglomerate as well as, at least three Quaternary terrace conglomerates. The combination of these observations with sandstone petrography data, further suggests that the northern margin of the basin (Alborz Mountains) experienced a greater magnitude of deformation and exhumation than the southern one (Tarom range), and hence accommodated a larger fraction of plate convergence. This implies that uplift of the Tarom range and hence the plateau margin must have been triggered by mantle driven processes rather than shortening and thickening processes. Finally, the Tarom Basin could not be an integral part of the IP because my results do not indicate the presence of a formerly elevated basin likewise the plateau interior.

1. Introduction

Orogenic plateaus are vast and elevated morphotectonic provinces, which provide the unique opportunity to decipher the interplay between shallow, deep-seated and surface processes, and their influences on Earth's landscape at various timescales (e.g., Dewey et al., 1988; Isacks, 1988; Molnar et al., 1993). They contain internally drained basins that have coalesced and filled with thick sedimentary deposits and hence retain insights into orogenic, erosional and geodynamic processes (e.g., Alonso et al, 1990; Meyer et al., 1998; Sobel et al., 2003; Carrol et al., 2010, Strecker et al., 2009; Pingel et al., 2019). Plateau's building models predict that the combination of reduced fluvial connectivity and outward propagation of the deformation fronts produce a lateral (orogen perpendicular) expansion through the integration of new sectors of the foreland into the plateau realm (Sobel et al., 2003; Garcia Castellanos et al., 2007). The application of these models, however, is not straightforward because the interplay between tectonic and surface processes may trigger different scenarios such as basin excavation and erosion with the destruction of the typical plateau morphology (e.g., Strecker et al., 2009; Heidarzadeh et al., 2019). Therefore, while the sedimentary basins in the plateau interior are stable over time scales of few 10^7 years (e.g., Alonso et al, 1990; Bush et al., 2016) intermontane basin at the transition with the foreland may experience a more complex evolution including several episodes of basin-filling and incision at shorter time scales (10^5 to few 10^6 years; e.g., Streit et al., 2015; Schildgen et al., 2016; Tofelde et al., 2017; Pingel et al., 2019). Importantly, these transitional basins hold precious information not only on the growth of the plateau margin but also on the evolution of the adjacent mountain ranges.

The NW-SE-oriented Iranian Plateau (IP) is mainly located on the upper plate of the Arabia-Eurasia collision zone and represent the second collisional plateau in elevation and size after Tibet (see Hatzfeld and Molnar, 2010 for a comparison). The IP is parallel to the Zagros orogenic belt and is characterized by high elevation (average elevation is ~1800 m), low internal topographic relief (few hundred of meters), dry climatic conditions and endorheic sedimentary basins in its interior (six out of eight basins are internally drained), and steep and dissected flanks bounded by major reverse faults (Ballato et al., 2013, 2017 Heidarzadeh et al., 2017). In central Iran, the northern margin of the IP is marked by a sharp boundary with the adjacent foreland, which comprises the rigid Central Iranian Block (Fig. 1). In NW Iran, the IP approaches the Caspian Sea and it is separated from the intracontinental Alborz and Talesh Mountains by an elongated, NW-SE oriented intermontane basin (Tarom Basin). Currently, this basin is drained by the Qezel-Owzan River, the second largest river in Iran that flows from the interior of the IP to the Caspian Sea. The basin is composed of post Eocene, synorogenic red beds that offer the opportunity to investigate puzzling aspects of this collision zone, such as the timing and mechanisms of plateau margin uplift, its lateral extension and the link with the adjacent growing Alborz Mountains.

For this purpose, I have performed a multidisciplinary study including the characterization of the depositional environments, of the sediment provenance areas and the depositional age of these post Eocene synorogenic red beds. Magnetostratigraphic analysis and new zircon U-Pb ages, document that the widespread Eocene arc volcanism terminated at ∼ 38-36 Ma, while the deposition of the red beds occurred from ∼16.5 Ma to at least 7.6 Ma. I then highlight that the timing of basin formation is associated with the development of internal drainage conditions triggered by the topographic growth of the fault-bounded Tarom (the plateau margin) and Alborz ranges (Fig. 1). Further, I document the occurrence of an alternation of periods of efficient and limited fluvial connectivity and I conclude that there are no evidences showing that this basin may have been an integral part of the plateau before its fluvial integration to the Caspian Sea. Finally, I infer that uplift in the IP margin in this area must have been triggered by deep seated processes rather than crustal shortening and thickening.

2. Geologic setting

The Tarom Basin is a NW-SE oriented, elongated, intermontane basin located along the northern margin of the Iranian Plateau between the western Alborz Mountains to the NE, and the Tarom range to the SW, within the Arabia-Eurasia collision zone (Figs. 1 and 2).

The western Alborz Mountains consist of Pre-Cambrian crystalline basement rocks, Paleozoic and Mesozoic marine deposits, Eocene volcanics and volcaniclastics and intrusives of variable age (Fig. 1). This assemblage indicates a complex history of deformation, exhumation, metamorphism, magmatism, subsidence and sedimentation that includes: the development of a metamorphic basement during the Neoproterozoic Pan-Africa Orogeny (e.g., Guest et al., 2006; Hassanzadeh et al., 2008), the deposition of unconformable carbonate and clastic marine deposits of Pre-Cambrian and Paleozoic age along a rifted passive margin associated with the opening the Paleo-Tethys Ocean (e.g., Horton et al., 2008), the occurrence of the Triassic Cimmerian Orogeny where the passive margin sediments experienced metamorphism (e.g., Zanchi et al., 2009; Omrani et al., 2013), renewed Mesozoic subsidence in association with the sedimentation of post-orogenic clastic sediments of the Shemshak Formation (e.g., Zanchi et al., 2009; Wilmesen et al., 2009), deposition of shallow- to deep-marine Middle to Late Jurassic sediments during the opening of the South Caspian Basin (e.g., Brunet et al., 2003), Cretaceous thermal subsidence and marine sedimentation (Brunet et al., 2003), deformation and exhumation during a Late Cretaceous to Paleocene regional compressional event (e.g., Guest et al., 2006; Yassaghi and Madanipour, 2008; Madanipour et al., 2017), deposition of Eocene volcaniclastics in a backarc system associated with the rollback of the Neo-Tethyan oceanic slab (Guest et al., 2006; Ballato et al., 2011 and 2013; Verdel et al., 2011; Rezaeian et al., 2012), and finally contractional deformation and exhumation during the closure of the Neo-Tethys ocean and the collision between Eurasia and Arabia starting from the latest Eocene-earliest Oligocene (e.g., Guest et al., 2006; Ballato et al., 2011 and 2013, Rezaeian et al., 2012; Mouthereau et al., 2012; Madanipour et al., 2017 and 2018; Pirouz et al., 2017; Koshnaw, et al., 2018). This final event led to development of a double-verging, narrow, mountain belt with over 3 km of topographic relief that represents an effective orographic barrier to moist air masses sourced in the Caspian Sea (Fig. 1; Ballato et al., 2015). Currently, the range accommodates left-lateral shearing between the Caspian Sea and the Central Iran (Djamour et al., 2010) and is characterized by the occurrence of few seismogenic faults including the Rudbar Fault, which ruptured in 1990 leading to the catastrophic Mw 7.3 earthquake (Berberian and Walker, 2010).

The Tarom range consists of a few-km-thick pile of Eocene volcanic and volcanoclastic rocks of the Karaj Formation (Figs. 1 and 2) that were deposited in the backarc of the Neo-Tethys subduction zone between ~ 55-36 Ma (Guest et al., 2006; Ballato et al., 2011 and 2013; Verdel et al., 2011; Rezaeian et al., 2012). This was associated with the emplacement of Late Eocene (~ 41 to 37 Ma) shallow intrusive rocks (Nabatian et al., 2014). In the Tarom range these deposits form a broad, roughly symmetric anticline (Heidarzadeh et al., 2017) with smaller scales anticline-syncline pairs (Fig. 2), cut by several high angle (both south and north dipping) faults, locally with a lateral component that are not associated with major displacements. Available low-temperature thermochronology data indicate that uplift and exhumation of the Tarom range could have started around the latest Eocene-earliest Oligocene and resumed during the last ~ 10 Ma (Rezaeian et al., 2012).

3. Regional stratigraphy

The Tarom Basin was filled by post Eocene red beds that rest in angular unconformity onto Eocene volcanics and volcaniclastics of the Karaj Formation (Fig. 2). The stratigraphic position of the red beds is unknown, mostly because the regional Late Oligocene-Early Miocene marine transgression that led to the widespread deposition of the shallow-water marine limestones of the Qom Formation along the southern margin of the Eurasian plate (Reuter et al., 2009) did not reach the Tarom Basin. These marine deposits represent a regional marker and are sandwiched between the clastic deposits of the Lower Red (LRF; Oligocene) and the Upper Red (URF, Miocene) formations, hence their absence does not allow differentiating the red beds of the Tarom Basin and unravelling their stratigraphic position.

The LRF and the URF are exposed virtually everywhere along the southern margin of the Eurasian plate, where they have a thickness varying from few hundreds to few thousands of meters. These red beds are characterized by a variable amount of sandstones, conglomerates, mudstones, evaporites and locally volcanics. Although their tectono-sedimentary significance is still matter of debate, the most recent publications interpret them as synorogenic sediments associated with collisional deformation (e.g., Morley et al., 2009; Ballato et al., 2011 and 2017; Rezaeian, et al., 2012; Madaniopour et al., 2018). Lithologically, the LRF is rather heterogeneous, while the URF seems to have more uniform characteristics, and hence has been differentiated in several geologic maps into 3 Units (M1, M2 and M3 (e.g., Davoudzadeh et al., 1997; Fig. 2). Units M1 and M3 are generally dominated by mudstones and evaporites with a variable amount of sandstone and conglomerate, respectively, while Unit M2 is characterized by abundant sandstone layers (Fig. 2). The URF is superseded by supposed Pliocene conglomerates known as Hezadarreh Formation (Rieben et al., 1955), that are generally thought to mark an intensification of collisional deformation. These conglomerates are diachronous and their age depends on their position with respect to the mountain fronts that were active at that time. For example, in the southern Alborz Mountains their deposition started at ~ 7.5 Ma (Ballato et al., 2008), while in the interior of the Iranian plateau they were deposited from ~ 10.7 Ma (Tavaq Conglomerates, Great Pari Sedimentary Basin; Ballato et al., 2017).

4. Stratigraphic and structural setting of the Tarom Basin

The red beds of the Tarom Basin consist of coarse- to medium-grained clastic deposits passing laterally toward the basin axis to finer grained sediments and evaporites (Fig. 3B). The minimum thickness of the basin-fill sediments observable in the field in the central sectors of the basin is about 1185 m, while the lack of major unconformity, suggest that sedimentation was rather continuous. In some parts, the red beds are unconformably covered by gently deformed, conglomerates of supposed Pliocene age that should be stratigraphically equivalent to the Hezardarreh Formation (Fig. 3A). Furthermore, at least three generations of terrace conglomerates can be observed in the field, suggesting the occurrence of recent phases of sediment aggradation and fluvial incision (Fig. 3G).

Along the southern margin of the basin, the red beds dip few degrees toward the NE (up to 20°), while the underlying volcanics are generally steeper (Figs. 3C) and can be locally folded (Fig. 3B). In addition, the southern margin of the basin is characterized by several steep synsedimentary normal faults (Fig. 3D), mostly parallel to the strike of the basin, that provide evidences for localized extension sub-parallel to the regional shortening direction (NE-SW; Madanipour et al., 2017). The significance and origin of these faults is discussed in Chapter 3. In any case, these faults do not appear to be linked to major extensional events and hence should not have controlled the large-scale subsidence pattern.

Along the northern side of the basin, the setting is more complex and heterogeneous. There, the Eocene deposits of the Karaj Formation are either sub-vertical or overturned. For example, in the central-southern sectors of the basin, the unconformable red beds are also subvertical to overturned (Fig. 3E) and exhibit a rapid shallowing upward trend suggesting the occurrence of growth strata. Conversely, in the central-northern sectors of the basin the angular unconformity is more pronounced, and the red beds dip less than 30° to the south-west (Fig. 3F). There, we do not have evidences for syndepositional deformation.

The central sectors of the basin are also characterized by several upright syncline-anticlines pairs subparallel to the strike of the basin (Fig. 2). These structures have a lateral extent of few kilometres, therefore their geometry is highly variable along strike. Figure 3H shows the core of one of these anticlines which is characterized by evaporites layers that have been deformed in a disharmonic manner and may have acted as local decollement horizon.

Currently, the basin is drained by the ~800 km long Qezel-Owzan River (QOR), the second largest river of Iran, which is flowing from the elevated Iranian Plateau to the Caspian

Sea (Fig. 1). The connection between the Iranian Plateau, the Tarom Basin and the Caspian Sea occurs trough narrow bedrock gorges across the Tarom range and the Alborz Mountains suggesting a complex history of internal drainage conditions that culminated with lake overspill (Heidarzadeh et al., 2017). In particular, the connection between the Tarom Basin and the Iranian Plateau must have been established during the last 4 Ma as suggested by the stratigraphic record of a sedimentary basin in the plateau interior (Mianeh Basin; Heidarzadeh et al., 2017).

5. Material and methods

To unravel the basin filling history of the Tarom Basin and its tectonostratigraphic evolution I performed a multidisciplinary study including: 1) a detailed sedimentologic study that provided the basis for an assessment of the depositional environments (Tables 1, 2 and 3; 2) a geochronologic study (U-Pb on zircons) of the uppermost volcanics of the Karaj Formation and of the red beds, that combined with 3) a magnetostratigraphic analyses provided a chronostratigraphic framework for the red clastics; and finally 4) a provenance study (sandstone petrography and paleocurrent analysis in the field) to identify compositional variations related to exposure of new sources and/or drainage-pattern reorganization in the sediment source area. Detailed information about the analytical methods are provided in the Appendix section.

This approach was employed on two stratigraphic sections exposed along the southern margin of the basin (TV and KA sections; Fig. 2) and on a third one located in the northern limb of a north-vergent anticline in the central sectors of the basin (GH section; Fig. 2). These sections are stratigraphically continuous and are not affected by major faults, therefore they represent an ideal setting for magnetostratigraphic sampling. The red beds along the southern basin margin are tilted northward with a dip angle between 14° to 30°, whereas those along the northern limb of anticline in the basin centre are steeply northward (occasionally overturned strata) with a dip angle between 40° to 88°. The stratigraphic sections along the southern margin cover the lowermost stratigraphic interval of the basin fill and consist mainly of reddish or light brownish conglomerates with intercalations of mudstone and fine-grained sandstone layers evolving up section into channelized sandstones with conglomerate lenses (fluvial channels see next section) and finer-grained sediments with tabular geometries (flood plain deposits see next section). The stratigraphic section in the basin center consists mainly of reddish or brownish mudstones, thin bedded sandstones and evaporates layers, locally with intercalations of conglomerates lenses which become more abundant toward the top of the section.

6. Depositional systems

Based on my field observations (lithological characteristics, lateral and vertical grain size variations, sedimentary structures and geometry of the sedimentary bodies) and according to the classification scheme of Miall (1985; 1996), I established a total of eighteen lithofacies types (Table 1 and Fig. 4) and recognized eight facies associations (Table 2 and Fig. 5). The combination of the facies associations led to the reconstruction of four depositional environments (alluvial fan, braided river, playa-lake and lacustrine settings; Fig. 5). In the following, I describe the main characteristics of these depositional settings.

6.1. Alluvial fan system

Alluvial fan deposits (Figs. 5A and 5B) are mostly located along both margins of the Tarom Basin and include two facies associations: (1) disorganized granule-boulder conglomerate (G1; Figs. 4A and 5A), and (2) moderately to well organized granule-boulder conglomerate (G2; Figs. 4B and 5B). I interpret the G1 facies association with weakly developed clast imbrications and erosive basal contacts as high-energy stream-floods equivalent to those produced by gravel-laden streams or sediment gravity flow deposits (hyperconcentrated flow and turbulent flow) in poorly confined channels (Figs. 4A and 5A; e.g., Maizels, 1989; Stanistreet & McCarthy, 1993; Ridgway & DeCelles, 1993; Miall, 1996; Blair, 1999). The beds geometry suggests the occurrence of sheet flows (Hein, 1982) with limited development of longitudinal bars (Boothroyd & Ashley, 1975; Todd, 1989). The G2 facies association is interpreted as traction- current deposits in poorly confined channels under conditions of higher bed shear stress (Figs. 4B and 5B; e.g., Stanistreet and McCarthy, 1993; Miall, 1996; Blair, 1999; Ballato et al., 2011).

6.2. Braided fluvial system

The braided river deposits (Figs. 5C, 5D and 5E) are characterized by five facies associations: (1) well-organized granule-pebble conglomerate (G3), (2) sandstone (S), (3) interbedded fine-grained sandstone and mudstone (SM), and (4) evaporite (E). The G3 facies association is interpreted to reflect traction-current deposits (longitudinal bars or lag deposits) related to the waning stage of high-energy flow in a laterally confined system (e.g., Stanistreet & McCarthy, 1993; Miall, 1996; Blair, 1999). The erosive basal contact of these conglomerates, together with their lens geometry and the interfingering with stratified sandstones suggests deposition in a braided channel with a variable proportion of gravel and sand (Figs. 4C and 5C; e.g., Miall, 1996). The S facies association is interpreted to represent deposition in lower flow and upper plane-bed flow regimes (e.g., Miall, 1996). The occurrence of planar (Sp) and trough cross-stratified (St); medium to coarse-grained, pebbly sandstones are interpreted as bedforms (fluvial dunes) migrating in a confined flow during upper to lower flow regimes (Fig. 4C; Uba et. al, 2005; Siks and Horton, 2011). Overall, these observations indicate deposition in fluvial channel. The SM facies association (Fig. 5D) includes sandstones with cross (Sr; Fig. 4D) and planar lamination (Sh and Sl; Fig. 5D) that are interpreted as sheet-flow deposits in a poorly confined to unconfined flow evolving from the upper flow regime to a waning flow stage. The SM facies association includes also massive to parallel laminated mudstones (Fm and Fl; Fig. 4F), which can be locally dominant and are interpreted to represent suspension fallout deposits (e.g., Ghibaudo, 1992) from standing or slowly moving waters in the floodplain (e.g., Miall, 1977 and 1978). Locally, the SM facies association can be characterized by the development of carbonate nodules and rizholithes indicating paleosols formation (P; Fig. 4G); this could have resulted from lengthy pauses in sedimentation or slow sedimentation rates (e.g., Kraus, 1999). The E facies association (Ev; Fig. 4H) is interpreted to represent precipitation of salt minerals from the evaporation of lake water and the subsequent concentration of dissolved minerals in the remaining water. Occasionally this can lead to the complete desiccation, as shown by the presence of mud cracks (e.g., Lowenstein & Hardie, 1985).

Finally, in the KA stratigraphic section in proximity of the contact with the Eocene volcanics forming the basin margin I found, embedded in the fluvial deposits, the BD facies association (Fig. 6). This disorganized package of blocks with different size and sediments of variable grain size is interpreted as landslide deposits (sturzstrom) caused by gravitational collapse of the adjacent mountain front (e.g., Hermanns and Strecker 1999). This interpretation is further supported by the occurrence of a clay-reach sheared basal contact (Fig. 6D) and the presence of a dense and irregular network of fractures (jigsaw cracks; Fig. 6C).

6.3. Lacustrine system

The lacustrine system is located along the central sectors of the basin (Figs. 4E, 4F, 5F and 5G; section GH) and is characterized by two facies associations: (1) mudstone (M) and (2) interbedded fine-grained sandstone and mudstone (SM). Tabular bodies of laminated mudstone of the M facies association are typical of suspension deposits in a lacustrine offshore setting and indicate a deepening of the system (Fig. 4F). Lenses of fine grained-sandstone with symmetrical ripple marks interbedded with mudstone (lenticular and waving bedding Figs. 4E and 5F) in the SM facies association indicate deposition in the lacustrine shoreface-offshore transition. In few sectors of the GH stratigraphic section, the tabular sandstones with symmetric ripples become dominant suggesting sedimentation in the lacustrine shoreface (Uba et. al, 2005). These intervals, however, are relatively rare and generally have a limited thickness (< 1 m), therefore most of the lacustrine sediments exposed in the section were deposited either in the offshore or in the shoreface-offshore transition setting.

6.4. Playa lake system

The playa lake system is also located in the central sectors of the basin where it alternates with the lacustrine setting (GH stratigraphic section, Figs. 4H and 5H). These deposits include two facies associations such as (1) mudstone (M) and (2) evaporite salt minerals (E). The first facies association (mudstone; M) is interpreted to represent deposits settled from suspension in arid to semiarid, oxidizing conditions as documented by the presence of red coloured sediments and the occurrence of desiccation cracks (e.g., Lowenstein & Hardie, 1985). The second facies association (E) is interpreted to represent evaporite layers (mostly gypsum) precipitated during short-lived desiccation episodes. Overall, these obervations suggest that sedimentation occurred in a shallow playa lake setting.

Table 1. Description and interpretation of lithofacies

Facies code	Characteristics	Interpretation
Gmd	Disorganised, structureless, matrix-supported, mostly monomictic conglomerate. Granules to boulders, subangular to angular clasts. Maximum clast diameter 40 cm	Mass flows deposits from hyperconcentrated or turbulent flow
Gcd	Disorganised, structureless, clast-supported, mostly monomictic conglomerate with crude bedding. Granules to boulders, subangular to moderately rounded clasts. Maximum clast diameter 40 cm	Stream-floods deposits with concentrated clasts
Gco	Moderately organized, clast supported, monomictic to polymictic conglomerate. Granules to cobbles, subangular to rounded clasts, normal grading, and weak imbrication. Maximum clast diameter 20 cm	Traction bedload deposits
Gh	Clast-supported, horizontally bedded, monomictic to polymictic conglomerate. Granules to pebbles, subrounded to well-rounded clasts, normal to inverse grading with imbrication. Maximum clast diameter 5 cm	Traction current bedforms (bars)
Gt	Clast-supported, trough cross-stratified, monomictic to polymictic conglomerate. Granules to pebbles, subrounded to well-rounded clasts, normal grading. Maximum clast diameter 5 cm	Traction current bedforms (bars)

Gp	Clast-supported planar cross-stratified monomictic to polymictic conglomerate. Granules to pebbles, subrounded to rounded, normal grading. Maximum clast diameter 5 cm	Traction current bedforms (bars)
Br	Matrix supported, structureless monomictic breccia. Granules to boulders, very angular clasts, inverse grading. Maximum clast diameter 1 m	Rock avalanche deposits (sturzstrom)
Sp	Planer cross-stratified sandstone. Medium to coarse grain size, moderately to well sorted occasionally with pebbles	Dune migration during upper to lower flow regime
Sl	Horizontally laminated sandstone. Very fine to medium grain size, well sorted occasionally with pebbles	Bedforms deposited under upper to lower flow regime
Sr	Rippled sandstone (asymmetric ripples). Very fine to medium grain size, well sorted	Ripples under lower flow regime
Sh	Horizontally stratified sandstone. Very fine to coarse grain size, moderately to well sorted, occasionally with pebbles	Planar bed flow during upper flow regime
St	Trough cross-stratified sandstone. Medium to coarse grain size moderately to well sorted, occasionally with pebbles	Dune migration during upper to lower flow regime
Smw	Rippled sandstone (symmetrical ripples). Fine to medium-grain size well sorted	Wave (bidirectional current) deposits
Fm	Massive structureless calcareous mudstone	Suspension deposits, overbank or abandoned channel
Fl	Finely laminated calcareous mudstone. Flat parallel lamination, small-scale ripples, locally with mud cracks	Suspension deposits, overbank or abandoned channel
Mr	Sheared reddish clay with unsorted angular clasts	Shearing stress at the base of a rock avalanche
P	Mudstone to fine-grained sandstone with carbonate nodules	Paleosol formation
Ev	Evaporites, locally associated with gypsum-filling fractures	In situ accumulation during evaporation of standing water

Table 2. Description, lithofacies, architectural elements, and interpretation of depositional processes and environments of facies association

Facies association	Description	Lithofacies	Architectural elements	Interpretation of depositional process	Depositional setting
G1 (disorganized granule-boulder conglomerate)	Structureless to poorly organized, matrix- to clast-supported conglomerate. Beds 0.2 to1 m thick with lateral extent of few tens of meters and a planar to slightly erosive basal contacts. Interbedded with facies associations G2 and G3	Gmd, Gcd	Gravel sheets and poorly confined channels	Sediment gravity-flow deposits	Alluvial-fan system
G2 (moderately to well organized granule-boulder conglomerate)	Moderately to well-organized, clast-supported, ungraded to normally graded, moderately to poorly sorted, poorly imbricated conglomerate. Moderate to poor horizontal and trough cross-stratification. Beds 0.2- to 1-m-thick with a lateral extent of few tens of meters and a slightly erosive basal contact. Interbedded with facies associations G1, G3, S and SM	Gco, Gh, Gt	Gravel sheets, and gravel downstream accretion macroforms (bars)	Traction bedload deposits in a gravel-dominated, poorly confined channel or in a gravel sheet	Alluvial-fan system
G3 (well organized granule-cobble conglomerate)	Well organized, clast-supported, channelized, horizontally, planar and trough cross-bedded, moderately to well sorted, conglomerate with slightly erosional contacts and a lateral extent of up to tens of meters. Interbedded with facies associations S, G2, SM, and rarely M	Gco, Gp, Gh, Gt, Sh, St, Sp	Channel-fill complex and gravel bedforms (gravel bars and lenses)	Traction bed load deposits in a gravel-dominated, well-confined channel	Alluvial-fan and proximal fluvial system
DB (Disorganized, granules to boulder breccia)	Chaotic, matrix supported, poorly sorted breccia with a sheared clay basal contact and few tens of meters lateral extent	Br, Mr	Probably lobate (full geometry not exposed)	Gravitational collapse from the adjacent mountain front	Landslide deposits (sturzstrom)
S (sandstone)	Channelized, fine to medium-grained, locally coarse-grained to pebbly, normally grained, fining upward sandstone. Sedimentary structures include horizontal, planar and trough cross-bedding and towards the top of the sandstone body ripples and parallal lamination. Beds 0.3- to 1.5-m-thick with lateral extent of few tens of meters. Erosive concave-up base contacts. Interbedded with facies G3, SM, M, and rarely E	Sh, St, Sp, Sl, Sr, Gh, Gt, Gp	Channel-fill complex, sandy bedforms and sandy downstream accretionary macroforms	Channel fill deposits in a well-confined sand-dominated fluvial channel	Fluvial system (channel complex)

SM (interbedded fine-grained sandstone and mudstone)	Fine-grained sandstone and siltstone with a tabular geometry. Sedimentary structures include parallel lamination symmetrical and asymmetrical ripples locally climbing. Beds 0.1- to 0.5-m-thick, and a lateral extent up to several tens of meters. Basal contacts are flat, non-erosive, and rarely slightly concave up. Proportion between mudstone and sandstone variable. Locally, palaeosol horizons consisting of mottled mudstone and calcite nodules, developed. Interbedded with facies S, G3, M and locally E (in this case they are associated with gypsum-filled fractures)	Sh, Sl, Sr, Smw Fl, Fm, P	Sheet-like and wedging deposits	Sheet-flow deposits in poorly confined to unconfined flow, evolving from upper flow regime to waning flow stage and suspension from standing water, and lacustrine sediments deposited either above the mean fair-weather wave base (sandstone dominating) or above the mean storm wave base (mudstone dominating)	Fluvial (floodplain), playa-lake and lacustrine system (beach to nearshore and offshore environment)
M (mudstone)	Massive to laminated grey to light red mudstone. Locally, poorly developed calcrete as well as gypcrete. Beds with a flat non-erosive contact typically 0.02- to 0.5-m-thick and a lateral extent up to several tens of meters. Interbedded with facies S, SM, and locally E (in this case they are associated with gypsum-filled fractures)	Fl, Fm, P	Sheet-like	Suspension deposits in standing water	Fluvial (floodplain), playa-lake and lacustrine system (offshore)
E (evaporite)	Evaporite deposits, 0.05 to 0.3 m thick with a lateral extent of several tens of meters. Generally associated with gypsum-filled fractures. They can form packages of up to 20 m. Interbedded with facies M, rarely with SM and S	Ev	Sheet-like	Evaporation deposits from standing water	Play-lake or fluvial (highly evaporative flood plain) system

7. Zircon U-Pb geochronology

Five samples were collected for Zircon U-Pb dating in the Eocene volcanics and the red beds. The goal was to constrain the top of the Karaj Formation and provide independent age constrains on the depositional age of the synorogenic red beds. Results are shown in table 3 and in the Appendix A1.

The contact between the Karaj Formation and the overlying red beds is well exposed along both margins of the basin. Considering that the northern margin has experienced a greater degree of deformation and erosion (compare Figs. 3B and 3C with Figs. 3E and 3F) I sampled the contact along the southern margin of the basin in two different locations (Fig. 1). Sample GH-15-03 represents a > 20-m-thick white tuff that can be followed along strike for about five kilometers. This lithotype is stratigraphically located below a thick package (several tens of meters) of coarse-grained volcanoclastic deposits that are less suitable for zircon U-Pb dating and represent the top of the Karaj Formation in this area (Fig. 3B). These units are characterized by a system of open syncline-anticline pairs with a wavelength of several tens of meters (Fig. 3B). Tuff sample GH-15-03 yielded only few zircon grains with a weighted average age of 36.7 ± 2.6 Ma (Table 3). Along strike (to the SE), another sample (GH-15-01) was collected from a rhyolite exposed on top the Karaj Formation (Fig. 3C). In this area the angular unconformity with the overlaying red beds has a low angle (< 10°). This sample yielded a weighted average age of 38.7 ± 1.4 Ma. This age overlaps with the previous sample (within a two-sigma error) suggesting that the termination of widespread arc volcanism should have occurred sometime between 38 and 36 Ma. This age agrees with those obtained by previous studies (~ 36 Ma, Ballato et al., 2011; ~ 37 Ma, Verdel et al., 2011) in central and northern Iran.

An additional, few cm-thick, ash layer (TM-16-01) was collected within the red beds in proximity to the top of the KA stratigraphic section. This sample is fundamental for pinpointing the magnetostratigraphic correlation (see next sections) and yielded a weighted average age over 13 grains of 10.7 ± 0.4 Ma (Table 3). This value does not include nine grains that clustered around 13-12 Ma. If I include these grains the weighted average age over 22 grains will be 11.3 ± 0.5 Ma (Table 3). Considering that a ~ 10.7-My-old tuff has been dated about 120 km to the NW in three different locations (Ballato et al., 2017), I prefer to consider the 10.7 Ma option as more reliable that the 11.3 Ma. Accordingly, the 13-12-My-old zircon grains should represent crystals that spent 2-3 million of years in the magmatic chamber before the eruption.

Finally, two more samples were collected in the red beds, directly upsection of sample GH-15-03. These two samples are located right above the unconformity (GH-15-02, resampled in a second stage as GH-17-02) and about 400 m (stratigraphically) above it (GH-17-04). The first sample is a weathered, reworked white tuff, while the second one is a light green tuffaceous sandstone with very pristine biotite crystals. These samples gave very similar ages (39.7 ± 1.3 and 38.3 ± 0.9 Ma, respectively; Table 3), which look almost identical to those obtained for the top of the Karaj Formation. Therefore, based on the stratigraphic separation between them I consider these two samples as reworked volcanic material from the eroding Karaj Formation that does not provide indication about the depositional age of the red beds.

Combined, new zircon ages indicate that arc volcanism in this area must have lasted until 38-36 Ma, while the deposition of the red beds appears to have occurred during the Miocene.

Table 3: Zircon U-Pb dating results

Sample code	Age (Ma)	Error 2s (Ma)	N of grains analyzed	N of grains used	MSWD	Rock type	Formation / Unit	Lat (Dec°)	Long (Dec°)	Elevation (m)
GH-15-01	38.7	1.8	11	10	0.4	Rhyolite	Karaj F	36.74525	49.23086	375
GH-15-02/ GH-17-02	39.7	1.3	18	16	1.8	Reworked tuff	Red Beds	36.70804	49.14391	752
GH-15-03	36.7	2.8	6	4	0.8	White tuff	Karaj F	36.70342	49.14172	840
GH-17-04	38.3	0.9	10	10	1.0	Tuffaceous sandstone	Red Beds	36.72139	49.14806	576
TM-16-01	10.7	0.4	24	13	1.3	Ash	Red Beds	36.91298	48.83748	600
TM-16-01 alternative	11.3.	0.5	24	22	3.8					

8. Paleomagnetic results

The initial Natural Remnant Magnetization (NRM) intensities vary between 8.59 × 10^{-4} and 1.01 × 10^{-2} A/M, and between 9.91 × 10^{-4} and 1.01 × 10^{-2}A/M for the TV and KA samples, respectively (Figs. 8 and 9). The NRM intensities for the GH samples are about one order of magnitude lower and vary between 9.89× 10^{-5} and 1.01 × 10^{-3} A/M (Fig. 10). The highest NRM values (average of 4.34 × 10^{-2} A/M) were obtained from the alluvial fan deposits at the base of TV section (first ∼15 m); upsection, the NRM values do not show significant variations (Fig. 8). Similarly, KA samples show the highest NRM values (average = 1.73 × 10^{-2} A/M) at the base of the section (up to ∼ 15 m) and a rather uniform pattern until the top of the section. Conversely, the GH samples exhibit a great NRM variability along the entire sequence, especially along specific intervals dominated by playa lake deposits and the floodplain deposits on top of the sequence (Fig. 10). Magnetic susceptibility results from the three studied stratigraphic sections in the Tarom Basin are shown in figures 8, 9 and 10. Samples from TV and KA sections show bulk susceptibility (k) values ranging from 170 to 10970 × 10^{-6} SI and 460 to 26570 × 10^{-6} SI, respectively (Figs. 8 and 9). This relatively high k values are most probably related to the significant contribution of the volcanoclastic Karaj Formation which is particularly rich in magnetite (Ballato et al., 2008). Conversely, the GH samples have lower magnetic susceptibility (k) values ranging from 70 to 3650 × 10^{-6} SI that may reflect a more composite sediment source area (Fig. 10).

In order to isolate the Characteristic Remnant Magnetization (ChRM), 375 samples from the three stratigraphic sections were subjected to progressive thermal demagnetization and 150 samples were subjected to alternate field (AF) demagnetization. The majority of the samples display two magnetic components including: 1) low-temperature (LTC) and low coercivity (LCC), viscous components generally erased below 430°C and 20 mT, respectively, that do not decay toward the origin and, 2) high-temperature (HTC) and high coercivity (HCC) components decaying around 580°C and 100/120mT, respectively, toward the origin and carrying out the ChRM. Most of the samples with a HTC and HCC were completely demagnetized at 580°C and 100/120mT, indicating the occurrence of magnetite as major ChRM carrier, while some of samples that mostly collected from GH section exhibit a sharp decrease of magnetization at 600-640° suggesting the presence of hematite (Fig. 7A).

Section TV displays, only 11 samples with two magnetic components with a LTC/LCC erased below 350°C and 15 mT, and 63 samples with a HTC and HCC removed between 530 and 560°C and between 20 and 100/120mT, indicating that magnetite was the main carrier of the ChRM (Fig. 7A). Section KA displays, only 19 samples with a viscous (LTC and LCC) component, while in 125 samples the occurrence of HTC and HCC allow isolating the ChRM. Likewise, most of the samples of section GH were completely demagnetized at 580°C or between 15and100/120mT, so that 41 samples from the analysed 321 samples display only a viscous component, while in 247 samples magnetite was the main carrier of the ChRM (Fig. 7A). The rest of 39 samples were rejected because the ChRM direction was unstable or because the maximum angular deviation (MAD) was >10. Overall, in most of the measured samples the dominant magnetic components (ChRM) were successfully isolated after removing one or two secondary components of magnetization. Moreover, mean normal and reversed polarity directions of each magnetostratigraphic section after tilt correction were calculated separately..

The overall mean normal and reverse polarity directions for three stratigraphic section TV, KA and GH sections is represented in table 4 and Figure 7B.

Table 4. The overall mean normal and reverse polarity directions for three stratigraphic section TV, KA and GH sections. Direction (Dec = declination; Inc = inclination). K is estimate of precision parameter, α95 is semi-angle of cone of 95% confidence.

(TV samples)	N	Dec	Inc	K	Alpha 95
Geographic (In-situ)	54	0.3	53.8	8.39	7.1
Stratigraphic (Tilt-corrected)	54	358.5	35.7	8.67	7

(KA samples)	N	Dec	Inc	K	Alpha 95
Geographic (In-situ)	103	347.5	58	8.34	5.1
Stratigraphic (Tilt-corrected)	103	1.6	43	8.44	5.1

(GH samples)	N	Dec	Inc	K	Alpha 95
Geographic (In-situ)	218	241.9	70.4	4.98	4.8
Stratigraphic (Tilt-corrected)	218	13.7	39.2	5.47	4.5

To assess the primary nature of the selected ChRM directions the reversal and fold tests were performed for all the ChRM dataset from three stratigraphic sections using a Python script and based on the orientation matrix method of Tauxe et al., (1991). The fold test is clearly positive with clustering of directions at maximum unfolding indicating that the accepted directions were acquired prior to folding. Therefore, the sediments are likely to carry a primary paleomagnetic record (Fig. 7D).

The paleomagnetic reversal test for each magnetostratigraphic section was separately used following the method reported by Tauxe et al., 1991 (Fig. 7C). The test for TV and KA samples show that all three (z, y and z) components overlap for both normal and reversed polarity directions at the 95% confidence level. This means that the normal and reverse polarity directions of TV and KA samples pass the reversal test**,** thus, the positive reversal test indicates a complete removal of the secondary components, so that mean normal and reverse directions are antipodal and (Fig. 7C) a hence a local magnetostratigraphy can be obtained. The reversal test for GH samples, however, is not positive at the 95% confidence level although the directions are close to antipodal, so that only the Y component overlaps for both normal and reversed polarity directions at this level (Fig. 7C). The negative reversal test for GH samples probably results from the incomplete separation of components of some samples. However, although the reversal test yielded a negative response, our data allowed determining correct polarities (latitude of the Virtual Geomagnetic Poles, VGP) and hence to build up a reliable local magnetic polarity stratigraphy also for the GH section.

9. Magnetostratigraphy

The VGP latitudes from the new paleomagnetic data set, define normal and reverse polarity magnetozones (Figs. 8, 9 and 10) and hence allow us to construct for each section a magnetic polarity stratigraphy to be correlated with the Geomagnetic Polarity Time Scale (GPTS) (Gradstein et al., 2012).

9.1. TV stratigraphic section

Patterns of VGP latitudes in section TV define 4 normal and 2 reverse polarity zones denoted as N1-N4 and R1-R2, respectively. Based on a radiometric age (sample TM-16-01; Table 3) from the overlying KA section, I correlate the uppermost long normal polarity zone N1 and the reverse polarity zone R1 of section TV with chron C5AC. Consequently, the long normal polarity zone N2 in the middle part of the section is correlated with chron C5AD and the short normal polarity zone N3 with chron C5B. This implies that the reverse polarity zone R2 in the lowermost part of the section should correspond to chron C5B, while the long normal polarity zone N4 at the base of the section should correlate with chron C5C. Accordingly, a depositional age of ~16 to 14 Ma is proposed for the TV stratigraphic section (Fig. 7).

9.2. KA stratigraphic section

In the KA stratigraphic section 7 normal (N1-N7) and 8 reverse (R1-R8) polarity zones were defined. A Zircon U-Pb age of 10.7±0.4 Ma (Table 3) from an ash layer in the upper part of the section at (~ 500 m) suggests that the long-lasting normal polarity zone N1 should be correlated with chron C5n1n. Consequently, the two short reverse polarity zones R1 and R2 and the longer normal polarity zone N2 should belong to the same C5 chron. According to these correlations, the polarity zones N3, N4, N5 as well as the reverse polarity zones R3, R4, R5 and R6 should correspond to chron C5A. In the lower part of section, the normal and reverse polarity zones N6 and R7 can be correlated with chron C5AA, while the long lasting normal polarity (N7) and the short reverse polarity at the base of the section can then be correlated to C5AB chron. Based on this correlation the most likely depositional age for the KA stratigraphic section will be between ~ 13.6 to 10.3 Ma (Fig. 8)

9.3. GH stratigraphic section

Patterns of VGP latitudes in section GH define 10 normal polarity zones and 9 reverse polarity zones, denoted as N1-N10 and R1-R9, respectively. Stratigraphic sections KA and GH overlap, hence, in my tentative correlation I associate the long-lasting, distinctive normal polarity zone N1 of section KA with the normal zone N5 in the middle part of section GH. The uppermost normal polarity zones N1, N2 and N3 as well as the short reverse polarity zone R1 and long lasting reverse polarity zones R2 and R3 at the top of the section can be correlated with chron C4. Consequently, the normal and reverse polarity zones N4 and R4 correlate with chron C4A. The long-lasting normal polarity zone N5 in the middle part of the section as well as the two short normal polarity zones N6 and N7 and two long reverse polarity zones R5 and R6 correspond to chron C5. Finally, the normal polarity zones N8, N9 and N10 and the reverse polarity zones R7, R8 and R9 in the lowermost part of the section should correlate with chron C5A. Based on this correlation the depositional age of section GH should range from ~12.8 to 7.6 Ma (Fig. 9). Combined my data document a depositional age for the red beds in Tarom Basin from ~ 16.5 to at least 7.6 Ma. This implies that these red clastics belong to the Upper Red Formation.

10. Sediment accumulations rates

The sediment accumulation rates for each stratigraphic section were calculated based on the magnetostratigraphic correlations and the stratigraphic thickness measured in the field (Fig. 11). The oldest record (from ~ 16.5 Ma) is from the TV section where rates are relatively low (0.025 mm/yr) until ~ 14.6 Ma when an increase up to ~ 0.1 mm/yr occurs. From ~ 13.6 Ma the record includes both the GH and KA sections with similar rates of ~ 0.21 mm/yr at least until ~ 12.1 Ma. By ~ 12.1 Ma, sediment accumulation rates for the GH section increase up to ~ 0.29 mm/yr and remain higher than those in the KA section (at least until the top of the KA section at ~ 10.3 Ma). At the top the section, sediment accumulation rates decrease down to 0.15 mm/yr.

Overall, the sediment accumulation rates from the intermontane Tarom Basin are bit lower than those recorded in the Miocene foreland basins of N Iran (0.3 to 2.2 and 0.3 to 0.5 mm/yr for the southern Alborz Mountains and the Great Pari Basin, respectively; Ballato et al., 2008 and 2017).

11. Sandstone petrography

Petrographic analyses were performed on 6 thin sections collected along the KA and GH stratigraphic sections according to the Gazzi-Dickinson method (Ingersoll, et al., 1984). Results are plotted on QFL-c, QFL and Lm-Lv-Ls ternary diagrams (Figs. 12A-C, respectively, Dickinson et al., 1985; Garzanti, 2019). A detailed table can be found in the Appendix (Tables A3.1 and A3.2).

The KA sandstones are rather homogenous and mainly composed of volcanic mafic clasts (Lvm, 50 and 58%) and plagioclase (Pl) grains (Figs. 12A, 12C, 12D, 12G and H). These are more abundant in the lower part of the section (30 vs 19%). A few lithic meta felsic particles (Lmv; 6 to 9%) as well as a small amount (less than 5%) of quartz and heavy minerals (epidote) are the other constituents observed in the KA samples. Finally, a minor amount (≤ 3%) of lithic fragments such as lithic volcanic felsic (Lvf), lithic limestone (Lcc), lithic terrigenous (Lp), lithic metasedimentary (Lms) and metabasalt lithic fragment (Lmb) were also observed.

Conversely, the GH sandstone samples contain a lower proportion of volcanic lithics, and a higher proportion of low-grade metamorphic particles (Figs. 12B, 12C, 12E, 12F and Table A3.1). The most abundant constituent of the framework components is represented by lithic metasedimentary (Lms) clasts, which range upsection from 14 to 37% (Table 1). The second most abundant constituents are lithic terrigenous (Lp; 8-25%). Other particles that are much more abundant than in the KA samples are meta felsic (Lmv) and lithic limestone (Lcc) clasts (4 to 17% and 9 to 16%, respectively). Volcanic mafic clasts (Lvm) are less abundant than in the KA samples, and show a significant upsection decrease from 21 to 3%.

Quartz (Figs. 12E and 12I) and feldspar particles were also observed in GH sandstones (Figs. 12D and 12H). Feldspar grains are less abundant than in the KA samples, with plagioclase particles ranging from 3 to 10%, while the alkali feldspars display also a very small amount (1%). Instead, Quartz grains are more abundant (9 to 13%). A minor amount (≤ 3%) of other lithic fragments (Lvf, Lch, Lmf) and heavy minerals (such as epidote) were also observed.

Overall, the abundance of volcanic clasts in the KA samples indicates that the main sediment source along the southern margin of the basin must have been from the Eocene volcanics (Karaj Formation) of the Tarom range. Concerning the central sectors of the basin, the occurrence of metamorphic and sedimentary lithics, as well as the progressive decrease in volcanic grains suggests that the GH sandstones collected in the central sectors of the basin where mostly sourced from the northern basin margin (Alborz Mountains).

12. Discussion

This study provides new constraints on the tectono-stratigraphic evolution of the Tarom Basin in the framework of collisional deformation and plateau building processes. Based on my new age determinations (U-Pb zircon dating and magnetostratigraphic correlation), the reconstruction of the depositional systems and sediment dispersal patterns. I propose a four-stage evolutionary model for the last ~38-36 Ma. Finally, I discuss the main implications of the findings for the evolution of the IP.

12.1. ~38-36-16.5 Ma: topographic growth of the southern margin, formation of angular unconformities and development of external drainage conditions

The geometrical relationships among the strata of the Karaj Formation exposed along the southern sectors of the Tarom Basin suggest that minor folding must have occurred during the latest stages of Eocene arc volcanism around 38-36 Ma (Figs. 3B and 13). This could represent the earliest event of Late Eocene-Early Oligocene collisional deformation recorded across the entire Arabia-Eurasia collision zone from the Zagros Mountains to the Caucasus (Vincent et al., 2007; Morley et al., 2009; Ballato et al., 2011; Mouthereau et al., 2012; Rezaeian et al., 2012; Roberts et al., 2014). Furthermore, the Middle-Late Miocene age for the overlying red beds indicates that the topographic growth of the Tarom range prevented the Late Oligocene-Early Miocene marine transgression that led to the deposition of the shallow-marine sediments of the Qom Formation (e.g., Reuter et al., 2009). Therefore, between ~ 38-36 Ma and ~ 16.5 Ma (initiation of red beds sedimentation) the Tarom Basin must have experienced external drainage conditions. This implies that the eroded sediments were delivered directly to the Caspian Sea and hence a connection between the Tarom Basin and Caspian Sea must have been established after the end of arc volcanism (Fig. 14A). During this ~ 20-My-long period both margins of the basin experienced tilting that led to the development of an angular unconformity between the Karaj Formation and the overlying red beds (Fig. 3). Prior to that, the Alborz Mountains represented a topographic barrier between central Iran and the Caspian Sea as suggested by the lack of Eocene volcanics along the northern slope of the Alborz (Guest et al., 2006a).

12.2. ~16.5 to < 7.6 Ma: intermontane basin development and internal drainage conditions

Sedimentation of continental red beds in the Tarom Basin started at ~ 16.5 and lasted at least until ~ 7.6 Ma, suggesting that these sediments are stratigraphically equivalent to the

Upper Red Formation. During that time interval an intermontane basin developed most likely as flexural response to tectonic loading from the adjacent uplifting mountain ranges (Alborz Mountains to the N and Tarom range to the S; Fig. 14B). This is also recorded by the progressive increase in sediment accumulation rates (one order of magnitude, from 0.025 to 0.25 mm/yr) in different sectors of the basin from ~16 to about ~12.2 Ma (Fig. 11).

The occurrence of lacustrine and playa lake deposits in the basin depocenter further implies the development of internally drained conditions associated with the topographic growth of the Alborz Mountains, which must have disconnected the former drainage system from the Caspian Sea. Such a topographic growth was triggered by widespread regional deformation related to a more advanced stage of the Arabia-Eurasia collision (e.g., Ballato et al.,2011; Mouthereau et al., 2012) in agreement with available low temperature thermochronology data in NW Iran (Guest et al., 2006b; Rezaeian et al., 2012; Ballato et al., 2013 and 2015; Madanipour et al., 2013 and 2017). This is further corroborated by the presence of growth strata along the north margin of the basin indicating syndepositional contractional deformation, most likely triggered by a south-verging blind thrust fault (Figs. 2, 3E and 12B).

Sediment provenance data provide additional information on to the evolution of the sediment source area. The southern side of the basin received sediments from the growing Tarom range. There, exhumation has been limited to less than 3-4 km as documented by available 41-32-My-old apatite fission track ages that still record magmatic cooling (Rezaeian et al., 2012). This is also shown by sandstone petrography data from the KA section, that have a rather constant composition dominated by volcanic lithics and feldspars (feldspatho-lithic arenite; QFL plot; Fig. 13B), as expected for undissected arc regions (QtFL-c ternary diagram; Fig. 13A). Instead, the central part of the basin received a greater amount of sediments from the Alborz Mountains as documented by the higher proportion of metamorphic lithics and quartz grains (quartzo-lithic arenite; Fig. 13B). Although these sample plot also in the undissected arc (Fig. 13A) the upsection increase in metamorphic grains and the relative decrease in volcanic lithics suggests erosional unroofing with the progressive exposure of the metamorphic basement. This is consistent with Miocene apatite fission track cooling ages documenting accelerated Miocene exhumation (Rezaeian et al., 2012).

12.3. <7.6 Ma to Plio-Pliocene: drainage reintegration, basin uplift, deformation and erosion

Sometime after ~7.6 Ma, the Tarom Basin was reintegrated into an external drainage system and a new fluvial connection with the Caspian Sea developed. Although I do not have precise information about timing and mechanisms of this process, one possibility is that basin capture may have been caused by fluvial headward erosion triggered by the km-scale, prolonged, base level drop of the Caspian Sea (~ 5.5 to 3 Ma; Forte and Cowgill, 2013; Van der Back et al., 2013). Alternatively, headward incision could have been triggered by a decrease in uplift rates with respect to fluvial incision rates or overspill from the Tarom Basin into the Caspian Sea. In any case, after 4 Ma, the Tarom Basin must have been integrated into the drainage system of the Qezwl-Owzan, the second longest river of Iran flowing from the interior of the Iranian Plateau to the Caspian Sea (Fig. 1; Heidarzadeh et al., 2017). This event has been related to an overflow from the adjacent and more elevated Mianeh Basin of the Iranian Plateau into the Tarom Basin and led to the development of ~1-km-deep Amardos gorge (Fig. 1; Heidarzadeh et al., 2015).

The establishment of an external drainage system appears to coincide with intrabasinal deformation, basin uplift, and erosion, as recorded by several anticline-syncline pairs, from the central sectors of the basin (Figs. 2 and 3H). For example, Along the GH section, the occurrence of overturned red beds suggests the development of a north verging anticline possibly associated with a shallow detachment horizon within gypsum layers.

12.4. Pliocene to present: alternating episodes of basin aggradation, incisions and excavation

Following intrabasinal deformation, the Tarom Basin experienced at least one major episode of supposed Pliocene conglomerate deposition (Stocklin, 1969) as well as three main phases of basin aggradation and incision, as documented by distinct levels of Quaternary terrace conglomerates (Figs. 2, 3D, 3G and 13D). These unconformable deposits suggest the occurrence of alternating phases of limited (or absent) and efficient fluvial connectivity with the Caspian Sea. A similar configuration has been described in the intermontane basins of arid to semiarid climatic regions like those forming the Eastern Cordillera and the broken foreland of NW Argentina. There, the landscape response to Quaternary climate changes is thought to be the main driver of short-term cycles (10^5 years) of basin filling and excavation, while tectonics plays a major role in controlling the long-term filling history (10^6 years; Strecker et al., 2009; Streit et al., 2015; Schildgen et al., 2016; Tofelde et al., 2017; Pingel et al., 2019). Here, the lack of chronological constraints does not allow unravelling the role of different forcing mechanisms. In any case, it should be noted that, the supposed Pliocene conglomerates are slightly folded into a broad syncline suggesting a possible interplay between intrabasinal deformation and sedimentary loading/unloading cycles, which can hinder/promote intrabasinal deformation (Ballato et al., 2019). For example, these conglomerates are in unconformity onto folded Miocene red beds, therefore, their deformation must have occurred after their deposition either during or after their removal through fluvial erosion (i.e., during sedimentary unloading).

Finally, it should be noted that a similar long-term, tectono-stratigraphic history has been proposed for the intermontane Taleghan-Alamut basin of the central-western Alborz Mountains (Guest et al., 2007). There, the deposition of Middle-Late Miocene red beds was followed by Late Miocene-Pliocene intrabasinal deformation, Pliocene aggradation with conglomerate deposition and Quaternary fluvial incision. This common evolution suggests that the orogen may have responded in a cylindric way to similar way to (either tectonic or climatic) forcing mechanisms (Ballato et al., 2015).

12.5. Implications on plateau building processes

My multidisciplinary dataset from the Tarom Basin allows constraining the evolution of the plateau margin (Tarom range) and exploring the connection with the adjacent Alborz Mountains. In particular, my provenance data and field observations indicate that the northern basin margin (Alborz Mountains) experienced a greater magnitude of deformation and exhumation than the southern one (Tarom range). There, the topographic growth was associated with limited erosional exhumation, as also documented by the occurrence of subdued topography onlapped by basin-fill units of the plateau interior further north (Heidarzadeh et al., 2017). This suggests that most of the Miocene plate convergence in NW Iran must have been absorbed via crustal shortening and thickening in the Alborz Mountains, possibly through the reactivation of crustal-scale anisotropies inherited from its complex geologic history. Thus, the growth of the plateau margin and the gain in elevation of its adjacent interior, must have been triggered by deep-seated (mantle driven) processes rather than crustal/lithospheric shortening and thickening (e.g., Sobel et al., 2003). Additionally, the reconstruction of the basin fill history combined with field observations does not indicate the presence of a formerly elevated basin likewise the plateau interior. Thus, the Tarom Basin cannot have been an integral part of the Iranian Plateau during its phases of internal drainage or limited connectivity with the Caspian Sea.

13. Conclusions

This work represents the first detailed study in the Tarom Basin, an intermontane basin at the transition between the Iranian Plateau and the Alborz Mountains. Combined, the magnetostratigraphic, sedimentologic, geochronologic and sediment provenance analysis, allow establishing a detailed chronostratigraphic framework and reconstructing the tectono-stratigraphic evolution of this basin, as well as the erosional history of its adjacent margins. In particular, I show that the regional, Eocene arc volcanism phase in this area ended at ~ 38-36 Ma while at the same time a phase of low-magnitude compressional deformation was starting. This was followed by a prolonged phase of erosion with development of angular unconformities. By ~16.5 Ma, the topographic growth on the northern side of the basin (western Alborz Mountains) must have disconnected the Tarom Basin from the Caspian Sea, leading to the formation of an intermontane basin. Such a basin had marginal alluvial fan deposits passing laterally toward the basin axis to fine-grained fluvial and lacustrine to playa lake deposits. My new ages document that the synorogenic deposits of the Tarom range are stratigraphically equivalent to the Miocene Upper Red Formation. The accommodation space available for sedimentation was most likely controlled by lithospheric flexural in response to tectonic loading of the adjacent mountain ranges. Internal drainage conditions lasted at least until 7.6 Ma, when basin incision and excavation occurred in association with intrabasinal deformation. Subsequently the occurrence of supposed Pliocene conglomerates and at least three Quaternary terrace conglomerates indicate multiple phases of aggradation and incision. This cyclic behaviour occurred during alternating episodes of reduced and renewed fluvial connectivity with the Caspian Sea. The lack of a detailed chronology, however, does not allow understanding the forcing mechanisms for these cycles. Furthermore, my results and observations indicate that the northern margin of the basin accommodated a larger fraction of plate convergence than the southern one, most likely through the reactivation of inherited structures. This implies that uplift of the Tarom range and the plateau margin must have been triggered by deep seated, mantle drive, processes rather than shortening and thickening processes. Finally, the Tarom Basin was never integrated in the IP because it did attain such elevations.

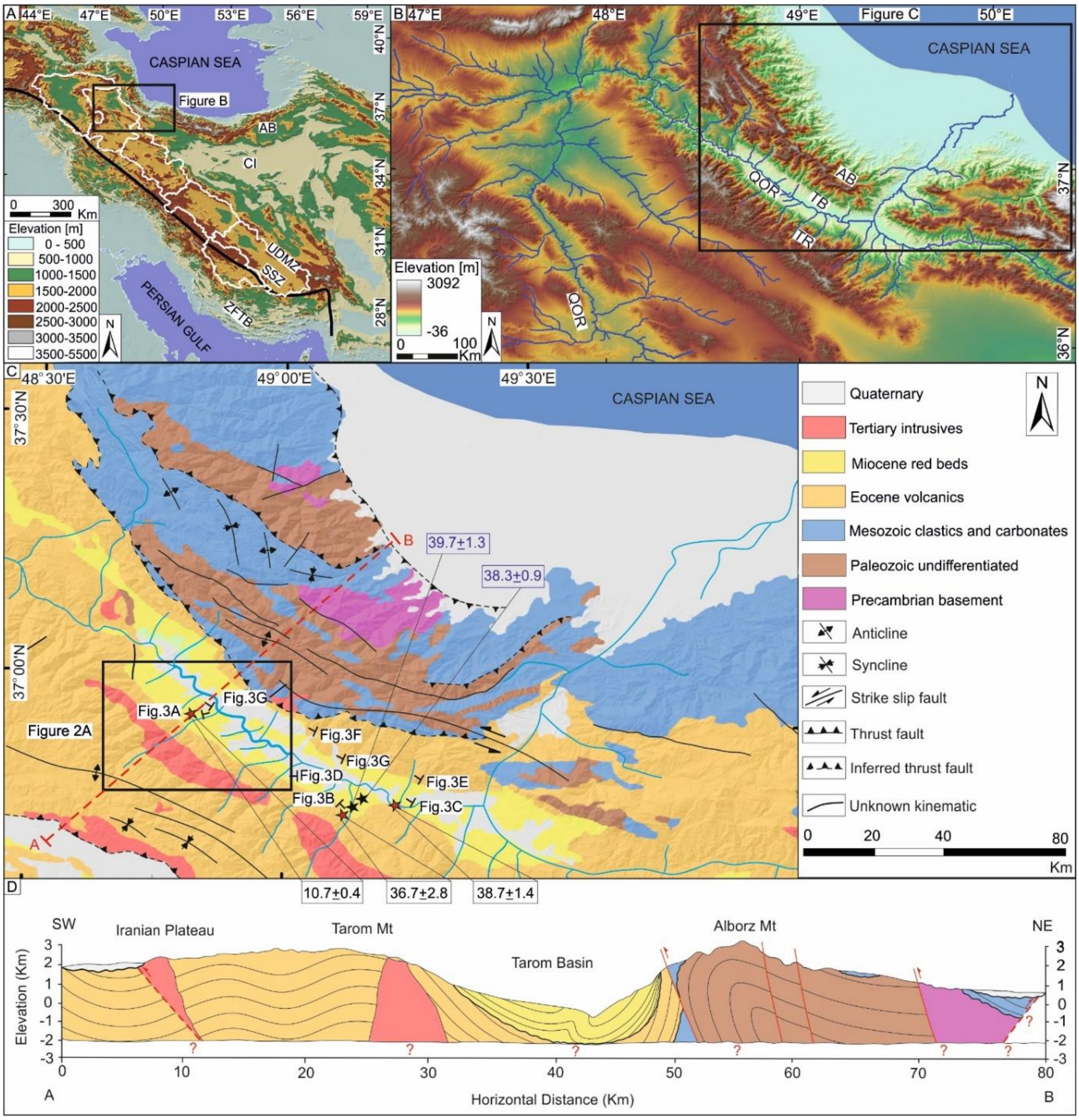

Figure 1. (A) Shuttle Radar Topographic Mission Digital Elevation Model (SRTM DEM) of Iran showing the Iranian Plateau; the white polygons indicate six main drainage basins forming the Iranian Plateau while the black line shows the approximate location of the suture zone which separates the lower Arabian plate from the upper Eurasian plate (Ballato et al., 2017). (B) DEM of NW Iran showing the Tarom Basin (TB) and its bounding ranges, Tarom range and Alborz Mountains, along the southern and the northern margins of the basin, respectively. Note the Qezel-Owzan River (QOR) drainage system (~ 55000 km^2) connecting the Iranian Plateau and the Caspian Sea trough the Tarom Basin. (C) Simplified geologic map of NW Iran showing the location of the panoramic field photographs of Figure 3. The Red stars show the location of my new zircon U-Pb ages (expressed in Ma) that provide information on the depositional ages; the black stars (and blue ages) represent reworked Eocene volcanic material within red beds that do not provide information on their depositional age. (D) Regional geological cross-section (modified after Stocklin et. al, 1969). Note that SSZ and UDMA are abbreviation of Sanandaj–Sirjan Zone and Urumieh–Dokhtar Magmatic Arc, respectively.

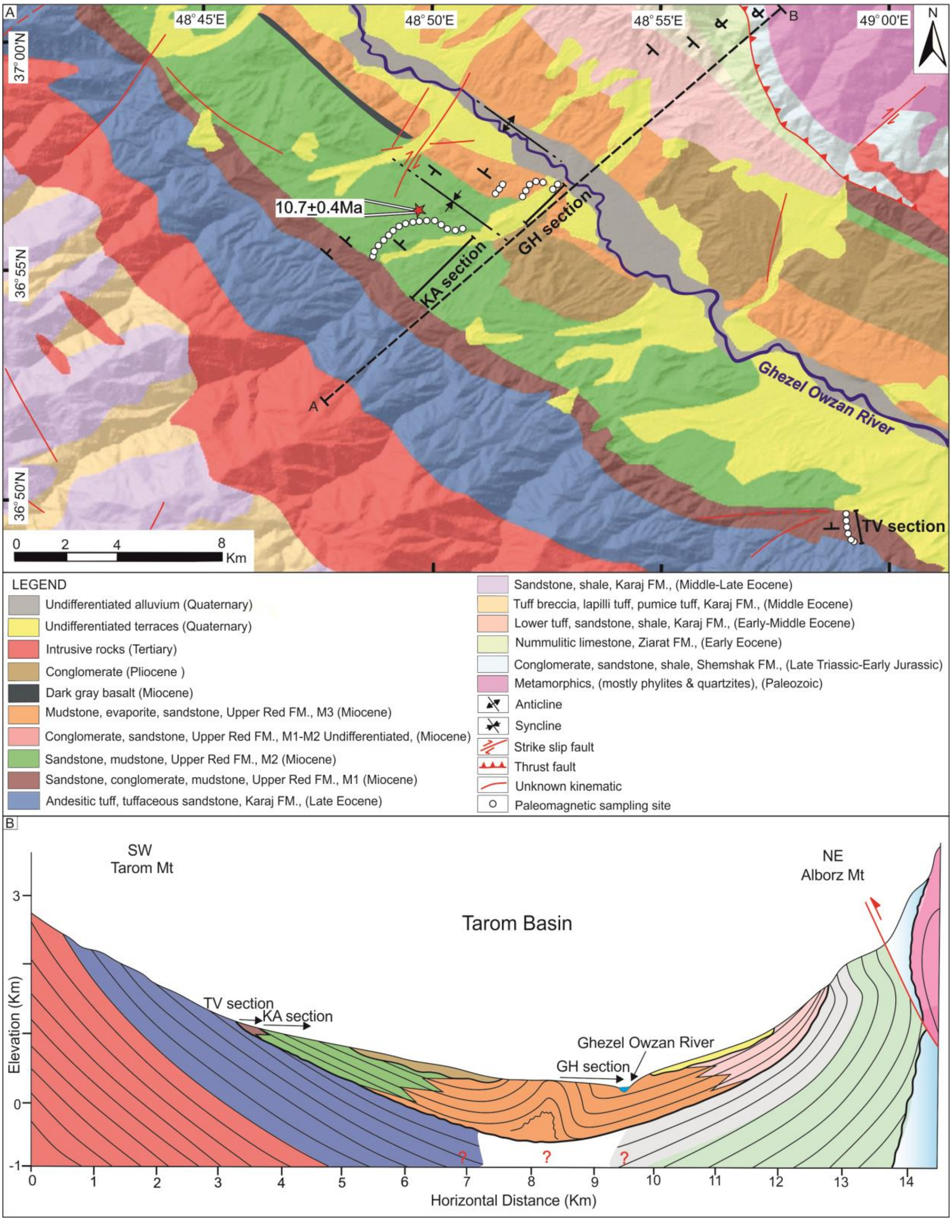

Figure 2. (A) Geologic map superimposed on a SRTM hillshade model of study area (TB). The white circles show the location of the three sections sampled for magnetostratigraphy named TV, KA and GH. The base of section G is also visible in Fig. 3H. (B) Geologic cross section along line A-B.

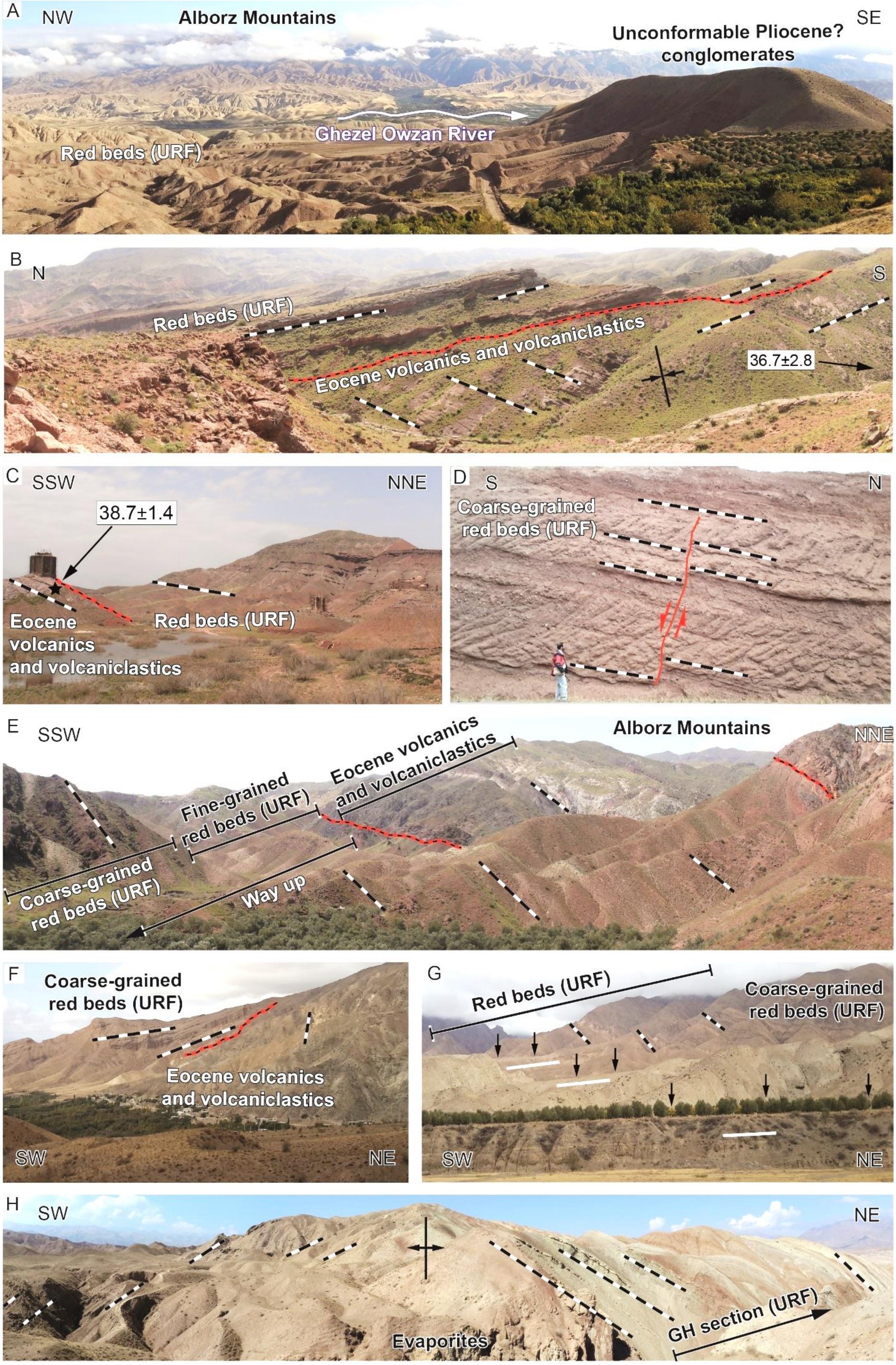
A
NW
Alborz Mountains
SE
Unconformable Pliocene? conglomerates
Ghezel Owzan River
Red beds (URF)
B
N
S
Red beds (URF)
Eocene volcanics and volcaniclastics
36.7±2.8
C
SSW
NNE
38.7±1.4
Eocene volcanics and volcaniclastics
Red beds (URF)
D
S
N
Coarse-grained red beds (URF)
E
SSW
Alborz Mountains
NNE
Eocene volcanics and volcaniclastics
Fine-grained red beds (URF)
Coarse-grained red beds (URF)
Way up
F
Coarse-grained red beds (URF)
Eocene volcanics and volcaniclastics
SW
NE
G
Red beds (URF)
Coarse-grained red beds (URF)
SW
NE
H
SW
NE
Evaporites
GH section (URF)

Fig. 3. Panoramic field photographs (see figure 1 for location) highlighting the main geometrical relationships among the units and formations exposed in the Tarom Basin. A) Northeast-facing photo showing the conglomerates supposed Pliocene age in unconformity onto deformed red beds; the conglomerates are tilted to the NNE and have a dip angle of ca. 25°. On the foreground the mountain front of the Alborz Mountains with several generation of terraces is visible (see Fig. G for details). B and C) Southeast- and northwest-facing photos documenting the unconformity (red and black line) between the Karaj Formation and the red beds in the southern margin of the basin. Black and white dashed lines show the bedding while the zircon U-Pb ages reported are in Ma (see Table 3 and Fig. 1). D) Synsedimentary normal fault exposed along the TV sections (see chapter 3 or details). E and F) Northwest-facing photos documenting the unconformity (red and black line) between the Karaj Formation and the red beds in the southern margin of the basin. Note that in Figure E the red beds are overturned. G) West-facing photo displaying three major terrace conglomerates (see black arrows); these deposits are virtually undeformed (white lines) and cover in unconformity steeply dipping red beds (black and white dashed lines). H) Northwest-facing photo showing the core of the anticline that represents the base of the stratigraphic section GH.

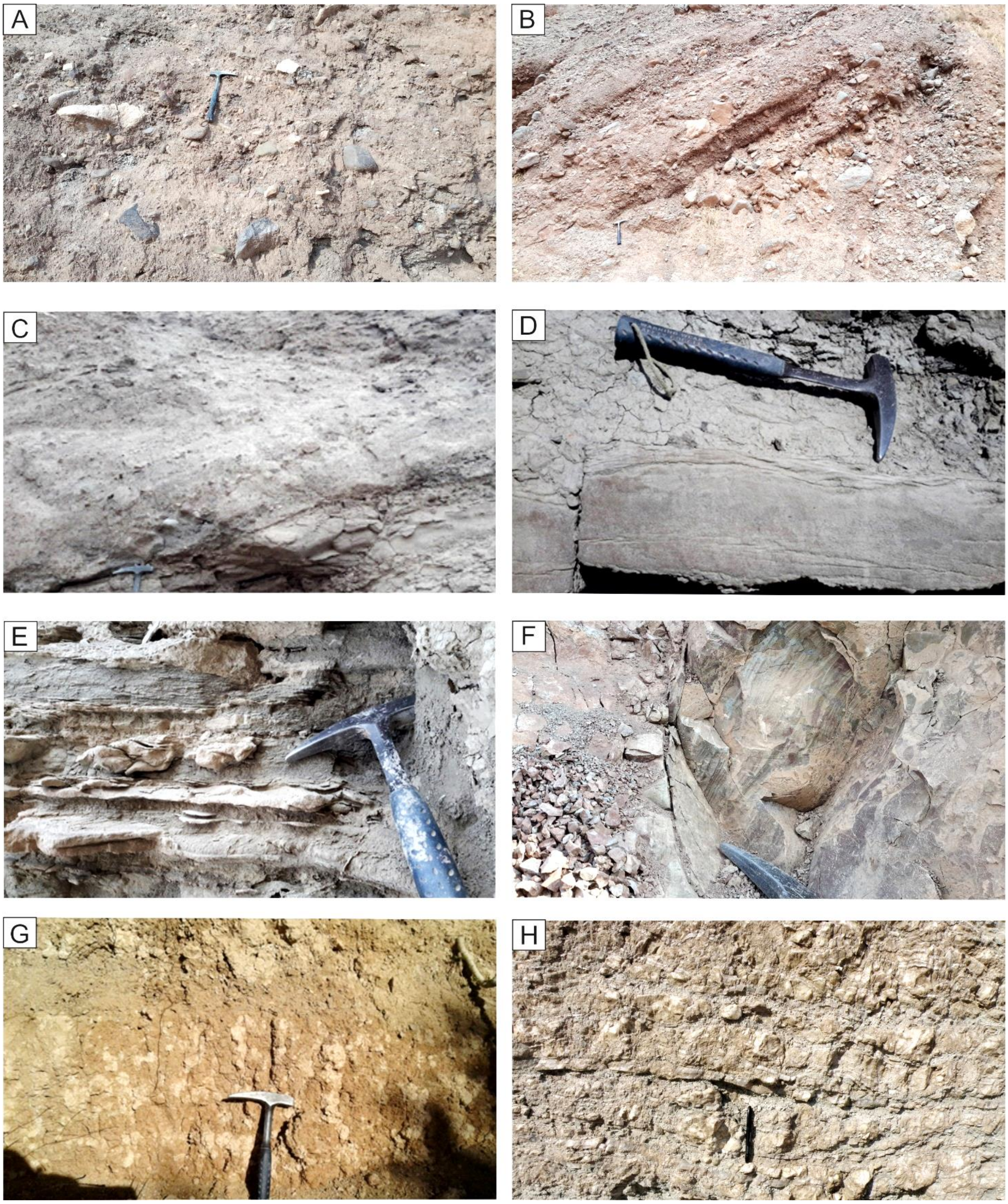

Figure 4. Close up view photographs of lithofacies characteristics. (A) Disorganised, structureless, matrix-supported, mostly monomictic (clasts are Eocene volcanics) conglomerate with subangular to angular clasts reflecting mass flow deposits (Facies code Gmd). (B) Disorganised, structureless, clast-supported, mostly monomictic conglomerate with crude bedding and subangular to moderately rounded clasts (stream-flood deposits; Gcd). (C) Conglomerates and coarse-grained sandstones with planar cross bedding representing traction current bedforms (Gp and Sp, respectively). (D) Horizontally laminated sandstone (Sl) and rippled sandstone (Sr) indicating traction currents of variable energy in sandy dominated system. (E) Lenticular bedding with symmetrical rippled sandstone (Smw) alternated with laminated mudstone (Fl) reflecting an alternation of current (bidirectional) and suspension deposits. (F) Massive structureless (Fm) to finely laminated (Fl) calcareous mudstone (suspension deposits). (G) Mudstone with carbonate nodules (P) indicating paleosol formation. (H)) Evaporate deposits (Ev) reflecting evaporation from standing water.

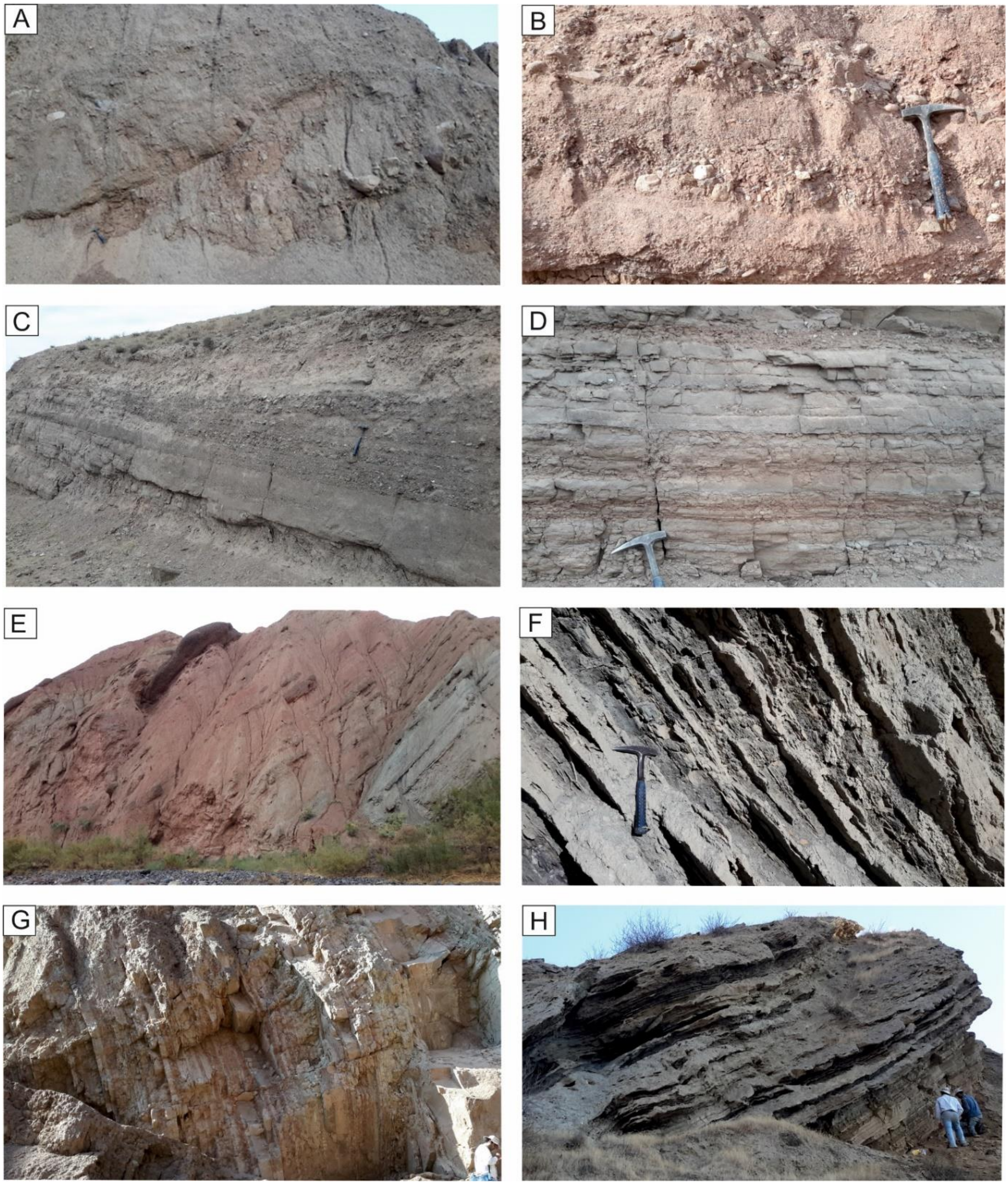

Figure 5. Representative views of different depositional systems in the Tarom Basin. (A) Disorganized granule-boulder conglomerate (facies association G1; base of KA stratigraphic section) and (B) moderately to well organized granule-boulder conglomerate (facies association G2; KA stratigraphic section) representing an alluvial fan setting. (C) Horizontally to trough cross-stratified pebbly sandstone and conglomerate in a fluvial channel (facies association S; KA stratigraphic section), of a braided river system. (D) Horizontally, thin bedded, fine grained sandstone and laminated mudstone sheets (facies associations SM; KA stratigraphic section) representing the flood plain deposits of the braided river system. (E) Overview of the braided river system with lenses of conglomerate and coarse-grained sandstone (facies association S and G3) embedded in flood plain deposits (facies associations SM; top of GH stratigraphic section). (F) Fine grained sandstone and mudstone deposits with flat geometry (facies association SM; GH stratigraphic section) reflecting deposition in the shoreface-offshore transition in a lacustrine depositional setting; the sandstone layers indicate distal storm beds. (G) Alternation of mudstone and fine-grained sandstone deposit with flat to tabular geometry (facies association SM; base of GH stratigraphic section; lacustrine depositional setting); when the mudstone dominates deposition occurred in the

offshore setting, otherwise the alternation of mudstone and sandstone indicates deposition in the shoreface-offshore transition. (H) Gypsum layers (Evaporite deposits) precipitated during short-lived desiccation episodes (facies association E, GH stratigraphic section), representing a playa lake depositional setting.

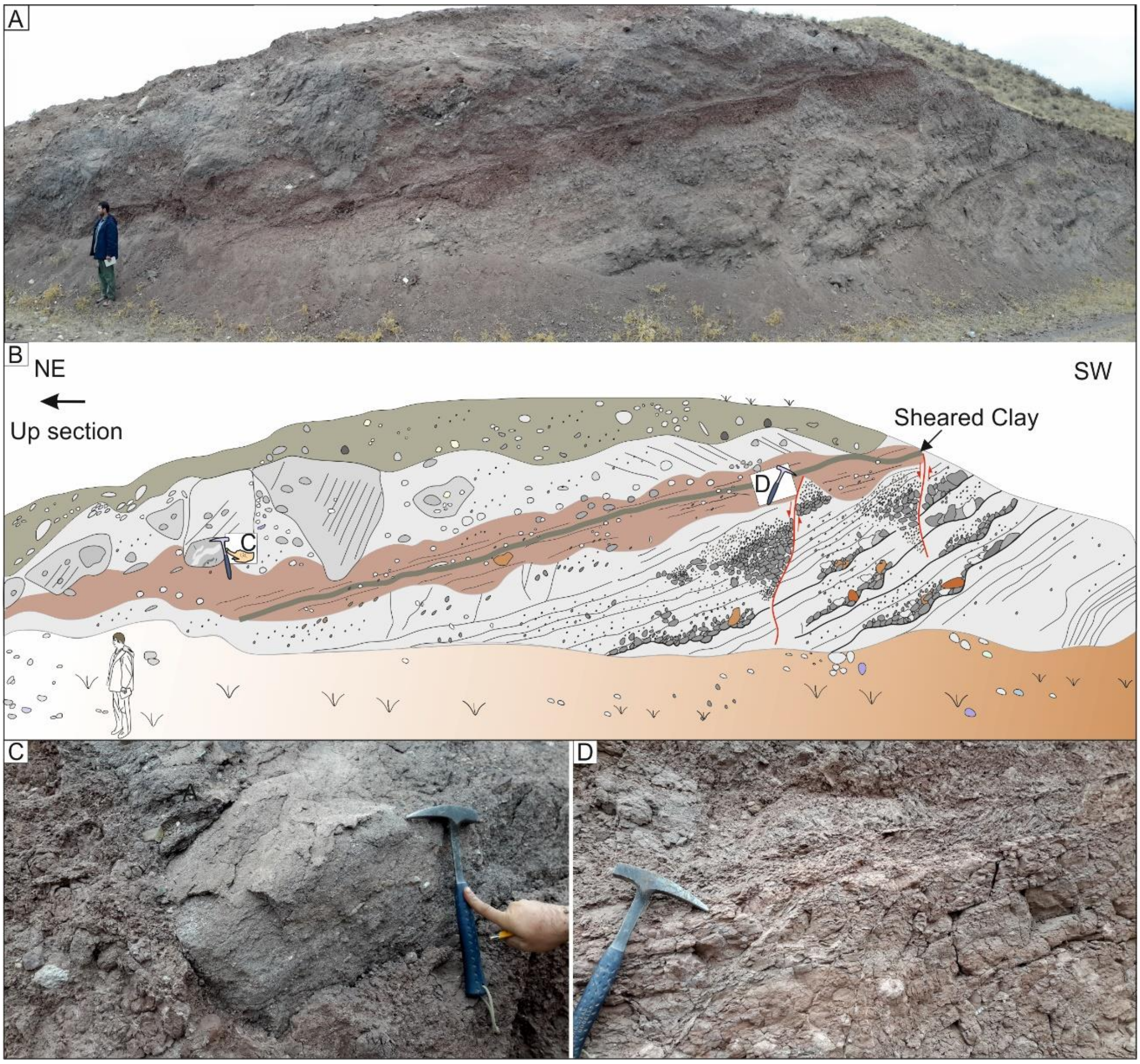

Figure 6. (A and B) Field photo and line drawing of the landslide deposits (sturzstrom) exposed along the KA stratigraphy section. These deposits consist of a chaotic, matrix supported, granules to boulder and poorly sorted breccia with a reddish matrix. This matrix includes red clays with unsorted angular clasts of variable size; at the base of the package, the clay shows shear structures that most likely formed during the fast downslope movement (facies association DB, Table 2 and facies codes Br and Mr, Table 1). Close up view of (C) a block of pebbly sandstone surrounded by a reddish matrix, and (D) sheared reddish clay at the base of the deposits.

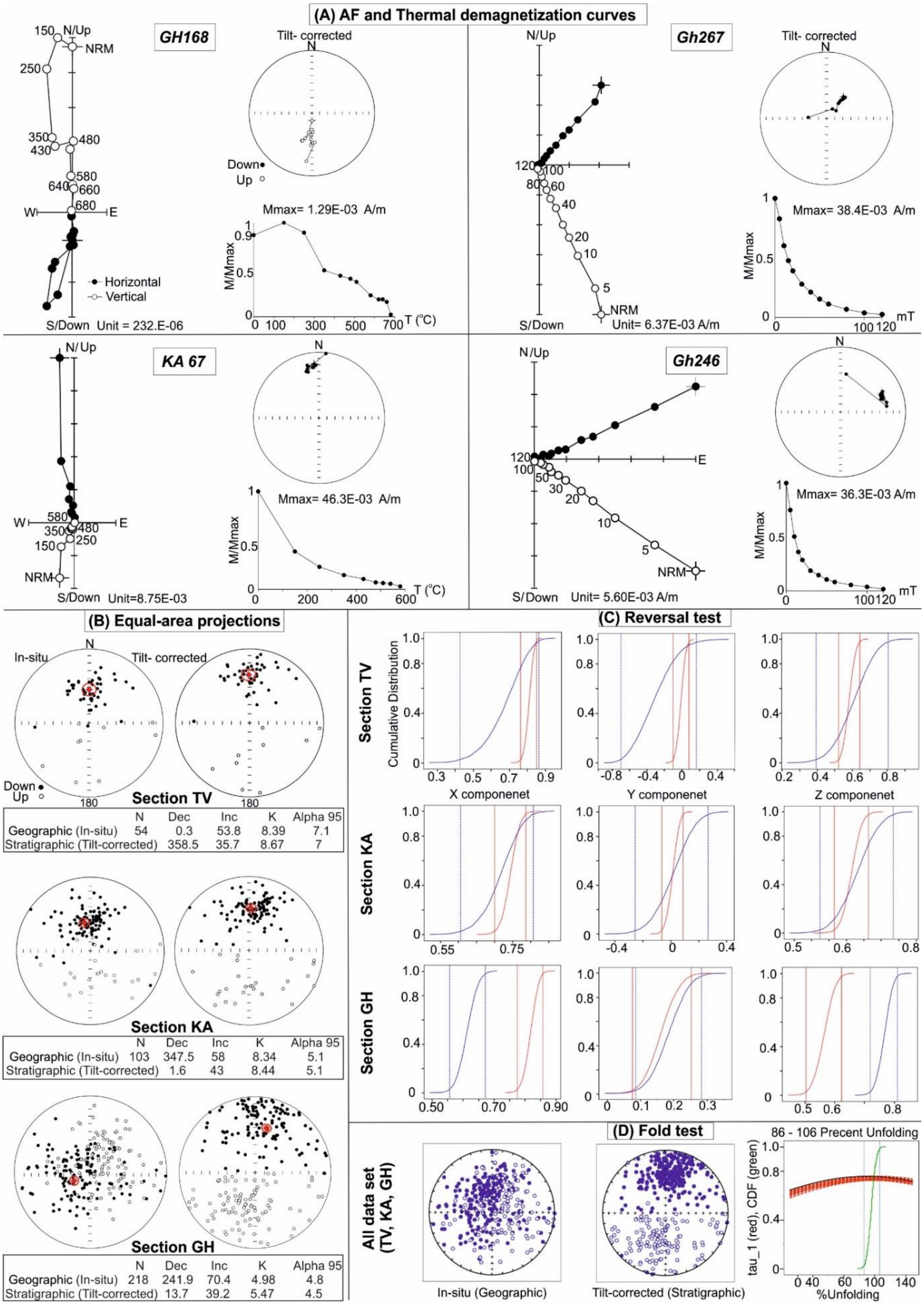

Section TV

	N	Dec	Inc	K	Alpha 95
Geographic (In-situ)	54	0.3	53.8	8.39	7.1
Stratigraphic (Tilt-corrected)	358.5	35.7	8.67	7	

Section KA

	N	Dec	Inc	K	Alpha 95
Geographic (In-situ)	103	347.5	58	8.34	5.1
Stratigraphic (Tilt-corrected)	1.6	43	8.44	5.1	

Section GH

	N	Dec	Inc	K	Alpha 95
Geographic (In-situ)	218	241.9	70.4	4.98	4.8
Stratigraphic (Tilt-corrected)	13.7	39.2	5.47	4.5	

Figure 7. (A) Representative tilt corrected diagrams of Thermal and AF demagnetization curves. The black and white circles represent the measured horizontal and vertical projections (Zijderveld, 1967). For each representative sample, demagnetization diagrams are shown in left side, intensity decay curve and sterioplot are shown in right

side. Note that solid (open) symbols in refer to the projection on the horizontal (vertical) plans, number at demagnetization step denotes the TH value in °C and the AF value in mT. (B) The overall mean normal and reverse polarity of ChRM components for three stratigraphic section TV, KA and GH sections on Equal-area stereographic projection in geographic and tilt-corrected coordinates (Dec=declination; Inc=inclination; K is estimate of precision parameter, α95 is semi-angle of cone of 95% confidence). (C) Bootstrap reversal test results and (D) Fold test results (Tauxe et al., 1991). The reversal test on TV and KA samples is positive, while GH samples show a negative reversal test. The fold test on all data set (all samples from three studied sections) is positive.

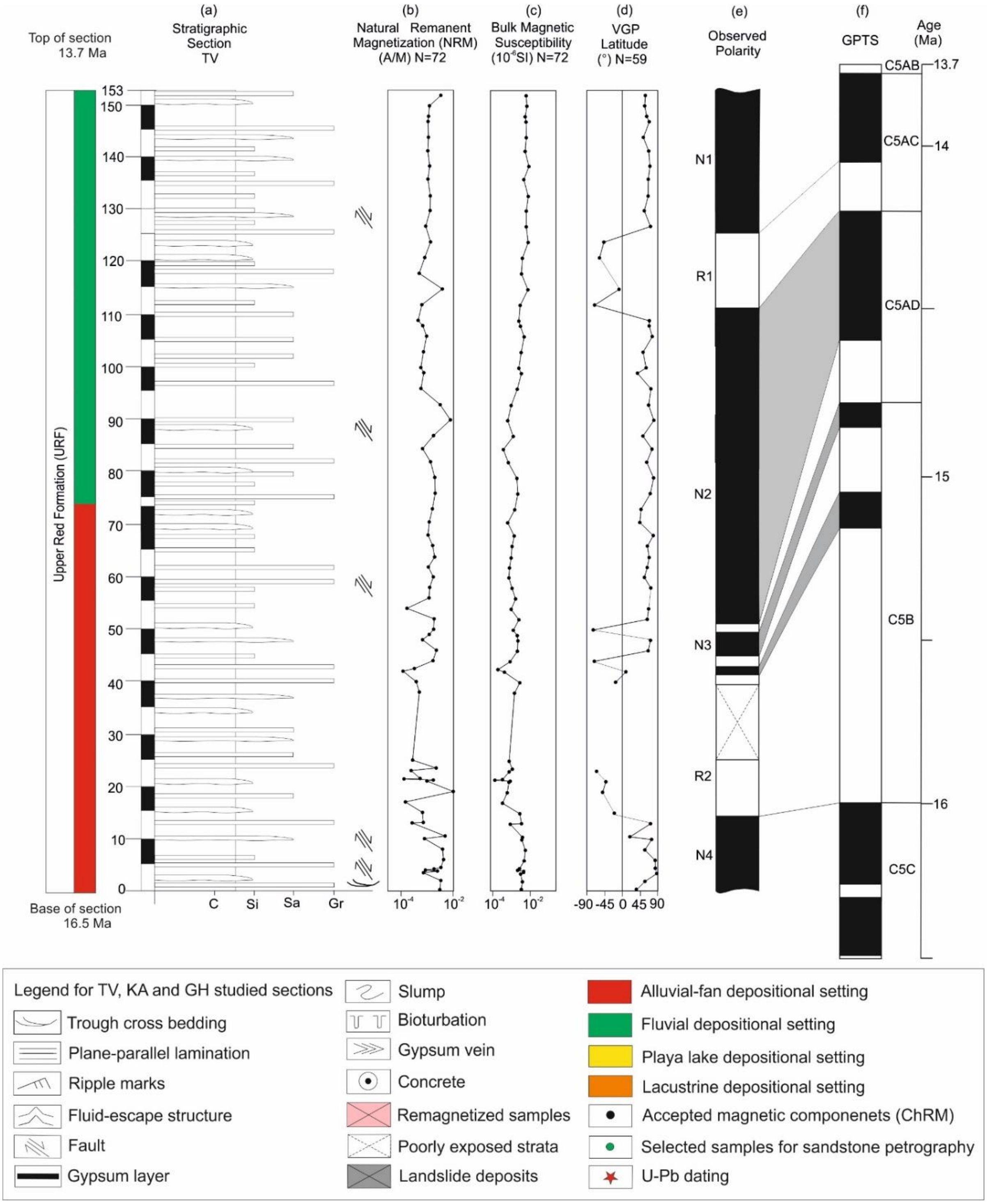

Figure 8. (A) Stratigraphic sections TV including (B) NRM (Natural Remnant Magnetization), (C) Bulk magnetic susceptibility, and (D) VGP latitude (Virtual Geomagnetic Pole). The VGP latitudes were used for constructing

(E) observed polarity scales, which were subsequently correlated each stratigraphic section with (F), the reference GPTS (geomagnetic polarity time scale) of Gradstein et al. (2012). Grey magnetozones of observed polarity scale were detected by means of only one sample.

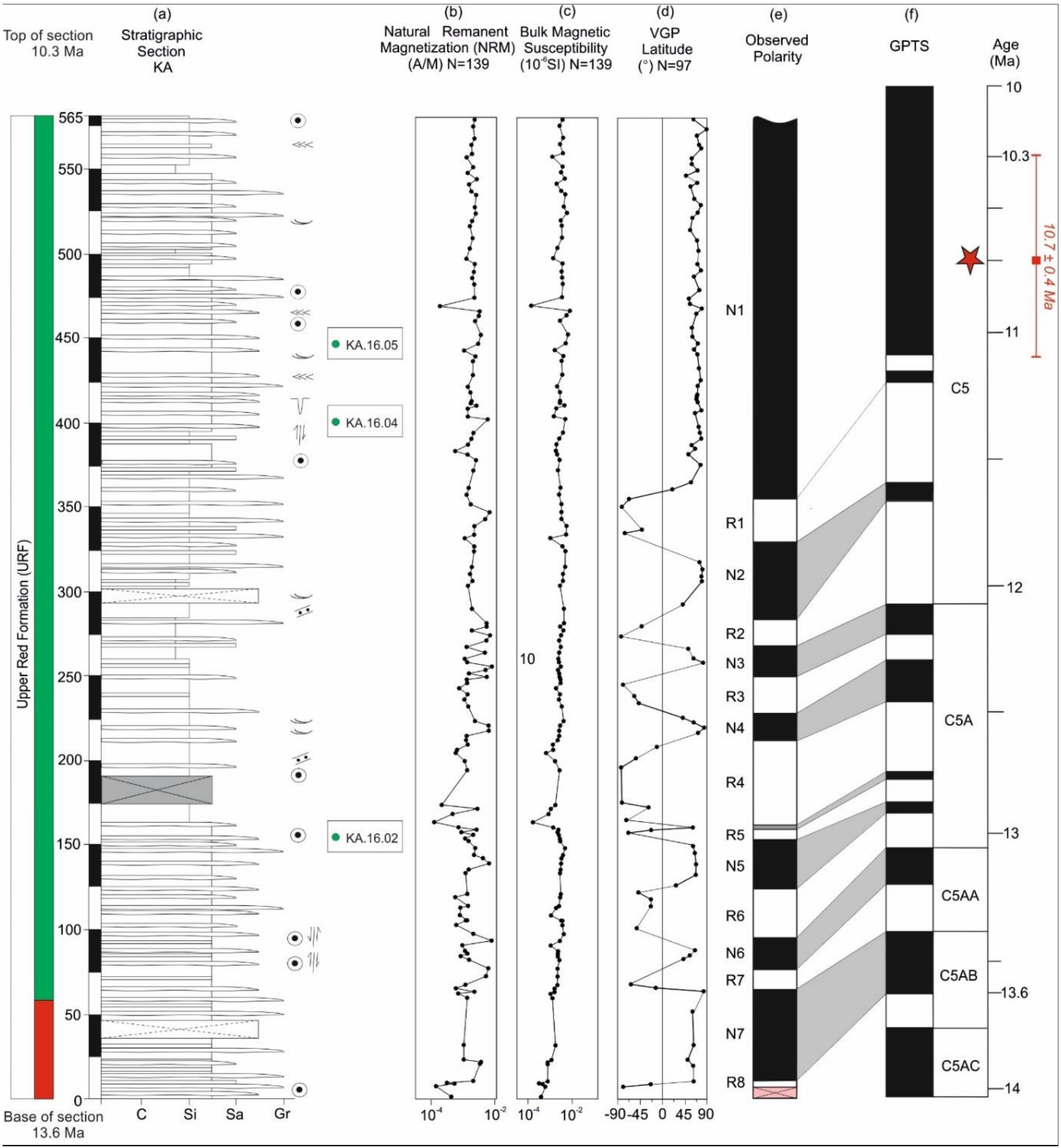

Figure 9. (A) Stratigraphic sections KA including (B) NRM (natural remnant magnetization), (C) Bulk magnetic susceptibility, and (D) VGP latitude (virtual geomagnetic pole). The VGP latitudes were used for constructing (E) observed polarity scales, which were subsequently correlated each stratigraphic section with (F), the reference GPTS (geomagnetic polarity time scale) of Gradstein et al. (2012). Grey magnetozones of observed polarity scale were detected by means of only one sample.

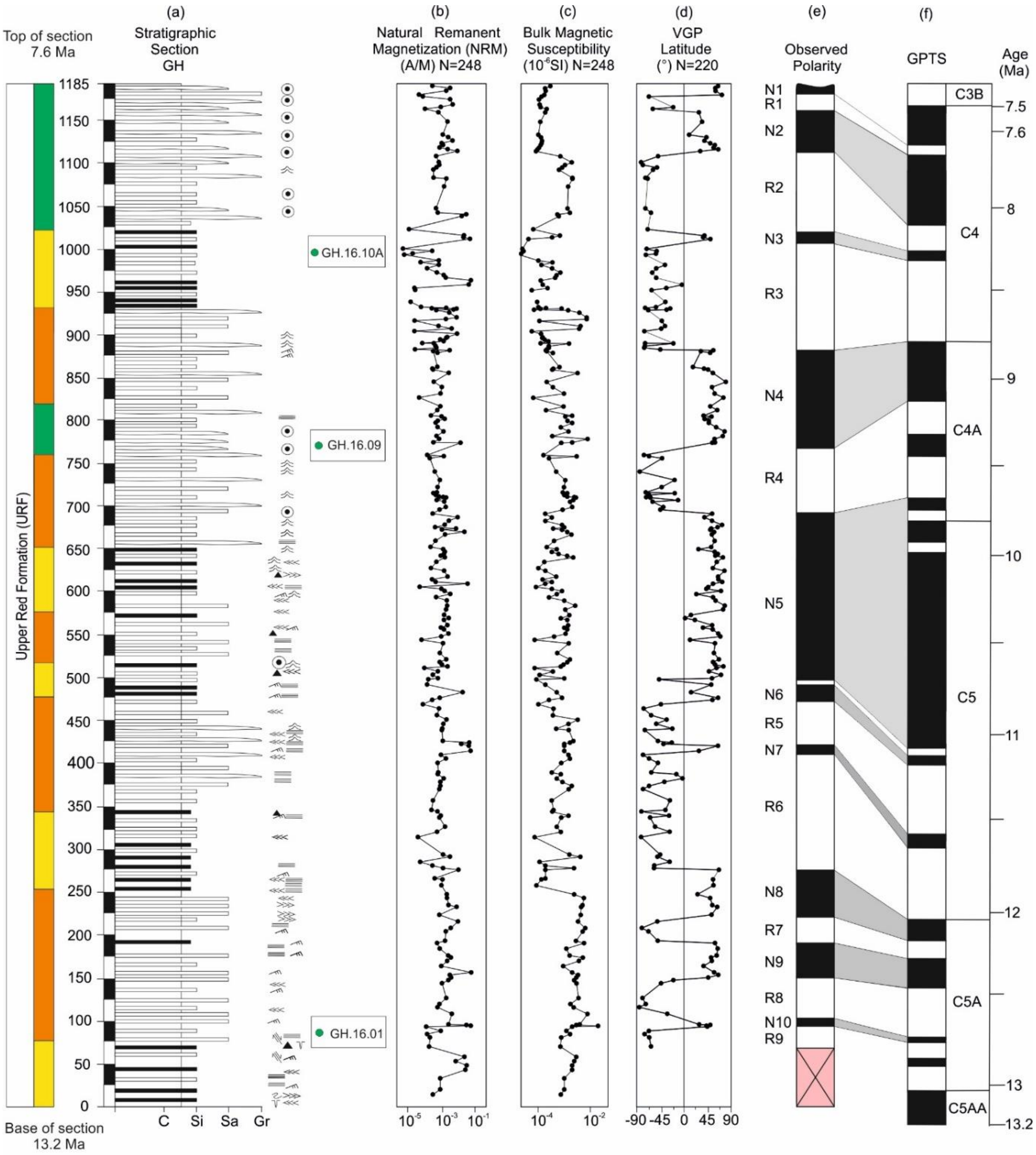

Figure 10. (A) Stratigraphic sections GH including (B) NRM (natural remnant magnetization), (C) Bulk magnetic susceptibility, and (D) VGP latitude (virtual geomagnetic pole). The VGP latitudes were used for constructing (E) observed polarity scales, which were subsequently correlated each stratigraphic section with (F), the reference GPTS (geomagnetic polarity time scale) of Gradstein et al. (2012). Grey magnetozones of observed polarity scale were detected by means of only one sample

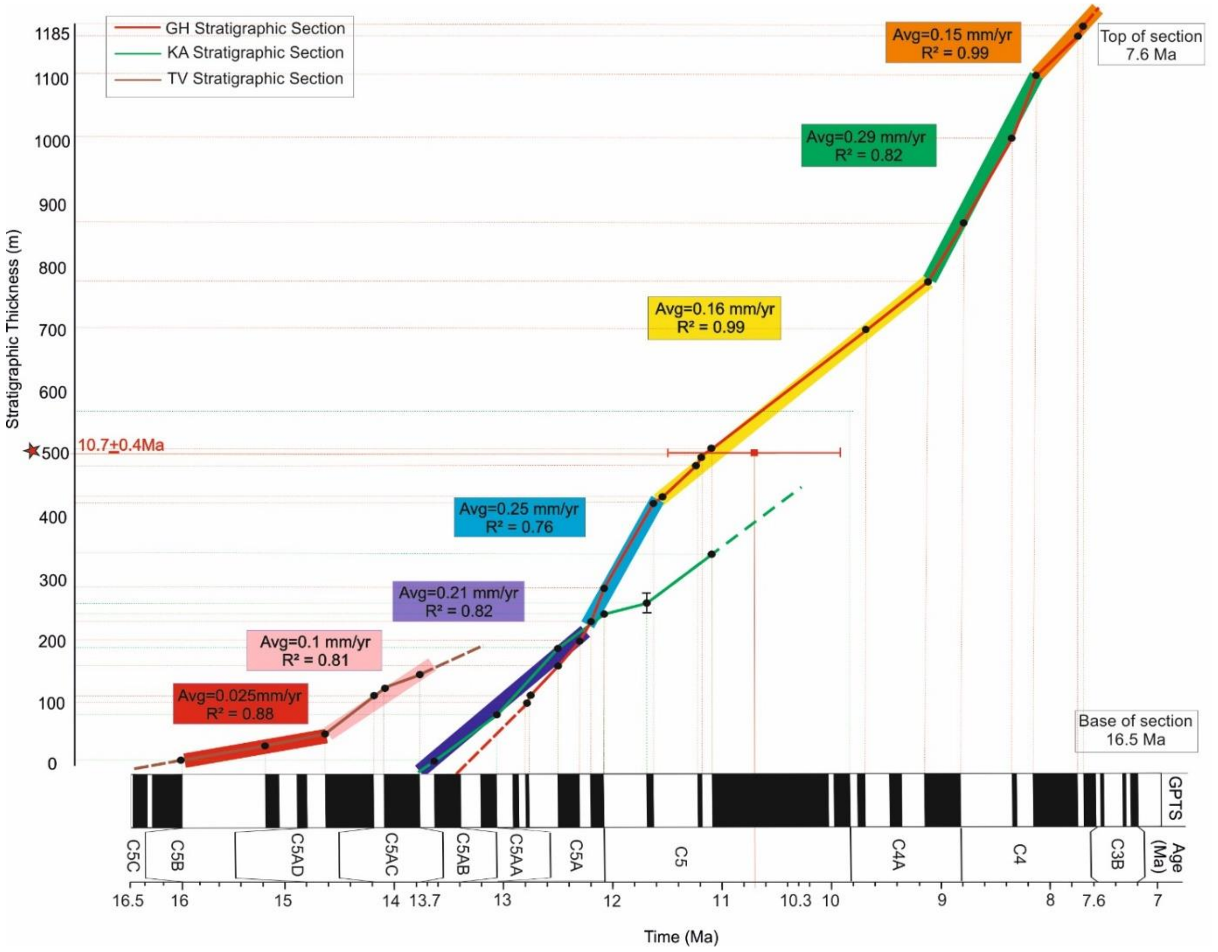

Figure 11. Long-term sediment accumulation rates for the Miocene synorogenic sediments of the three investigated stratigraphic sections. Rates have been obtained by using a linear best fit model (see correlation coefficient R^2) according to the different segments shown with the colourful boxes.

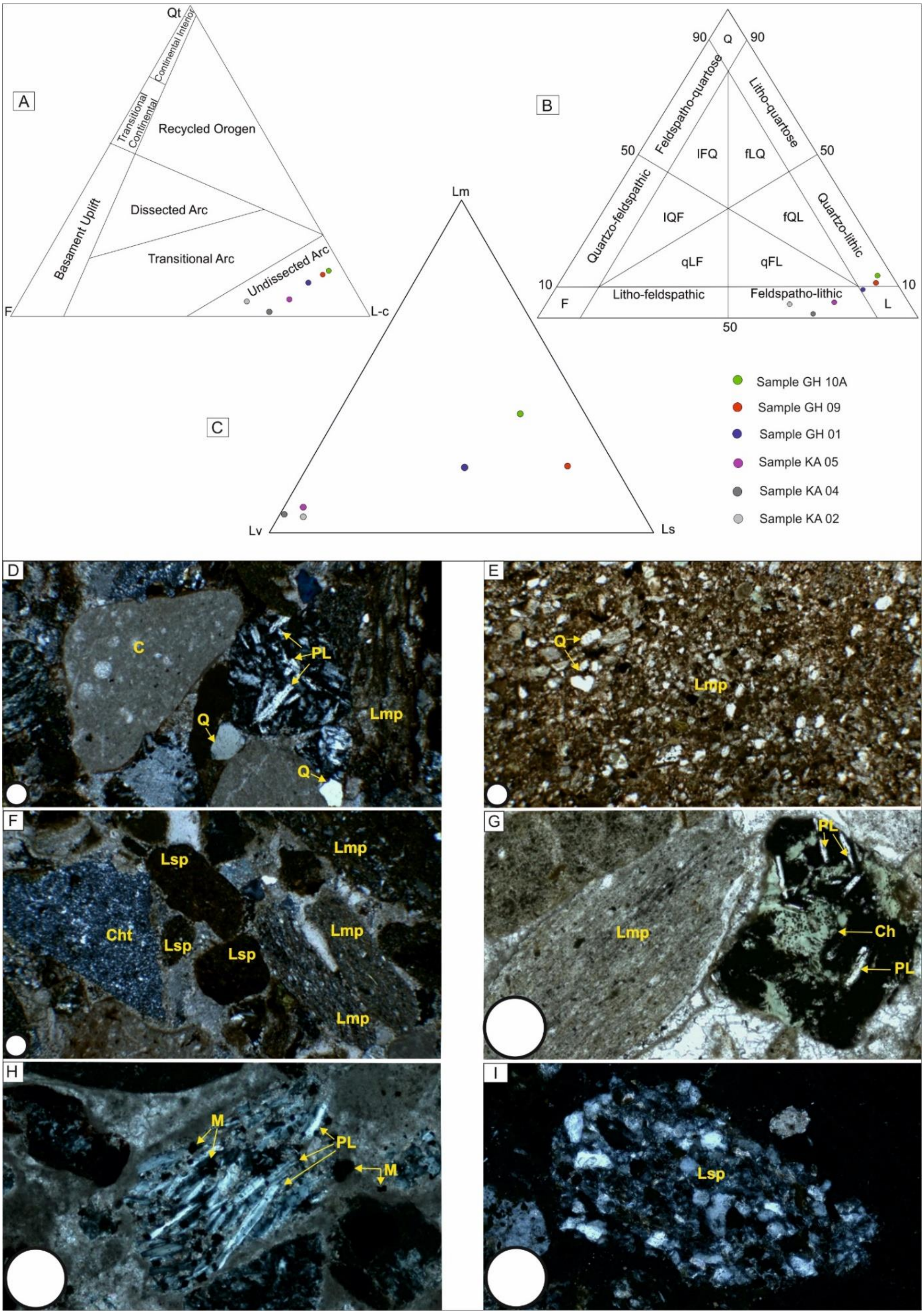

Figure 12. QFL triangular diagrams with tectonic zones defined by (A) Dickinson, (1985) and (B) Garzanti, (2019). Q represents total quartz grains (Qm = monocrystalline and Qp = polycrystalline), F represents total feldspar grains (P = plagioclase and K-feldspars), L total lithic clasts and L-c: total lithic clasts excluding

carbonates. (C) Lm-Lv-Ls ternary plot for the Tarom Basin (Lm = metamorphic; Lv = volcanic; Ls = sedimentary). (D to I) Representative photomicrographs of sandstone samples. (D) Sample GH-16-05 (stratigraphic position of ~ 410 m) showing a large calcareous grain (c), a volcanic mafic grain with plagioclases (PL), a slate fragment with rough cleavage (Lmp) and quartz grains. (E) Sample GH-16-04 (at ~ 370 m) with metamorphic clasts and quartz (Q) grains in a terrigenous-carbonatic matrix. (F) Sample GH-16-05 (at ~ 410 m) with chert (Cht), pelitic lithic (Lsp) and metamorphic fragments (Lmp). (G) Sample GH-16-10B (~ 990) showing a volcanic mafic grain (Lvm) with Pl altered in green Chlorite (Ch), and Lmp. (H) Sample KA-16-05 (~ 450) displaying a volcanic mafic grain with Pl and magnetite (M) crystals. (I) Sample GH-16-01 (~ 75 m) showing a sandy siltstone lithic fragment with detrital micas (Lsp). Note that all photos are under cross polarized light except figure F. Small and large white circles show scales of 4 and 10 microns, respectively.

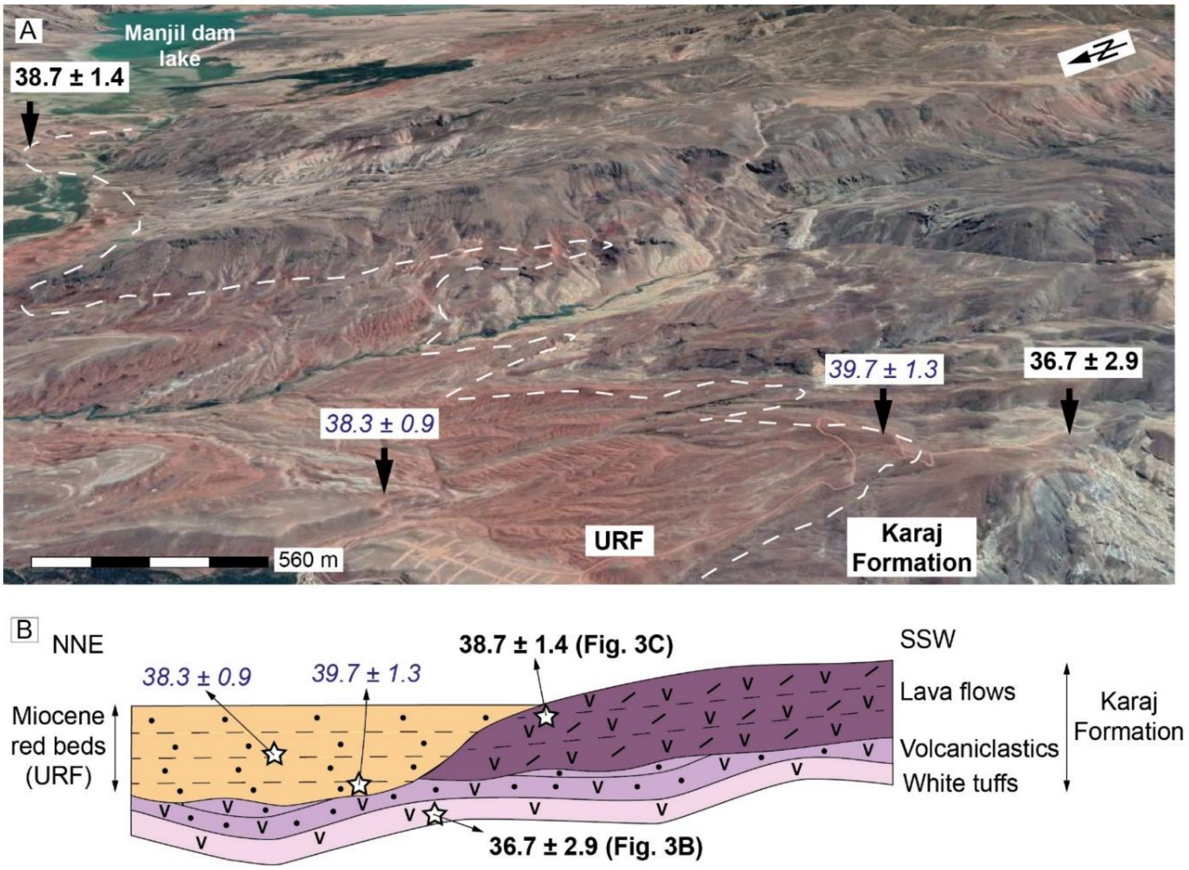

Figure 13. (A) Google Satellite Imagery showing the relationship between the Karaj Formation and the red beds along the southern margin of the basin in proximity of the Manjil dam lake (see the same ages reported Figure 1 for location). (B) Schematic cartoon showing the geometrical relationships between the top of the Karaj Formation and the red beds along the southern margin of the Tarom Basin.

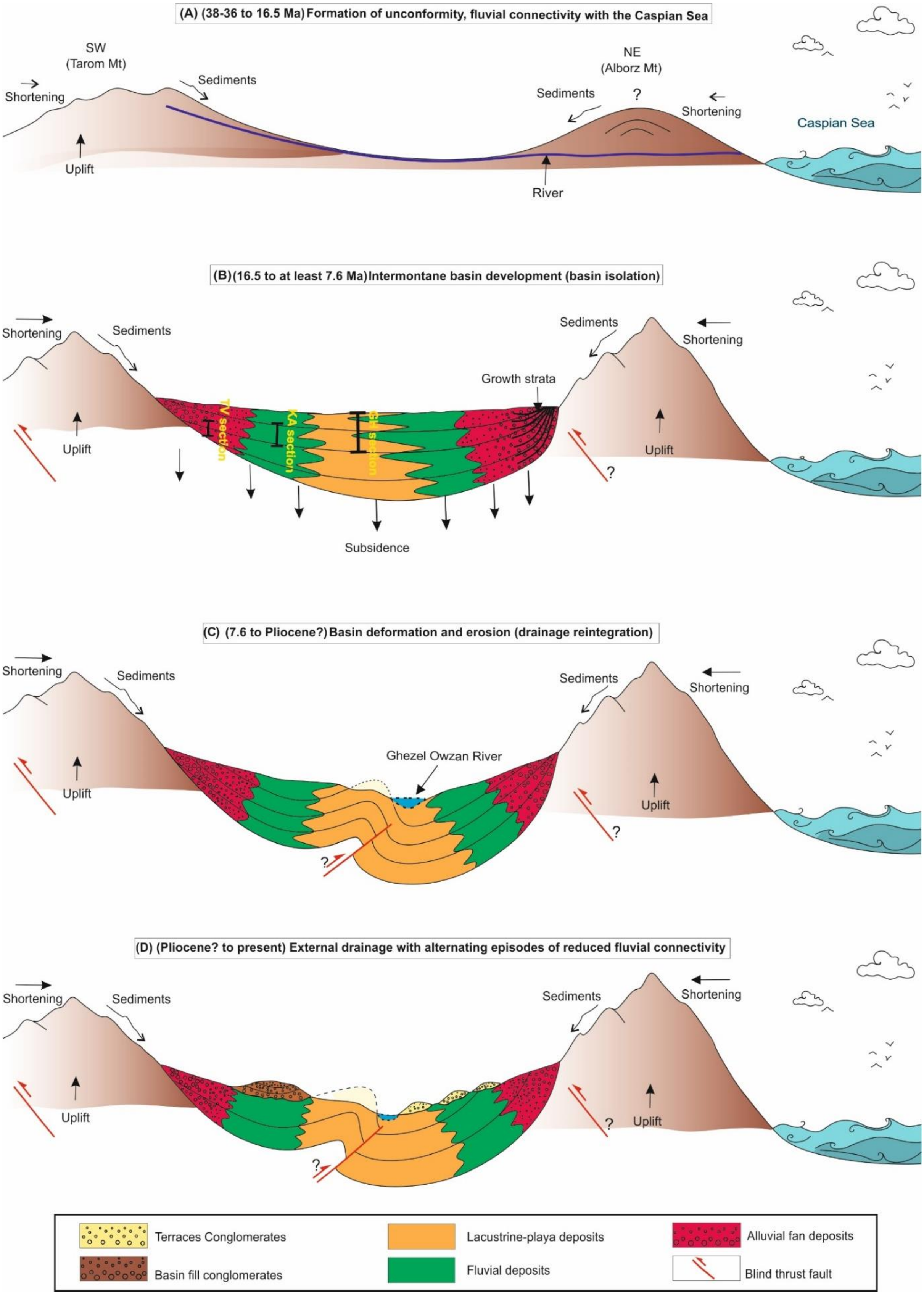

Figure 14. Schematic diagram showing the Late Cenozoic evolution of the Tarom Basin (A) ~ 38-36-16.5 Ma, uplift and tilting, formation of angular unconformities, and development of an external drainage system flowing into the Caspian Sea. (B) ~ 16.5-7.6 Ma, basin isolation and internal drainage conditions, development of an intermountain basin, uplift of the basin-bounding mountain ranges (Tarom and Alborz ranges). (C) ~7.6 Ma – Pliocene?, drainage reintegration with renewed fluvial connectivity with the Caspian Sea, intrabasinal

deformation, basin uplift and erosion. (D) Pliocene? to present, cycles of incision and aggradation, folding of basin fill conglomerates.

Chapter 3: Anisotropy of Magnetic Susceptibility (AMS) investigation as proxy for unravelling the tectonic evolution of the Intermontane Tarom Basin, NW Iran

Abstract

The anisotropy of the magnetic susceptibility (AMS) allows investigating the magnetic fabric of sedimentary rocks or unconsolidated sediments in different tectonic settings. The combination of magnetic fabric patterns with structural and sedimentologic data can provide insights into deformation or lithogenetic processes and thus it represents a powerful approach for investigating sedimentation and tectonic histories of sedimentary basins. In this work, we focus on the intermontane Tarom Basin (NW Iran) at the transition between the Iranian Plateau (IP) and Alborz Mountains. Although this basin recorded sedimentation between 16.5 and 7.6 Ma during contractional deformation associated with the Arabia-Eurasia collision, its southern margin is characterized by syndepositaional normal faults showing orogen perpendicular extension. These contrasting styles of deformation pose some questions about the mechanisms that controlled the evolution of this intermontane basin.

In order to unravel the tectonic history of the Tarom Basin, we have performed an integrated structural and AMS study on Miocene red beds from three stratigraphic sequences (named TV, KA, and GH) exposed in the Tarom Basin. Our AMS results from 357 oriented, fine-grained (mostly mudstone) samples reveal two types of magnetic fabrics: an oblate shape typical of a sedimentary magnetic fabric acquired during lithogenesis observed in ~16.5- to 10.3-My-old strata of the TV and KA sections, and a secondary oblate and prolate shape typical of a tectono-magnetic fabric that experienced layer parallel shortening (LPS) prior to folding (GH section). Our fault kinematic data from 69 faults observed mostly along the southern sectors of the basin allow us distinguishing a localized ~ N–S (TV section) and a NE–SW orogen perpendicular extension direction (KA section). The lack of correlation between the NE-SW to N-S extensional direction and the sedimentary magnetic fabric in ~16.5 to 10.3-My-old strata suggests that the Tarom Basin did not form during a phase of extensional tectonics. Thus, the observed synsedimentary normal fault must be linked to some localized processes such as gravitational instability along the tectonically growing southern margin of the basin.

1. Introduction

The importance of the Anisotropy of Magnetic Susceptibility (AMS) as a method to determine the strain pattern and the degree of deformation of sedimentary rocks or unconsolidated sediments in different tectonic settings has been recognized in many scientific studies (e.g. Saint-Bezar et al. 2002; Pares 2004; Robion et al. 2007). Specifically, AMS is a useful method to measure shape anisotropies changes and bulk-preferred orientation of different magnetic minerals such as ferromagnetic, paramagnetic, and diamagnetic minerals (Hrouda 1982; Borradaile, 1988; Tarling and Hrouda 1993; Borradaile and Henry, 1997; Borradaile, 2001; Soto et al., 2009). Previous studies that examined the sensitivity of the AMS in deformed sediments documented a systematic reorientation of the original magnetic fabric according to the associated tectonic regimes and the magnitude of deformation (e.g., Borradaile and Tarling, 1984; Kissel et al., 1986; Averbuch et al., 1992; Sagnotti and Speranza, 1993; Sagnotti et al., 1998; Parés, 2004; Cifelli et.al, 2004; Huang et al., 2006; Alimohammadian et al., 2013; Caricchi et al., 2016; Graham, 1966; Henry, 1973; Hrouda and Janak, 1976; Kligfield et al., 1977; Hrouda et al., 1978; Hrouda, 1979; 1982,; Borradaile and Henry, 1997; Lee et al., 2000; Borradaile, 2001; Soto et al., 2009; Cifelli et al., 2015; Caricchi et al., 2016). At the same time, studies conducted on undeformed sediments yielded information on sedimentary processes such as sedimentary paleocurrent directions and on compaction processes acting during diagenesis (Pares et al., 1999; Parès and Van der Pluijm, 2002; Hrouda, 1991 and Kanamatsu et al., 1996). Therefore, the AMS is a very useful technique that allows exploring the link between magnetic fabrics, tectonic strain, sedimentation and diagenetic processes.

In this study, we focus on Miocene continental deposits exposed in the intermontane Tarom Basin. This basin is located along the northern margin of the Iranian Plateau (Ballato et al., 2017) and recorded continuous sedimentation at least from ~ 16.5 to 7.6 Ma (see chapter two) during regional shortening and thickening processes associated with the Arabia-Eurasia continental collision (e.g., Allen et al., 2004; Hatzfeld and Molnar, 2010; Ballato at al., 2011; Mouthereau et al., 2012). Interestingly, these strata underwent also synsedimentary normal faulting and this appears to be in contrast with the occurrence of coeval contractional deformation. These, apparently conflicting observations, cast doubt on the evolution of the Tarom Basin. Particularly, it is not clear what processes controlled the creation of accommodation space and why normal faulting occurred during a time of widespread regional contractional deformation.

To address these issues, we have combined the study of the AMS along three stratigraphic sections (TV, KA and GH) with the kinematic analysis of syndepositional normal faults observed in the field. Our approach allowed characterizing the magnetic fabrics of the sedimentary rocks in different sectors of the basin and investigating the relationship between such a fabric, tectonic deformation and depositional processes. Combined, our data document local orogen perpendicular extension unrelated to the regional tectonic stress field. This implies that normal faulting was most likely associated with gravitational instabilities within the sedimentary basin. Overall our study highlights the importance of the AMS in unravelling the deformation history of sedimentary basins.

2. Geological setting of the Tarom Basin

The Tarom Basin is a NW-SE oriented intermontane basin located along the northern margin of the Iranian Plateau between the Tarom range to the SW, and the western Alborz Mountains to the NE (Fig. 1). The former is composed of Eocene volcanic and volcanoclastic rocks of the Karaj Formation that were deposited during Eocene in the back-arc of the Neo-Tethys subduction zone (Guest et al., 2006; Ballato et al., 2011 and 2013; Verdel et al., 2011; Rezaeian et al., 2012), whereas the latter consists of Pre-Cambrian crystalline basement rocks, Paleozoic and Mesozoic marine deposits, Eocene volcanics and volcaniclastics and intrusives of variable age, indicating a complex history of deformation, exhumation, metamorphism, magmatism, subsidence and sedimentation (Hassanzadeh et al., 2008; Zanchi et al., 2009; Brunet et al., 2003; Madanipour et al., 2017).

The Tarom Basin was filled by ~ 16.5 to 7.6 Ma red beds (see chapter two) that rest in angular unconformity on Eocene volcanics and volcaniclastics of the Karaj Formation exposed along both margins (Fig. 2). In the southern margin of the basin, these red beds are dipping few degrees to the NE (up to 20º), while the underlying volcanics are slightly steeper, except few locations where they are folded and deep to the SW (see chapter two). There, the presence of a series of steep, synsedimentary normal faults (Fig. 3) in the proximal part of the southern margin of the basin provides evidence for extension. These faults are parallel to the strike (basin elongation) and perpendicular to the shortening direction (NE-SW) of the basin. In the axial sectors of the basin the Miocene red beds are tightly folded in a system of synclines-anticlines that can be locally overturned (Fig. 2).

2.1. Stratigraphy

The stratigraphic setting and the depositional environments of the Tarom basin are reported in chapter two. There, we have presented results from two stratigraphic sections exposed along the southern margin of the basin (TV and KA sections; Figs. 4 and 5) and a third one along the northern limb of a north-verging anticline in its central sectors (GH section; Fig. 6). The TV and KA sections cover the lowermost stratigraphic interval of the basin fill (~ 16.5 to 10.3 Ma) and consist mainly of tabular, reddish or light brownish conglomerates with intercalations of mudstone and fine-grained sandstone layers and lenses (alluvial fan deposits) evolving up section into channelized sandstones with conglomerate lenses (fluvial channels) and finer-grained sediments with tabular geometries (floodplain deposits). The GH section (~ 13.2 to 7.6 Ma) consists mainly of reddish, brownish and greyish mudstones, thin bedded, mostly tabular mudstones, sandstones and evaporates. Conglomerates lenses can be also present especially toward the top of the section. These strata reflect deposition in a lacustrine and a play-lake setting evolving upsection into a fluvial system.

3. Methodology

3.1. Structural analysis

A total of 69 synsedimentary fault planes were observed in the southern and central sectors of the basin along the TV and KA stratigraphic sections (Figs. 3 and 7A-H). Fault planes measurements were coupled with the characterization of fault kinematics (direction and sense of slip) mostly by looking at slickensides and offset geological markers (primarily bedding). These data were inverted to obtain the paleostress directions by using the rotax analysis (also known as "slip normal", i.e. the line lying on the fault surface and orthogonal to the slickenlines; Salvini et al, 1999; Storti et al., 2006) available in the computer program Daisy v522e (http://host.uniroma3.it/progetti/fralab/). Fault inversion was conducted after back tilting the strata to a sub-horizontal position in order to reconstruct the orientation of the principal paleostress axes ($\sigma 1$, $\sigma 2$ and $\sigma 3$) at the time of sedimentation. Results were then compared with paleostress directions inferred from the AMS analysis (Fig. 7; see next section).

3.2. Anisotropy of magnetic susceptibility (AMS)

AMS measurements were performed to define the preferred alignment of the magnetic grains. A total of 357 samples were collected from the three stratigraphic sections with an average sampling interval of ~ 6 m. All samples were cored with a portable gasoline-powered drill and oriented by using a magnetic compass to determine both azimuth (declination) and dip (inclination) of the core axis. Each compass measure was corrected to account for a local ~ 5° magnetic declination according to the NOAA National Geophysical data center.

All AMS measurements were carried out with a Kappabridge AGICO KLY-3S susceptibility instrument, using the 15 directional susceptibilities scheme by Jelinek (1978), on a low-field intensity = 300 A/m and frequency of 875 Hz at room temperature) at the Paleomagnetic Laboratory of the Department of Sciences of the University of Roma Tre. The orientations of the AMS axes (K1> K2 > K3) and the criteria described in Jelínek (1978) was used to evaluate AMS measurements. In particular, the relationship between the parameters L (Magnetic Lineation), F (Magnetic Foliation), Pj (Corrected Degree of Anisotropy) and T (Shape Parameter) provided constrains on the shape of the AMS ellipsoid (Jelinek et al., 1981, Hrouda et al., 1982).

3.3. Magnetic mineralogy

A set of sister specimens was chosen for rock magnetic studies from the same AMS samples collected along the three stratigraphic sections. All magnetic measurements were carried out at the Institute for Rock Magnetism of the University of Minnesota, USA. Selected samples were subjected to rock magnetic studies in order to obtain detailed information about magnetic minerals identification and the main ferromagnetic carriers. Mass normalized susceptibility (χ) from all samples was measured at room temperature using both low (47 Hz) and high frequency (4700 Hz) with a Magnon VFSM.

The hysteresis measurements were carried out on a Vibrating Sample Magnetometer (VSM) using a maximum field of 1-1.5 T (depending on the samples and their lithological characteristics). These measurements were conducted to identify the magnetic mineralogy characteristics such as magnetization and remanence coercivity of magnetic particles. Thermomagnetic measurements (high magnetic susceptibility versus temperature curves) of representative samples were measured from room temperature up to 700°C using a KLY-2 KappaBridge. These measurements was performed to characterize the type of magnetic minerals of the studied samples.

4. Results

4.1. Fault kinematic results

Our faults data from the TV section exhibit a wide range of strike angles ranging from 50 to 280° average of 147°, with dip angles between 38 and 88° (an average of 65°), while faults data from the KA section display strike angle ranging from 130 to 302° (an average of 217°), and dip angle between 22 and 86° (average of 59°). Considering that these faults are synsedimentary (i.e., they are sealed by younger strata; Fig. 3) the fault inversion analysis was conducted after back tilting to the horizontal position. Our results indicate that the faults that affected the Miocene synoregenic sediments were characterized by a ~ N–S (TV section) and a NE–SW (KA section) extensional direction (with an average of ~ 178° and 216°, respectively) (Figs. 7A-H). It should be noted the value of ~ 216° represents the mean value of ~ 230° and 202° for base and top of the KA section, respectively.

These directions are perpendicular to the strike of the basin and hence are roughly parallel to the regional maximum paleostress direction inferred by previous studies in N Iran (Zanchi et al., 2009; Landgraf et al., 2010; Madanipour et al., 2017 and 2018), and to the regional Arabia-Eurasia convergence direction inferred from plate motion (McQuarrie and Van Hinsbergen, 2013).

4.2. AMS results

Our magnetic susceptibility and magnetic fabric results are shown in figures 4, 5 and 6. Samples from the TV and KA sections exhibit bulk susceptibility (k) values ranging from 170 to 10970 × 10^{-6} SI (average of 3400 × 10^{-6} SI) and 460 to 26570 × 10^{-6} SI (average of 10200 10^{-6} SI), respectively (Figs. 4 and 5. This relatively high k values are most likely related to the significant contribution of the volcanoclastic Karaj Formation, which is particularly rich in magnetite (Ballato et al., 2008). Conversely, the GH samples have lower K values ranging from 70 to 3650 × 10^{-6} SI (average of 700× 10^{-6} SI) that may reflect a more composite sediment source area (Fig. 6).

Furthermore, the TV samples do not show significant variations in magnetic susceptibility, with lower susceptibility values (average of 1600 × 10^{-6} SI) for the alluvial-fan deposits from ~ 10 to 100 m of stratigraphic thickness (∼ 16.1 to 14.2 Ma), and slightly higher values (average of 4800 × 10^{-6} SI) for the base of the section and for the fluvial deposits at the top (average of 6200 × 10^{-6} SI; ∼ 14.2 to 13.7 Ma; Fig. 4B). The KA samples yielded the lowest magnetic susceptibility values (average of 1500 × 10^{-6} SI) for the alluvial fan deposits near the base of the section (up to ~ 10 m; ~ 13.6 Ma), while the rest of the section has rather uniform k values (average of 10100 × 10^{-6} SI; ~ 13.6 to 10.3 Ma; Fig. 5B). The GH samples have a mean magnetic susceptibility of 1300 × 10^{-6} SI from the base of the section up to ~ 250 m (~13.2 to 12.1-My-old playa and lacustrine deposits) and slightly lower values with a mean of ~ 650 × 10^{-6} SI until~ 1100 m (~ 8.1 Ma). From that point, the magnetic susceptibility decreases uniformly (average of 250 × 10^{-6} SI) up to the top of the section at 1185 m (~ 7.6 Ma; Fig. 6B). Our AMS data indicate that TV samples have Pj values ranging from 1.000 to 1.109 with an average of 1.041, while KA and GH samples show Pj values varying from 1.000 to 1.112 (average of 1.039) and from 1.000 to 1.099 (average of 1.038), respectively. Concerning the shape parameter (T), the TV and KA samples show T values between 0 and 1 with a mean of 0.628 and 0.682, respectively, implying a magnetic fabric with an oblate magnetic ellipsoid (Figs. 4D and 5D; Table 1). The majority of GH samples show T values of $0<T<1$ with an average of 0.370 implying an oblate magnetic ellipsoid (Fig. 6D). Few GH samples, however, have negative T values typical of a prolate magnetic ellipsoid. Finally, the Pj and T magnetic parameters along the TV and KA stratigraphic sections have an oblate magnetic fabric with rather uniform values, while for the GH stratigraphic section the T values have a more complex pattern. They are lower in sediments younger than ca. 11.5 Ma (Fig. 6D) and consequently the mean values decrease from 0.408 to 326 after ca. 11.5 Ma (~ 425 m).

Table 1; Magnetic parameters of studied samples at each stratigraphic sections in the Tarom Basin.

Section	N	S0	Km	L	F	Pj	T	D,I (K1)	D,I (K3)
TV	73	260,20	3.90E-03	1.007	1.030	1.041	0.628	31.9/14.9	200.3/74.8
KA	100	304,18	9.89E-03	1.005	1.030	1.039	0.682	335.5/7.3	204.9/78.9
GH	184	297,66	7.03E-04	1.010	1.026	1.038	0.370	302.8/15	207.1/22.7

N = number of specimens; So = bedding attitude (azimuth of the dip and dip values); D,I (K1) = declination and inclination of the maximum susceptibility axis (geographic coordinates); D,I (K3) = declination and inclination of the minimum susceptibility axis (geographic coordinates); km = (k1 + k2 + k3)/3 (mean susceptibility, in 10^{-6} SI units); L = K1/K2 (lineation); F = K2/K3 (foliation); Pj = corrected anisotropy degree); T = shape factor (Jelinek 1981).

4.3. Magnetic mineralogy results

Our magna our magnetic mineralogy study allows characterizing the main carriers of the magnetic susceptibility. Hysteresis loops diagrams of representative TV and KA samples show a greater content of low coercivity mineral (magnetite) and a little amount of high coercivity minerals (hematite), whereas most of representative GH samples exhibit a mixture of both low and high coercivity minerals (magnetite and hematite, respectively). Thermomagnetic analysis of representative TV and KA samples indicates the occurrence of two main ferromagnetic phases, which are attributed to titanomagnetite with low titanium content (Ti-poor titanomagnetites) and magnetite. Conversely, representative GH samples are mainly characterized by a main ferromagnetic phase, suggesting the presence of both magnetite and hematite as the dominant magnetic carriers. These results appear to be consistent with our paleomagnetic data from the same studied stratigraphic sections (see chapter two). Collectively, these results suggest that the magnetic susceptibility for TV and KA samples is mostly carried by ferromagnetic minerals, while in GH samples both ferromagnetic and paramagnetic minerals are present.

5. Discussion

5.1. Origin of magnetic fabrics and tectonic reconstruction of the Tarom Basin

The combination of structural and AMS data provides information about the magnitude and style of tectonic deformation processes and hence on the strain state of rocks (e.g., Graham, 1954; Tarling and Hrouda, 1993; Parés and van der Pluijm, 2002; Soto et al., 2009; Alimohammadian et al., 2013; Cifelli et al., 2015; Caricchi et al., 2016). In case of limited or absence of tectonic deformation, however, the primary magnetic fabrics revealed by AMS will provide insights into lithogenetic processes (i.e., sedimentation and compaction for sedimentary rocks; Weil and Yonkee, 2009; Cifelli et al., 2015; Rashid et al., 2015).

Our results for the TV and KA samples document an oblate ellipsoid (0 <T <1), suggesting that these sediments experienced more compaction-induced inclination shallowing than those with spherical (T= 0) or prolate ellipsoids (T<0) observed in the GH samples (e.g, Gilder et al., 2001). Magnetic fabrics in both TV and KA samples are quite similar as the maximum susceptibility axes (K1 max) are scattered on the bedding plane with gentle sub-horizontal dip angle and without a preferred azimuthal alignment. This suggests that such a fabric is primary (sedimentary origin) and have not been obliterated by deformation processes (e.g, Cifelli et al., 2015; Rashid et al., 2015). Further, the minimum susceptibility axes (K3) are tightly grouped and perpendicular to the bedding plane (and hence vertical after back tilting), which is also typical of a primary magnetic fabric (e.g, Cifelli et al., 2015). Overall, these data indicate that the development of the magnetic fabrics for TV and KA section was controlled by flattening resulting from compaction processes during lithogenesis. Therefore, the K1 mean directions for these samples are not aligned with the extensional direction axis (σ3) defined by our kinematic analysis of synsedimentary normal faults (compare Figs. 7B with 7J and Figs.

7C-7H with 7L). This mismatch indicates that the original lithogenetic fabric was not overprinted by extensional deformation, and hence the magnitude of extension is not significant. In fact, in regions characterized by higher magnitude of stretching like extensional basins and grabens, K1 is subparallel to σ3 (e.g., Cifelli et al., 2004 and 2005).

Conversely, the magnetic fabric recorded in the GH specimens is characterized by a dominant magnetic foliation (K1-K2 trend) parallel to the NW-SE oriented bedding plane, while the minimum magnetic axis (K3 min) clusters around the bedding poles (Fig. 7M-N). This appears to agree with magnetic fabrics observed in regions subjected to layer parallel shortening (LPS) deformation. In such cases, the maximum (K1) susceptibility axis is perpendicular to the maximum compressional stress axis (σ1; shortening direction; e.g. Mattei et al., 1997; Sagnotti et al., 1998; Pares and Van der Pluijm, 2002; Cifelli et al., 2009; Oliva-Urcia et al., 2009; Cifelli et al., 2015). Thus, the comparison between the magnetic susceptibility ellipsoids (Fig. 7M-N) and the shortening direction (σ1) defined by the orientation of thrust fault systems and associated folds along the margins of the basin (Fig. 2) as well as structural analysis performed in previous studies (Madanipour et al, 2017) indicates that the magnetic fabric of GH samples is of tectonic origin with a shortening direction perpendicular to the K1 axis. Therefore, the magnetic fabric is secondary and was acquired during weekly to moderate LPS deformation (Borradaile and Henry 1997; Housen et al., 1995; Sagnotti et al., 1994; Pares et al., 1999, Cifelli et al., 2015, Rashid et.al., 2015). This event was induced by intrabasinal compressional deformation sometime after ~ 7.6 Ma and led to basin uplift and erosion (basin research manuscript). The orientation of the fabric is consistent with the orientation of the main intrabasinal structures, which are parallel to the basin bounding ranges.

Furthermore, the comparison between our AMS data from the GH section with published data from sparse samples from the Tarom Basin (here referred as Manjil samples; Mattei et al., 2017) show the same magnetic fabric in the central and northern sectors of the basin with a magnetic foliation (K1-K2 trend) parallel to the NW-SE oriented bedding planes. This implies that the magnetic fabrics observed in these regions is of tectonic origin and resulted from low to moderate NE-SW oriented layer parallel shortening (LPS; Figs. 7M-N and 7O-P). This is consistent with the occurrence of tight intrabasinal folds and a main thrust fault that bounding the northern side of the basin that led to the exposure of basement rocks.

In conclusion, TV and KA samples retain the primary lithogenetic magnetic fabric and hence did not record any extensional deformation during the development of the basin (from ~

16.5 Ma to at least ~ 10.3 Ma) despite the occurrence of syndepositional normal faults. Conversely, GH samples exhibit a tectonic magnetic fabric resulting from a more recent event (sometime after ~ 7.6 Ma) of layer parallel shortening associated with the regional collisional deformation.

5.2. Implications for basin development and causes of syndepositional normal faulting

The discrepancy between structural and AMS data for the TV and KA sections combined with the widespread occurrence of contractional structures in the basin fill (see AMS data on GH samples) and along both basin margins (e.g., Guest et al., 2006; Zanchi et al., 2009; Madanipour et al., 2017; Heidarzadeh et al., 2017) suggest that the formation of the intermontane Tarom Basin was not controlled by orogen perpendicular extension but rather by compressional deformation. This led to the growth of topography along the basin margins with the development of an endorheic basin from ~ 16.5 to 7.6 Ma (see chapter two).

If the intermontane Tarom Basin developed during widespread, regional contractional deformation, what caused synsedimentary normal faulting? The synsedimentary normal faults that were observed in the field are mostly located (if not entirely) in proximity of the southern margin of the basin. Furthermore, they do not appear to be a regional feature because we have not observed them in Middle to Late Miocene strata of adjacent sedimentary basins and so far they have not been described in other publications. It should also be noted that within the red beds of the KA section, we have found a ~12.6-My-old landslide deposits that seal some of these normal faults (Fig. 8). These disorganized deposits are matrix supported and consist of heterometric blocks (up to 2 m in size) of conglomerates and sandstones (BR manuscript). The matrix includes silty to sandy grey to red clay with a dense network of fractures filled by calcite. The base of this 2-m-thick chaotic package is characterized by a few-cm thick horizon of sheared clay (S-C fabrics). Such a fabric suggests a N-directed movement and hence must have developed during the emplacement of the landslide. The compositional similarity between the proximal Miocene red beds (see stratigraphic section TV) and the material involved in the landslide process suggests that landsliding must have affected uplifted Miocene strata of the southern basin margin.

The simultaneous occurrence of landslide deposits and normal faults in synorogenic deposits, has been observed in settings characterized by fast topographic growth associated limb rotation during folding and thrusting (Morley et al., 2007). There, the presence of faults on the limbs of growing anticlines has been attributed to gravitational instability rather than outer-arc extension which tends to be more localized on the fold crest. Similarly, the occurrence of landslide in these settings has been interpreted as the interaction between gravity-driven rock slope failure processes and fold growth, (Gamond, 1994; Morley, 2007). These processes appear to be quite common offshore (Morley et al., 2007), while in continental settings their preservation potential is limited due the occurrence of more efficient erosional processes. Additional processes that may have favoured gravitational instability in would include strata steepening along the basin margin due to the development of fault splays or duplexing at depth, and/or the presence of evaporites in the basin depocenter (Fig. 8). Overall, although the lack of subsurface data hampers our understanding of the geometric relationships between pre and post-orogenic strata as well as the extent of the normal faults at depth, our model appears to explain the occurrence of this localized and limited orogen perpendicular extension.

6. Conclusions

Our AMS document two types of magnetic fabric for the Miocene strata of intermontane Tarom Basin. The magnetic fabric for samples collected in proximity of the southern margin of the basin (TV and KA stratigraphic sections) is lithogenetic and hence developed during the formation of the sedimentary rocks (16.5 to 10.3 Ma). In particular, the magnetic parameters and the orientation of the susceptibility axis indicate that the magnetic fabric was controlled by flattening resulting from compaction processes. Conversely, the magnetic fabric in the sediments of the GH section is secondary and developed sometime after ~ 7.6 Ma during weak to moderate layer parallel shortening deformation induced by the regional NE-SW oriented compressional direction.

At the same time, our kinematic analysis of synsedimentary normal faults in ~ 16.5- to 10.3-My-old red beds document the occurrence of a ~ N–S to NE–SW orogen perpendicular extension mostly localized along the southern margin of the basin (TV and KA stratigraphic sections). The lack of a magnetic fabrics consistent with such an extension and the absence of similar faults in Middle to Late Miocene strata from adjacent basins suggests that extensional deformation must have been very minor and localized. Furthermore, these synsedimentary normal faults are sealed by landslide deposits that contain coeval blocks of conglomerates and sandstones that must have been previously uplifted. Overall, the presence of synsedimentary normal faults and landslide deposits embedded in the Miocene red beds suggests gravitational instability processes that may have occurred during the topographic growth the basin-bounding Tarom range via south-directed thrusting.

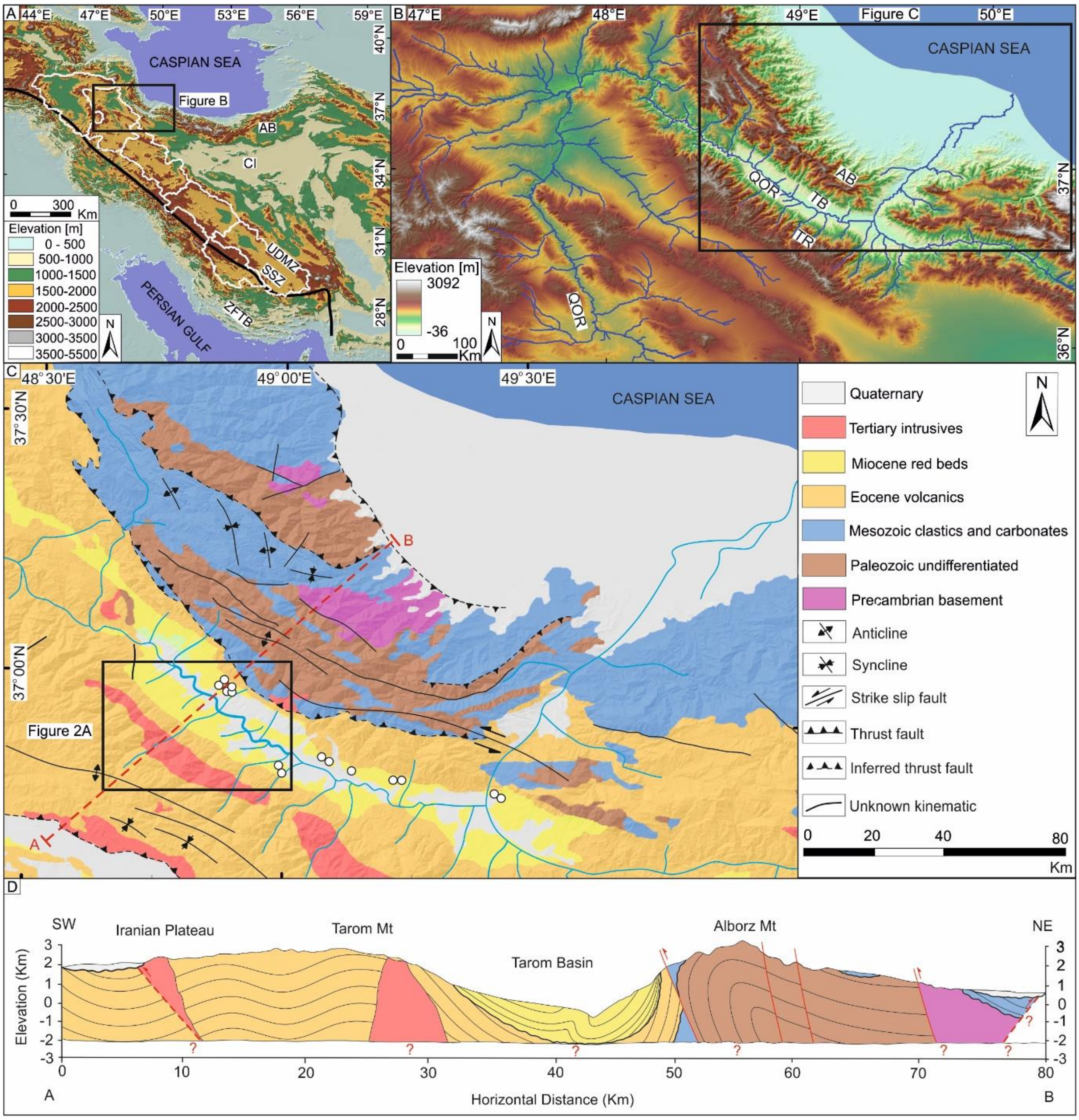

Figure 1. (A) Shuttle Radar Topographic Mission Digital Elevation Model (SRTM DEM) of Iran. The CI indicates the Central Iran Block location and the white polygons indicate six main drainage basins forming the Iranian Plateau while the black line shows the approximate location of the suture zone which separates the lower Arabian plate (and the Zagros Fold and Thrust Belt; ZFTB) from the upper Eurasian plate (Ballato et al., 2017). The Urumieh Doktar Magmatic Zone (UDMZ) and the Sanandaj Sirjan Zone (SSZ) represent the backbones and the margins of the plateau. (B) DEM of NW Iran showing the Tarom Basin (TB) and its bounding ranges, Tarom range (TR) and Alborz Mountains (AB), along the southern and the northern margins of the basin, respectively. Note the Qezel-Owzan River (QOR) drainage system (~ 55000 km^2) connecting the Iranian Plateau and the Caspian Sea trough the Tarom Basin. (C) Simplified geologic map of NW Iran. (D) Regional geological cross-section (modified after Stocklin et. al, 1969). Note that the white circles show the location of AMS sampling sites from Manjil area collected by Mattei et al., 2017.

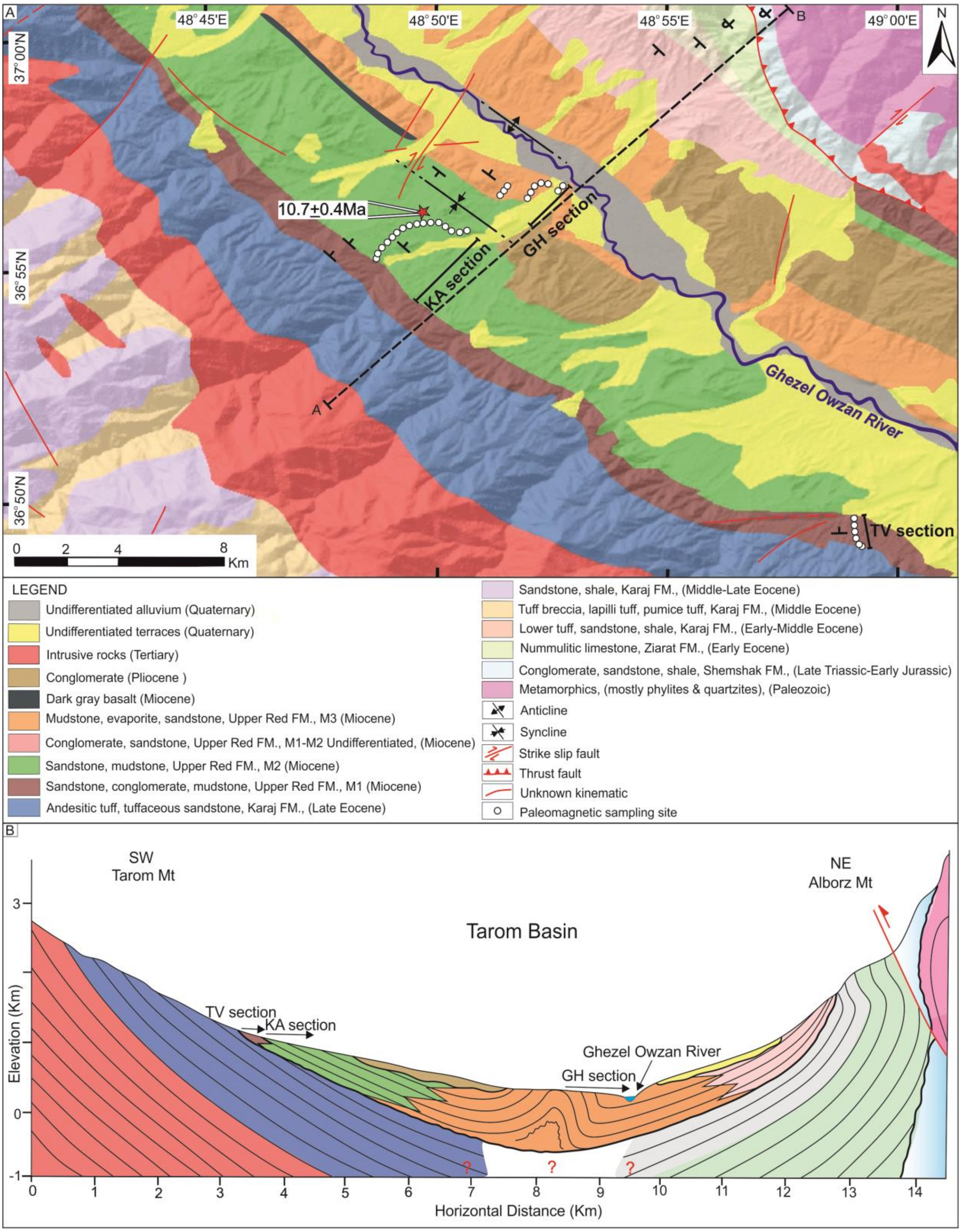

Figure 2. (A) Shuttle Radar Topographic Mission Digital Elevation Model (SRTM DEM) of Iran showing the Iranian Plateau; the white polygons indicate six main drainage basins forming the Iranian Plateau while the black line shows the approximate location of the suture zone which separates the lower Arabian plate from the upper Eurasian plate (Ballato et al., 2016). (B) DEM of NW Iran showing the Tarom Basin (TB) and its bounding Tarom range and Alborz Mountains along the southern and the northern margins of the basin, respectively. Note the Qezel-Owzan River (QOR) and its river drainage systems (~ 55000 km^2) connecting the Iranian Plateau and the Caspian Sea trough the TB. (C) Geologic map superimposed on a SRTM hillshade model of study area (TB). The white circles show the location of the three sections sampled for AMS study named TV, KA and GH. (D) Geologic cross section along line A-B.


A
SW
NE
B
NE
SW
C
S
N
D
SSE
NNW
After tectonic correction
N:12
Ang.dev: 6.8

Figure 5. Examples of synsedimentary normal faults from (A) an outcrop that is time equivalent of the top of the KA section. (B) Lower part of KA section. (C) Strata along the TV stratigraphic section and the figure (D) shows an outcrop located ~22 km to the NW of section GH. Note that the figure D included Stereoplot (Schmidt net, lower hemisphere projection; after tectonic correction of some measured synsedimentary normal faults with fault planes, slicken lines, sense of motion and paleostress axis; these fault kinematic data are not reported in the figure 7). The black dash line drawn around the yellowish package at the base of figure D shows slumped strata. Also, a synsedimentary thrust fault and a drag fold are shown in this figure.

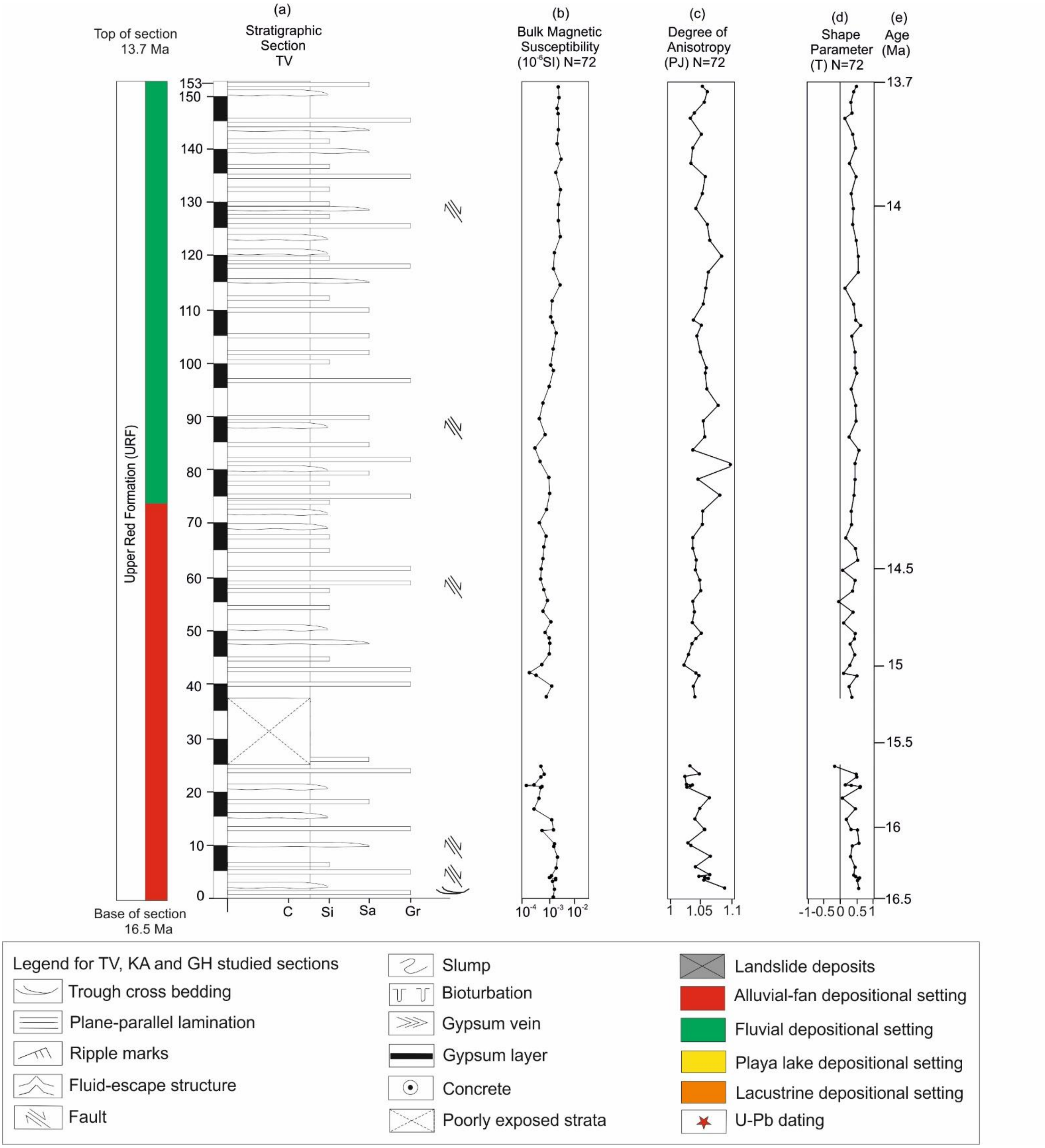

Figure 4. (A) Stratigraphic sections TV and variations of (B) bulk magnetic susceptibility (K), (C) anisotropy degree (Pj), (D) shape parameter (T) as a function of thickness and (E) age constrained from magnetostratigraphic data for the TV section.

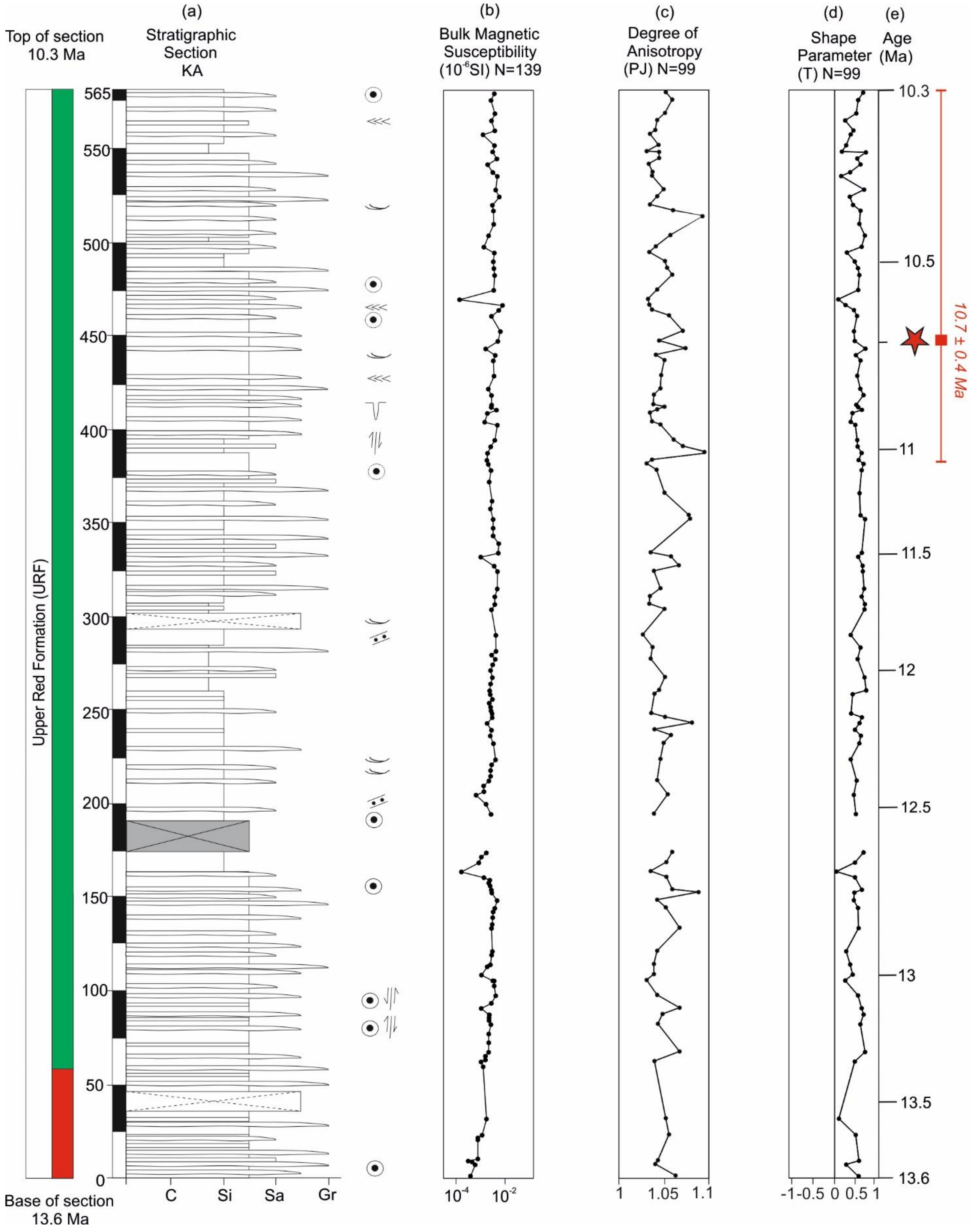

Figure 5. (A) Stratigraphic sections KA and variations of (B) bulk magnetic susceptibility (K), (C) anisotropy degree (Pj), (D) shape parameter (T) as a function of thickness and (E) age constrained from magnetostratigraphic data for the KA section.

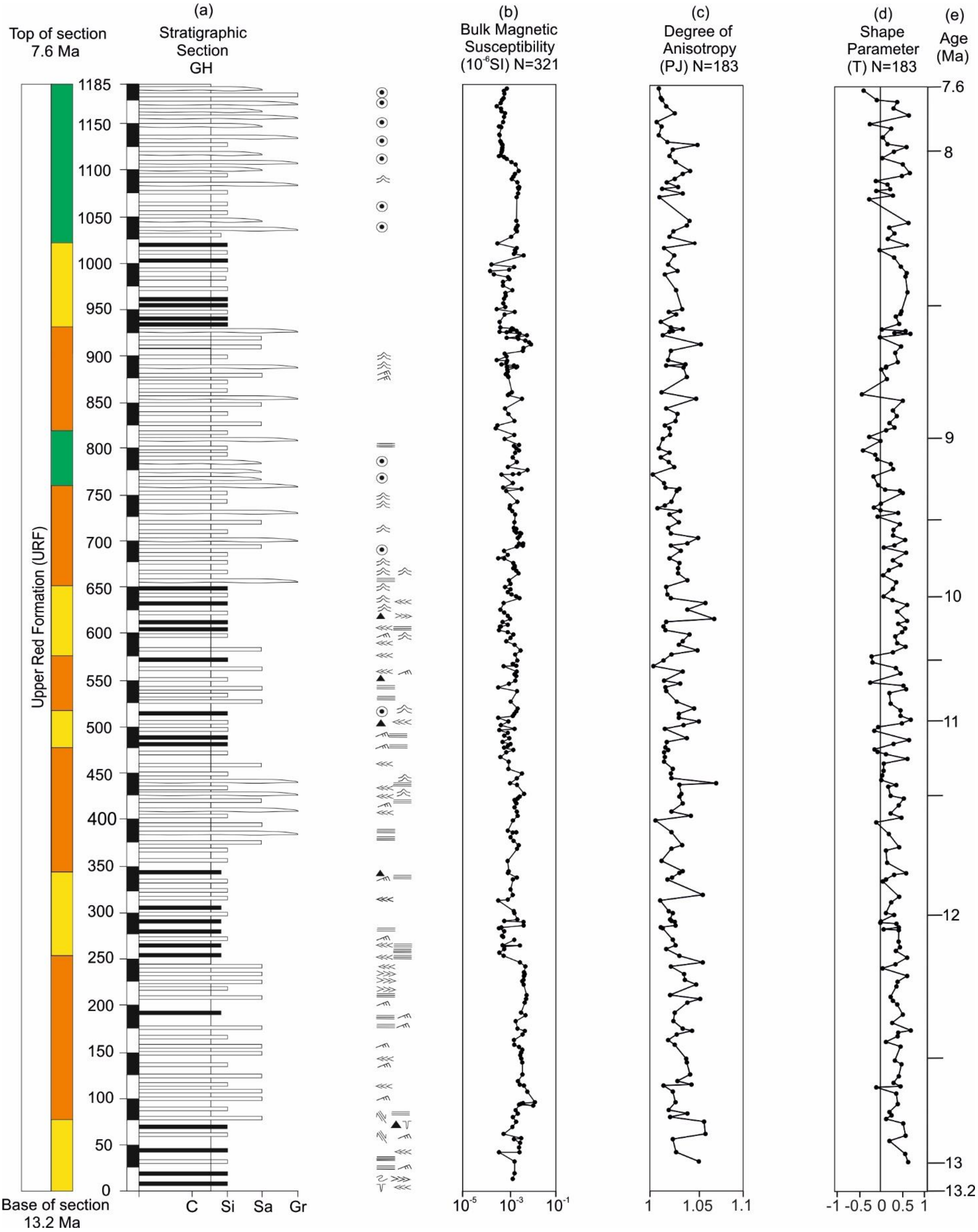

Figure 6. (A) Stratigraphic sections GH and variations of (B) bulk magnetic susceptibility (K), (C) anisotropy degree (Pj), (D) shape parameter (T) as a function of thickness and (E) age constrained from magnetostratigraphic data for the GH section.

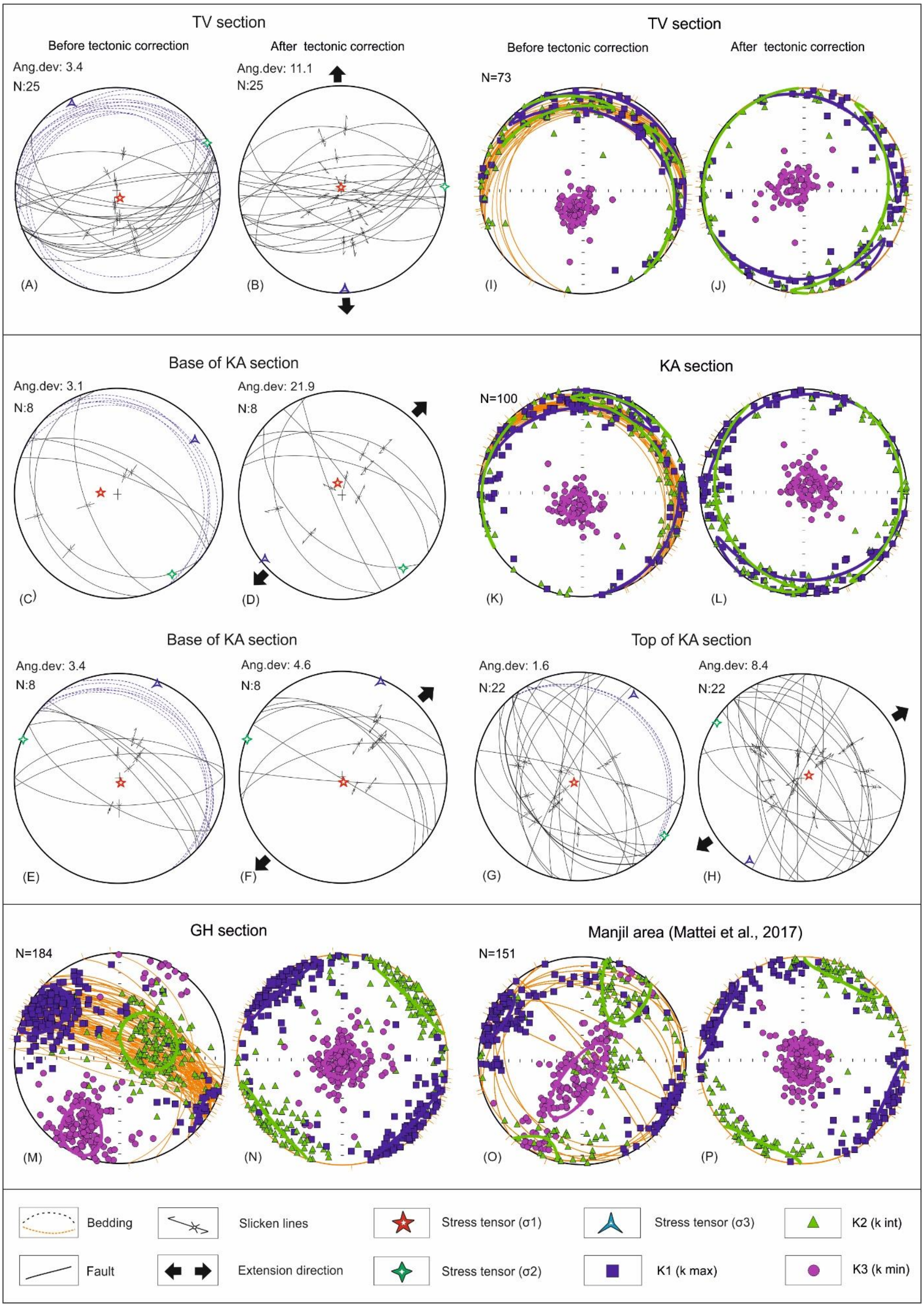

Figure 7. Stereoplots (Schmidt net, lower hemisphere projection) before and after tectonic correction of (A to H) the structural dataset including fault planes, slicken lines, sense of motion and paleostress axis, and (I to N) magnetic fabrics from the three sedimentary sections in the Tarom Basin with squares, circles and triangular

indicating orientations of maximum (Kmax), minimum (Kmin) and intermediate principal axes of magnetic susceptibility, respectively (see the methodology section for details). The magnetic fabrics (M to N) from GH studied section compared with (O and P) from studied Manjil area (Mattei et al, 2017) indicating a dominant magnetic foliation (K1-K2 trend), the same shortening direction (NE-SW) and hence tectonic magnetic fabric recorded in both regions.

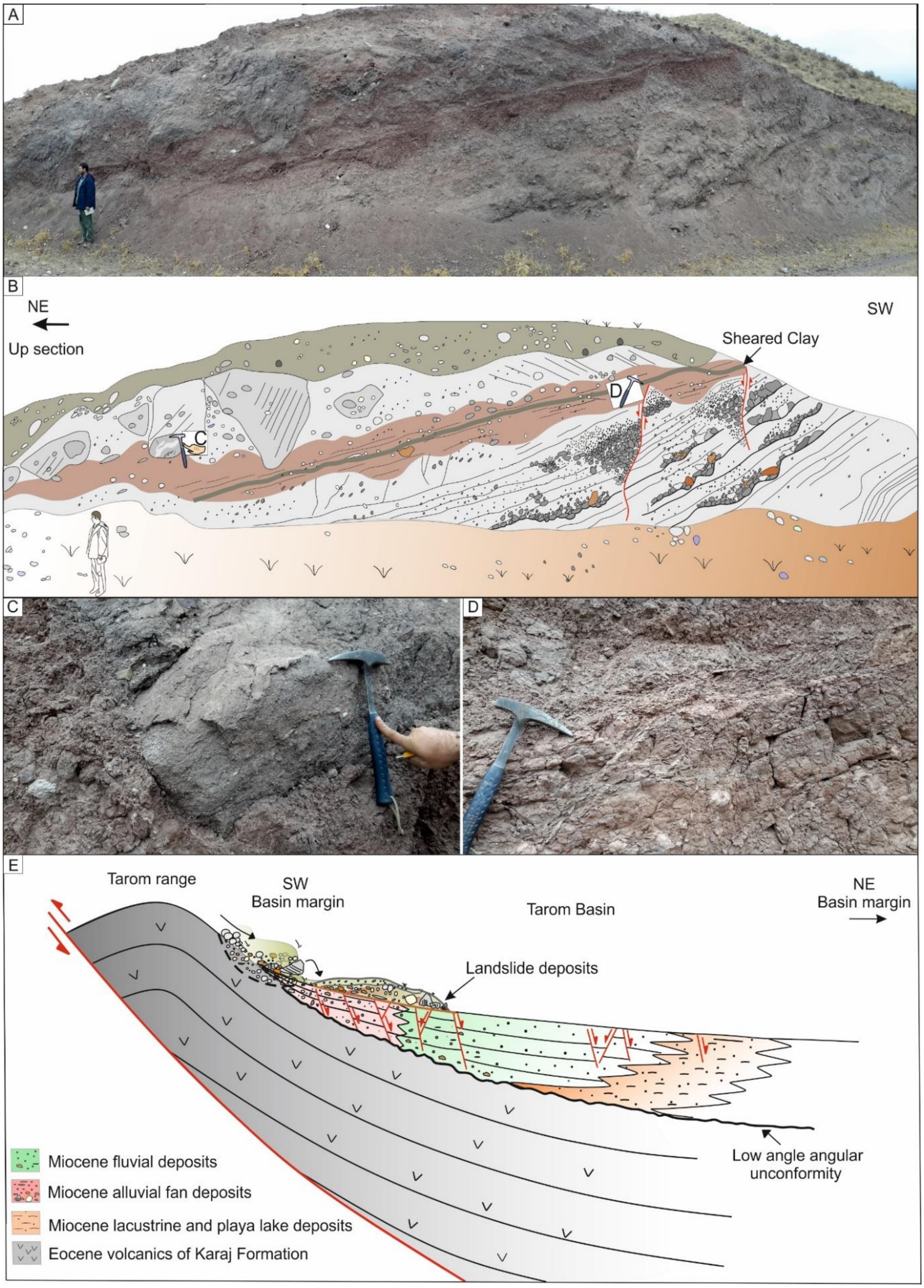

Figure 8. (A and B) landslide deposits (sturzstrom) exposed along the KA stratigraphy section. These deposits are embedded in the red beds and have an approximate age of 12.6 Ma. These deposits consist of a chaotic, matrix supported, granules to boulder and poorly sorted breccia with a reddish matrix. Close up view of (C) of block of pebbly sandstone surrounded by a reddish matrix, and (D) of the sheared reddish clay at the base of the breccia. (E) Simplified sketch showing the location of the synsedimentary normal faults with respect to the fold geometry

as well as the position of landslide deposits (black rectangle). Note that the landslide deposits sealing synsedimentary normal faults.

Chapter 4: Rock magnetic measurements on middle-late Miocene sediments from the Intermontane Tarom Basin: implications for the provenance of sediments

Abstract

Environmental magnetism is a sub discipline of paleomagnetism and rock magnetism, and represents an effective method for studying the magnetic mineralogy and other parameters such as grain-size and domain state of the main ferromagnetic carriers. One of the main advantages of magnetic mineral measurements in sedimentary rocks is that they are used as proxies for environmental changes associated with paleoclimate variations or for sediment provenance studies. Thus, sedimentary basins represent archives that offer the possibility to investigate the evolution of depositional environments, paleoenvironmental conditions and sediment provenance areas. In the present study, I focus on the intermontane Tarom Basin at the transition between the Iranian Plateau (IP) and Alborz Mountains. This basin was filled with ~16.5 to 7.6-My-old synorogenic red beds of the Upper Red Formation during the growth of the adjacent mountain range and possibly the uplift of the plateau There, I performed a complete suite of rock magnetic analysis on three sedimentary sections (called TV, KA, and GH). This approach allows documenting the concentration, remanence, of the main ferromagnetic carriers and other magnetic characteristics of the sediments associated with changes in past climate, in the sediment source area and in the depositional settings.

Overall, my data show that the sediments along the southern margin of the basin (TV and KA sections) have higher susceptibility, and lower coercivity and remanence values than those exposed in the central sectors of the basin (GH section). Moreover, they are mainly composed of ferromagnetic minerals such as magnetite (and Ti-poor titanomagnetites) indicating that they were only sourced from Tarom range which is composed of Eocene volcanic rocks of the Karaj Formation. Conversely, the sediments in the central parts contain a mixture of paramagnetic (clay minerals) and ferromagnetic minerals such as Ti-poor titanomagnetites magnetite, maghemite and hematite, implying that were sourced from both margins of the basin (Tarom range in S and Alborz mountains in N).

1. Introduction

Rock magnetic studies provide information on the magnetic properties of rock forming minerals and hence can have a wide range of application. For example, they can be used for detecting major changes in sediments provenance as well as in environmental and/or climatic conditions (Moreno et al., 2002; Maher, 2007; Heslop and Roberts, 2013; Zan et al., 2015). Furthermore, they are fundamental in paleomagnetic studies for interpreting demagnetization curves and isolating primary from viscous (secondary) components. In this chapter, I am presenting newly acquired results from the Miocene red beds of the Tarom Basin sampled for magnetostratigraphic dating (see chapter 2) and AMS analysis (see chapter 3). The goal of this study is a detailed characterization of the magnetic mineralogy in order to get new insights into the evolution of the Tarom intermontane basin and adjacent mountain belts. The analytical results have been obtained only recently, therefore, I report the main outcome of the analysis with some preliminary conclusions.

2. Methods

In this study, a set of sister specimens (in total 524) was chosen for rock magnetic studies from the same paleomagnetic samples collected along the three stratigraphic sections (TV, KA and GH) described in chapters 2 and 3. All magnetic measurements were carried out at the Institute for Rock Magnetism of the University of Minnesota, USA.

Selected samples were subjected to rock magnetic studies in order to obtain detailed information about magnetic minerals identification, main ferromagnetic carriers, and their domain state as well as grain-size analysis. In the following, I provide a brief description of the techniques I used Mass normalized susceptibility (χ) from all samples was measured at room temperature using both low (47 Hz) and high frequency (4700 Hz) with a Magnon VFSM. Frequency-dependent susceptibility (χfd), defined as [(low χf − high χf)/ low χf Hz × 100٪], was determined from these measurements.

All samples were also subjected to a 3-axis alternating field demagnetization with a maximum field of 170 mT. After demagnetization, samples were subjected on anhysteretic remanent magnetization (ARM) in an arbitrary direction using a direct current bias field (DC field) of 0.05 mT. The anhysteretic susceptibility, χARM, was determined by normalizing the remanent magnetization by the strength of the bias field. Remanence measurements were performed in magnetically shielded room with a 2-G Superconducting Rock Magnetometer.

Hysteresis loop parameters including saturation magnetization (Ms), saturation remanence (Mrs), coercive force (Hc), remanence coercivity (Hcr), and backfield demagnetization curves were measured for a subset of 234 samples from the three stratigraphic sections on a Vibrating Sample

Magnetometer (VSM) using a maximum field of 1-1.5 T (depending on the samples and their lithological characteristics). The hysteresis measurements were conducted to identify magnetic mineralogy, domain state, and magnetic interactions among magnetic particles (Day et al., 1977; Roberts et al., 2000). The correction for paramagnetic contributions was also done on measured samples. In addition, I performed thermomagnetic measurements (high magnetic susceptibility versus temperature curves) to characterize the magnetic mineralogy of the studied samples. Fifty representative samples were powderized first and then weighted. The variations in magnetic susceptibility of the powdered specimens were measured from room temperature up to 700°C using a KLY-2 KappaBridge.

Remanent magnetization measurements as a function of low temperature were also performed on 38 selected samples to identify the type of magnetic minerals and characterize their rock magnetic properties. These experiments were done on Magnetic Properties Measuring Systems (MPMS) with both Big Red and Old Blue Mumpsies instruments using two different sequences. In the first sequence (FC-ZFC-LTSIRM) each specimen was subjected to a sustained DC field (2.5T) at 300 °K in a short duration of time (~1 min). Magnetic remanence measurements have been performed as the specimen cooled down to a specified low temperature (20 °K) and subsequently warmed back up to 300 °K. This experiment generated the FC and ZFC remanence curves. In the second sequence (FC-ZFC-LTSIRM-RTSIRM) more detailed sequence were done on samples and consequently more information extracted from samples. This experiment generated the FC, ZFC and RT remanence on cooling and RT remanence on heating curves.

3. Results and interpretations of the magnetic mineralogy

3.1. Thermomagnetic analysis

Temperature-dependent susceptibility (K–T curves) are sensitive to magnetic mineralogical changes during thermal treatment (Hunt et al. 1995; Deng et al. 2001, 2004). Thermomagnetic properties were measured to determine the Curie temperature of a particular magnetic mineral or phase. My thermomagnetic results for all representative samples show irreversible heating and cooling (χ –T) curves (Fig. 1). Both TV and KA samples are mainly characterized by two main ferromagnetic phases. For the first phase, the heating curves show drops at Curie temperatures between ~ 450° and 550ºC, which are attributed to a titanomagnetite with low titanium content (Ti-poor titanomagnetites). For the second phase, the heating curves decrease near a temperature of 580ºC, suggesting that magnetite is the dominant ferromagnetic carrier. Some representative heating curves, however, are followed by a further decrease after 600ºC, in the range between 600ºC – 640ºC, suggesting the presence of maghematite?/ hematite (Fig. 1). This is also consistent with my paleomagnetic data from the same stratigraphic sections (see chapter 2). Representative GH samples are mainly characterized by a main ferromagnetic phase with Curie temperatures decrease at ~ 580ºC, followed by a further decrease after 600ºC, so that the magnetic susceptibility curve persists and does not disappear completely until about 680ºC. This indicates that magnetite is the dominant ferromagnetic carrier with a minor content of hematite (Fig. 1). In some representative GH samples, however, the magnetic susceptibility curve persists until about 680ºC, suggesting that hematite is the dominant ferromagnetic carrier. Furthermore, K –T measurements for all GH samples show that the magnetic susceptibility values are much higher in the cooling than in the heating curves, indicating that new magnetic minerals formed in a ferromagnetic phase during heating (Fig. 1) (Liu et al., 2005).

3.2. Magnetic hysteresis

A hysteresis loop shows the behaviour of ferromagnetic particles in response to an applied magnetic field and can provide essential information such as the variation of magnetization and the domain state of the magnetic carrier (Day et al., 1977, Tauxe et al., 1996, Dunlop & Ozdemir, 1997, Dunlop, 2002).

Hysteresis loops results for representative TV and KA samples show a mixture of both, low and high coercivity minerals, suggesting the presence of both magnetite and hematite, respectively. However, as shown in figure 2, these samples exhibit a greater content of low coercivity mineral (magnetite) and very little content of high coercivity minerals (hematite). The low coercivity minerals

(also called soft magnetic materials), are hence dominant as indicated by the narrow shape of the hysteresis loops with a maximum coercivity of ~ 100 to 300 mT, implying that magnetite and probably pigmentary hematite are the dominant remanence carriers. This suggests that these samples were sourced by a uniform lithology such as the volcanic and volcanoclastic deposits exposed along the southwestern margin of the basin (Karaj Formation of Eocene age).

The hysteresis loops for most of the representative GH samples exhibit a mixture content both, low and high coercivity minerals (magnetite and hematite, respectively). Thus, these samples are dominated by a low coercivity mineral with a narrow shape in the lower field (~ 100 to 300 mT) and also by a high coercivity mineral, (also called hard magnetic materials) with a wide shape of hysteresis loops in the higher field and a saturation of the IRM acquisition curve above ~ 100/300 mT (Fig. 2). This mixture of magnetic phases suggests that in contrast to the TV and KA deposits, the GH sediments were sourced from a more complex and less uniform sediment source area including Eocene Volcanic of the Karaj Formation (mostly sourced from the southern margin but also from the North) as well as Triassic Sandstones and shales (Shemshak Formation) and Pre-Cambrian metamorphic rocks along the northeastern margin of the basin.

The remanence ratios (Mrs/Ms) versus hysteresis rations (Hcr/Hc) were plotted after obtaining the coercivity of remanence (Hcr) values by backfield demagnetization Mrs. This was done to estimate the average grain size of the magnetic minerals by means of the Day diagram (Day et al., 1977 & Dunlop et al, 2002) and the squareness-coercivity (SC) plot (Tauxe et al., 2002 and Wang & Van der Voo, 2004). The Day diagram indicates that the magnetic grain sizes of all studied samples plot within the pseudo-single domain (PSD) region of magnetite (Fig. 3A). Also, in the Day plot, the TV and KA samples exhibit different hysteresis behaviour and they are more clustered than GH samples. This suggests that the pseudosingle-domain magnetite grains contain more effective remanence carriers with higher coercivities which saturate above 100 mT (Deng et al, 2004). The presence of high-coercivity components (hematite) in some GH samples could lead to increasing Hcr, and hence increasing the values of Hcr/Hc (Roberts et al., 1995, Deng et al, 2004). Therefore, the hysteresis parameters will shift to the coarser end of the PSD box to some extent (Fig. 3A).

Representative samples were also plotted on fig 3B (Day et al., 1977 & Dunlop et al, 2002). These data are not plotted along Dunlop mixing black curves of magnetite, which indicate the presence of both magnetite and hematite as the remanence carriers (Fig. 3B).

The remanence ratios (Mrs/Ms) versus hysteresis rations (Hc) for representative TV, KA and GH samples were also plotted on squareness-coercivity (SC) plot. (Tauxe et al., 2002, Wang & Van der Voo, 2004). Such a plot shows that our data tend to follow the trend of magnetite line. Thus, magnetite is the main dominance remanence carrier in most of the studied samples. However, some of the data are not aligned, suggesting higher coercivity values and the presence of harder materials (hematite) for GH samples (Fig. 3C). Therefore, TV and KA sediments mainly contain soft minerals (magnetite) with low coercivity values, while GH sediments mostly contain hard minerals (hematite) with higher coercivity values.

Moreover, hysteresis results for TV and KA samples are characterized by low ratios of saturation remanence (0.06 < Mrs/Ms < 0.2) as well as low coercivity, so that Hc values range from 6 to 18 mT (Hc < 18 mT) and from 5 to 11 mT (Hc < 11 mT) for TV and KA samples, respectively, while GH samples show higher ratios of saturation remanence ($0.1 < Mrs/Ms < 0.3$) and high coerivity which range from 10 to 55 mT (Fig. 4, I haven’t prepared yet).

4. Discussion and conclusions

According to this magnetic mineralogy results, the sediments along southern side of the basin should have only received sediments from a main source area. Conversely, sediments along the central part of the basin show a higher complexity with respect to the magnetic mineralogy characterises, indicating that they must have been sourced from multiple lithotypes. The result of the sediment provenance study reported in chapter 3 corroborate these results. Sandstone petrography data from the KA section, document a rather constant composition dominated by volcanic lithics and feldspars (feldspatho-lithic arenite; QFL plot; Figs 12B), as expected for undissected arc regions (QtFL-c ternary diagram; Fig. 12A). Instead, the central part of the basin received a greater amount of sediments from the Alborz Mountains as documented by the higher proportion of metamorphic grains.

The paleoenvironmental evolution of the basin will be addressed in second stage when these data will be compared with stable isotope (Carbon and Oxygen) results from carbonate paleosols and lacustrine marls.

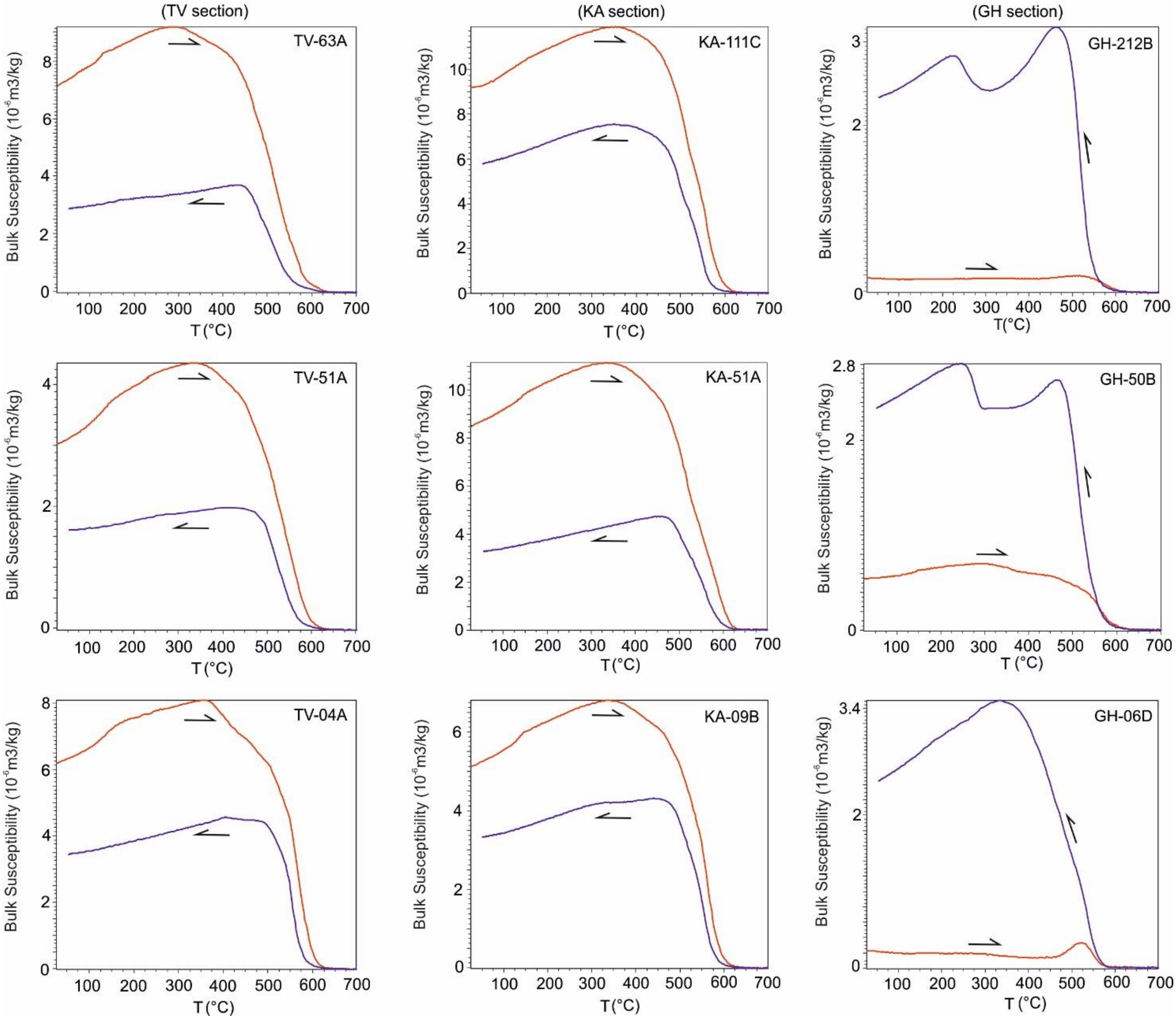

Figure 1. Representative Thermomagnetic curves (Magnetic susceptibility (K) versus temperature (T) for nine representative TV, KA and GH samples. Heating and cooling curves are shown by red and blue colours, respectively.

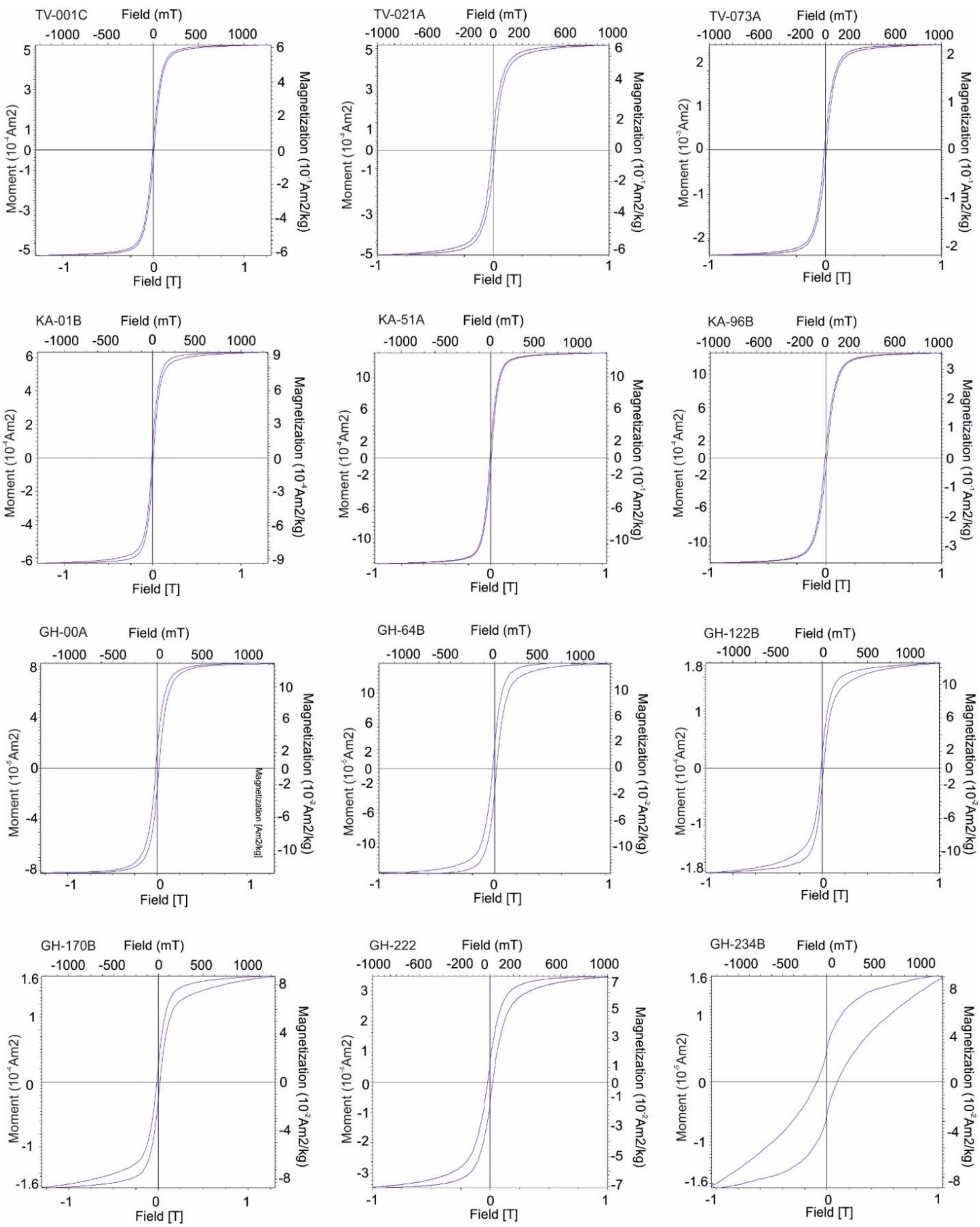

Figure 2. Examples of hysteresis loops to a peak field of 1.5 T for representative TV, KA and GH samples. Most of the studied samples present a narrow loop (typical of pseudosingle domain hysteresis loop) indicating the occurrence of magnetite and probably pigmentary hematite?. The hysteresis curves for TV and KA samples have alow coercivity force (Hc) and coercivity of remanence values (Hcr) values, suggesting the dominance of magnetically soft minerals. GH samples have higher Hc and Hcr values in compare to TV and KA samples. These samples have a mixture of both low and high coercivity minerals, suggesting the presence of magnetite and hematite, respectively. Note tate few GH samples present a 'wasp-waisted' loop, the typical shape for hematite (e.g. the last fig below in the right corner). All data corrected for slope of paramagnetism.

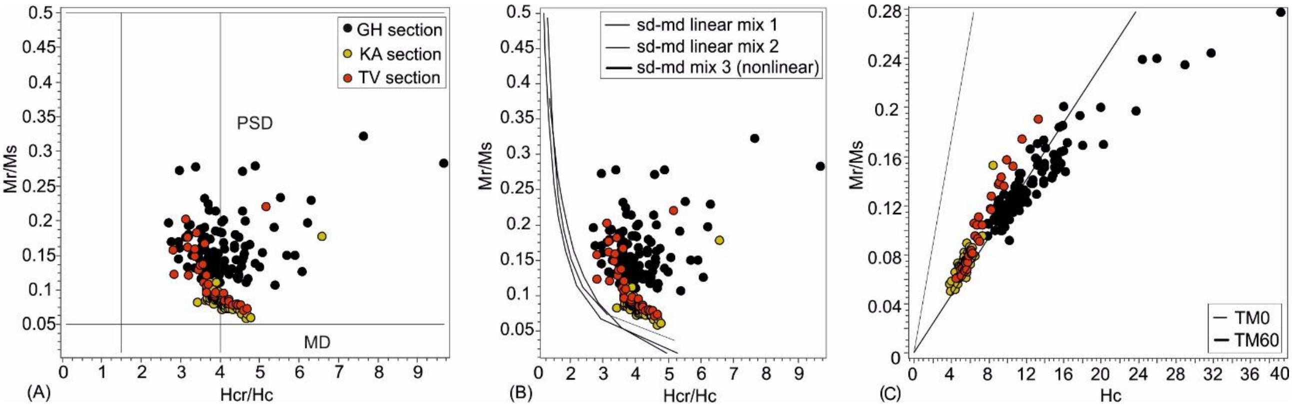

Figure 3. (A and B) A Day plot of the hysteresis parameter ratios (Day et al, 1977) showing the hysteresis magnetization (Mrs/Ms) versus coercivity ratios (Hcr/Hc) for the three stratigraphic sections in the Tarom basin. The line represents a theoretical mixing curve for MD particles at variable percentages (black squares) with uniaxial SD magnetite (Dunlop, 2002). The PSD label denotes the region for pseudosingle particles (Day et al., 1977). Red, yellow and black circles represent samples from Sections TV, KA and GH, respectively. (B) Our data are not plotted along the Dunlop mixing curves of magnetite, indicating the presence of both magnetite and hematite as the main remanence carriers (Dunlop et al, 2002). (C) Squareness-coercivity plot? All data are plotted along the second black line, indicating that the data tend to follow the trend of magnetite line. Thus, magnetite is the main dominance remanence carrier in most of the studied samples. However, some of the data are not in consistent with line, suggesting the higher coersivity values and the presence of harder materials (hematite) for GH samples (black circles).

Chapter 5: Conclusions

The combination of all results presented in chapter 2 and 3 allow tracking the evolutionary history of the intermontane Tarom Basin in the framework of orogenic and plateau building processes associated with the ongoing Arabia-Eurasia collision. Geochronology data and field observations document an initial phase of low-magnitude compressional deformation along the NW margin of the Iranian Plateau and possibly the western Alborz mountains starting from ~38-36 Ma simultaneously with the termination of the regional Eocene arc volcanism. Subsequently, the topographic growth of the basin margins (Tarom range to S and Alborz Mountains to N) led to formation of an internally drained intermontane basin (Tarom Basin) from ~16 Ma. This coincides with the Early-Middle Miocene acceleration of contractional collisional deformation observed across the entire collision zone. The tectonic loading caused by the adjacent mountain ranges was most likely responsible for lithospheric flexure that generated accommodation space for the accumulation of the red beds, which are stratigraphically equivalent to the Upper Red Formation (URF). Thus, extension triggered by the synsedimentary normal faults observed along the southern margin of the basin cannot be responsible for creating accommodation space. This is in agreement with new AMS data documenting a lithogenetic magnetic fabric unaffected by extensional deformation and also with the absence of similar faults in coeval strata from adjacent basins. Overall, extensional deformation must have been very minor and localized, possibly associated with the gravitational instability of the growing Tarom range as suggested by the presence of landslide deposits embedded in the red beds of the URF. Furthermore, the integrated rock magnetic and sediment provenance analysis indicates that sediments along the southern margin of the basin were only sourced from the Eocene volcanics of Karaj Formation, while the sediments that filled the central sectors of the basin received a large fraction of sediments from the northern basin margins (Alborz Mountains), where a greater variability of rocks are exposed (i.e., metamorphic, sedimentary and magmatic rocks). Sedimentation in the basin terminated sometime after ~ 7.6 Ma and was followed by intrabasinal uplift and erosion induced by the regional NE-SW oriented compressional direction. This is consistent with the development of a magnetic fabric of tectonic origin that formed during a weak to moderate episode of layer parallel shortening recorded by data. After ~7.6 Ma, the basin experienced also a major phase of incision and excavation followed by younger phases (at least four, form the Pliocene?) of aggradation and incision during alternating episodes of reduced and renewed fluvial connectivity with the Caspian Sea. Finally, my results, field observations and available data, indicate that the northern margin of the basin experienced more exhumation and accommodated a larger fraction of plate convergence than the southern one, most likely through the reactivation of inherited structures. This suggest that uplift of the Tarom range which composes the southern plateau margin must have been triggered by deep seated, mantle drive, processes rather than shortening and thickening processes.

REFERENCES

A1. References of chapter 2:

ABIMBOLA., D.A. (2016) A Re-evaluation of the Depositional Environments and Sedimentary Facies of Middle Miocene Paralic Deposits (Agbada Formation), Ewan and Oloye Fields, Northwestern Niger Delta, Journal of Marine Science: Research & Development.

AGARD, P., OMRANI, J., JOLIVET, L., WHITECHURCH, H., VRIELYNCK, B., SPAKMAN, W., MONIE, P., MEYER, B. & Wortel, R. (2011) Zagros orogeny: A subduction-dominated process, Geol. Mag, 148 (5–6), 689–691.

ALLMENDINGER, R.W., JORDAN, T.E., KAY, S.M. & ISACKS, B.L. (1997) the evolution of the Altiplano-Puna Plateau of the central Andes: Annual Review of Earth and Planetary Sciences, 25, 139–174.

ALONSO, B., E Field, M., V GARDNER, J. & MALDOANDO, A. (1990) Sedimentary evolution of the Pliocene and Pleistocene Ebro margin, northeastern Spain. Marine Geology, 95, 313-331.

BALLATO, P., BRUNE, S. & STRECKER, M.R. (2019) Sedimentary loading–unloading cycles and faulting in intermontane basins: Insights from numerical modeling and field observations in the NW Argentine Andes. Earth and Planetary Science Letters, 506, 388-396.

BALLATO, P., CIFELLI, F., HEIDARZADEH, G.H., GHASSEMI, M.R., WICERT, A.D., HASSANZADEH, J., DUPONT–NIVET, G., BALLING, P., SUDO, M., ZEILIGER, G., SCHMIT, A.K., MATTEI, M. & STRECKER, M.R. (2017) Tectono-sedimentary evolution of the northern Iranian Plateau: insights from middle-late Miocene foreland-basin deposits, Basin Research, 29, 1–30.

BALLATO, P., LANDGRAF, A., FOX, M., STOCKLI, D., SCHILDGEN, T.F., GHASSEMI, M.R., KIRBY, E. & STRECKER, M.R. (2015) the growth of a mountain belt forced by base-level fall: tectonics and surface processes during the evolution of the Alborz Mountains, N Iran. Earth Planet. Sci. Lett., 425, 204–218.

BALLATO, P., NOWACZYK, N.R., LANDGRAF, A., STRECKER, M.R., FRIEDRICH, A. & TABATABAEI, S.H. (2008) Tectonic control on sedimentary facies pattern and sediment accumulation rates in the Miocene foreland basin of the southern Alborz mountains, northern Iran. Tectonics, 27, TC6001.

BALLATO, P., STOCKLI, D.F., GHASSEMI, M.R., LANDGRAF, A., STRECKER, M.R., HASSANZADEH, J., FRIEDRICH, A. & TABATABEI, S.H. (2013) Accommodation of

transpressional strain in the Arabia-Eurasia collision zone: new constraints from (UTh)/He thermochronology in the Alborz Mountains, N Iran. Tectonics, 32, 1–18.

BALLATO, P., UBA, C.E., LANDGRAF, A., STRECKER, M.R., SUDO, M., STOCKLI, D.F., FRIEDRICH, A. & TABATABAEI, S. H. (2011) Arabia-Eurasia continental collision: Insights from late Tertiary foreland-basin evolution in the Alborz Mountains, northern Iran. Geological Society of America Bulletin, 123, 106–131.

BERBERIAN, M. & WALKER, R. (2010) The Rudbār Mw 7.3 earthquake of 1990 June 20; seismotectonics, coseismic and geomorphic displacements, and historic earthquakes of the western ‘High-Alborz’, Iran. Geophysical Journal International, 182, 1577–1602.

BLAIR., T.C., (1999) Sedimentology of the debris-flow–dominated Warm Spring Canyon alluvial fan, Death Valley, California. Sedimentology, 46, 941–965.

BOOTHROYD, J.C. & ASHLEY, G.M. (1975) Processes, bar morphology, and sedimentary structures on braided outwash fans, Northeastern Gulf of Alaska. The Society of Economic Paleontologists and Mineralogist (SEPM); Glaciofluvial and Glaciolacustrine Sedimentation (SP23).

BORRADAILE, G.J. & HENRY, B. (1997) Tectonic applications of magnetic susceptibility and its anisotropy. Earth Sci Rev, 42, 49–93.

BORRADAILE., G. J. (1988) Magnetic susceptibility, petrofabrics and strain. Tectonophysics, 156, 1-20.

BORRADAILE., G. J. (2001) Magnetic fabrics and petrofabrics: Their orientation distribution and anisotropies. J. Struct. Geol, 23, 1581–1596.

BRUNET, M., KOROTAEV, M.V., ERSHOV, A.V. & NIKISHIN, A.M. (2003) The South Caspian Basin: a review of its evolution from subsidence modelling. Sedimentary Geology, 156, 119-148.

CARROLL, A.R., GRAHAM, S.A. & Smith, M.E. (2010) Tectonic and Stratigraph. Evolution of Nonmarine Basins of China. Basin Research, 22, 17 - 32.

CASTELLANOS., D.G. (2007) The role of climate during high plateau formation Insights from numerical experiments. Earth and Planetary Science Letters, 257, 372–390.

CHARREAUH, J., CHEN, Y., GILDER, S., DOMINGUEZ, S., AVOUAC, J.PH. SEN, S., SUN, D., LI, Y. & WANG, W.M. (2005) Magnetostratigraphy and rock magnetism of the Neogene Kuitun He section (northwest China): Implications for Late Cenozoic uplift of the Tianshan mountains. Earth and Planetary Science Letters, 230, 177–192.

DAVIS, D., SUPPE, J. & DAHLEN, F.A. (1983) Mechanics of fold-and-thrust belts and accretionary wedges. J. Geophys. Res, 88, 1153–72.

DAVOUDZADEH, M., LAMMERER, B. & WEBER-DIEFENBACH, K. (1997) Paleogeography, Stratigraphy, and Tectonics of the Tertiary of Iran. Neues Jahrbuch für Geologie und Paläontologie – Abhandlungen, 205, 33-67.

DEWEY, J.F. & BURKE, K. (1974) Hot spots and continental break-up: implications for collisional orogeny. Geology, 2, 57–60.

DEWEY, J.F. (1988) Extensional collapse of orogens. Tectonics, 7, 1123–1139.

DICKINSON., W.R. (1985) Interpreting provenance relations from detrital modes of sandstones. In: Zuffa, G.G. (Ed.), Provenance of arenites. Reidel, Dordrecht, NATO ASI Series, 148, 333–361.

DJAMOUR, Y.,VERNANT, P.H., BAYER, R., NANKALI, H.R., RITZ, J.F., HINDERER, J., HATAM, Y., LUCK, B. & Moigne, N.L. (2010) GPS and gravity constraints on continental deformation in the Alborz mountain range, Iran. Geophysical Journal International, 183, 1287-1301.

DUPONT-NIVET, G. & KRIJGSMAN, W. (2012) Magnetostratigraphic methods and applications, in Busby, C., & Azor, A. (eds.), Recent Advances in Tectonics of Sedimentary Basins, Wiley-Blackwell, p 80-94.

EJI UBA, C., HEUBECK, C. & HULKA, C. (2005) Facies analysis and basin architecture of the Neogene Subandean synorogenic wedge, southern Bolivia. Sedimentary Geology, 180, 91–123.

ENGDAHL, E., JACKSON, J., MYERS, S., BERGMAN, E. & PRIESTLEY, K. (2006) Relocation and assessment of seismicity in the Iran region. Geophys. J. Int., 167, 761–788.

ENGLAND, P.H. & MVKENZIE, D. (1982) A thin viscous sheet model for continental deformation. Geophysical Journal of the Royal Astronomical Society, l70, 295–32.

FORTE, A.M. & COWGILL, E. (2013) Late Cenozoic base-level variations of the Caspian Sea: a review of its history and proposed driving mechanisms. Palaeogeogr. Palaeo-climatol. Palaeoecol, 386, 392–407.

FRANCOIS, T., BUROV, E., AGARD, P. & MEYER, B. (2014) Buildup of a dynamically supported orogenic plateau: Numerical modeling of the Zagros/Central Iran case study; Geochem. Geophys. Geosyst, 15, 2632–2654.

GARZANTI., E.D. (2019) Petrographic classifiation of sand and sandstone. Earth-Science Reviews, 192, 545–563.

GHIBAUDO., G.U. (1992) Subaqueous sediment gravity flow deposits: practical criteria for their field description and classification. Sedimentology (IAS), 39, 423-454.

GRADSTEIN, F.M., OGG, J.G., SCHMITZ, M. & OGG, G. (2012) The Geologic Time Scale 2012. Elsevier, Cambridge University Press, Cambridge.

GUEST, B., AXEN, G.J., LAM, P.S., & HASSANZADEH, J. (2006a) Late Cenozoic shortening in the west central Alborz Mountains, northern Iran, by combined conjugate strike-slip and thin-skinned deformation. Geosphere, 2, 35–52.

GUEST, B., HORTON, B.K., AXEN, G.J., HASSANZADEH, J. & MCINTOSH, W.C. (2007) Middle to late Cenozoic basin evolution in the western Alborz Mountains: Implications for the onset of collisional deformation in northern Iran. Tectonics, 26, TC6011.

GUEST, B., STOCKLI, D. F., GROVE, M., AXEN, G. J., LAM, P. S. & HASSANZADEH, J. (2006b) Thermal histories from the central Alborz Mountains, northern Iran: Implications for the spatial and temporal distribution of deformation in northern Iran. Geological Society of America Bulletin, 118, 1507-1521.

HASSANZADEH, J., STOCKLI, D. F., HORTON, B. K., AXEN, G. J., STOCKLI, L. D. & GROVE, M. (2008) U-Pb zircon geochronology of late Neoproterozoic- Early Cambrian granitoids in Iran: Implications for paleogeography, magmatism, and exhumation history of Iranian. 778 basement. Tectonophysics, 451, 71–96.

HATZFELD, D. & MOLNAR, P. (2010) Comparisons of the kinematics and deep structures of the Zagros and Himalaya and of the Iranian and Tibetan plateaus and geodynamic implications, Rev. Geophys, 48, 2.

HEIDARZADEH, G.H., BALLATO, P., HASSANZADEH, J., GHASSEMI, M.R. & STRECKER, M.R. (2017) Lake overspill and onset of fluvial incision in the Iranian Plateau: insights from the Mianeh Basin; Planetary Science Letters, 469, 135-147.

HEIN., F.J., (1982) Depositional mechanisms of deep-sea coarse clastic sediments, Cap Enrage Formation, Quebec. Canadian Journal Earth Science, 19, 267–287.

HERMANNS, R.L. & STRECKER, M.R. (1999) Structural and lithological controls on large Quaternary rock avalanches (sturzstroms) in arid northwestern Argentina. Geological Society of America Bulletin, 111, 934-948.

HILLEY, G.E, STRECKERt, M.R. & RAMOS, V.A. (2004) Growth and erosion of fold-and-thrust belts with an application to the Aconcagua fold-and-thrust belt, Argentina. J. Geophys. Res, 109, B1.

HILLEY, G.E. & STRECKER, M.R. (2004) Steady state erosion of critical Coulomb wedges with applications to Taiwan and the Himalaya. J. Geophys. Res, 109, B1.

HORTON, B.K., HASSANZADEH, J., STOCKLI, D.F., AXEN, G.J., GILLIS, R.J., GUEST, B., AMINI, A., FAKHARI, M.D., Zamanzadeh, S.M. & Grove, M. (2008) Detrital zircon provenance of Neoproterozoic to Cenozoic deposits in Iran: Implications for chronostratigraphy and collisional tectonics: Tectonophysics, 451, 97–122.

HROUDA., F. (1982) Magnetic anisotropy of rocks and its application in geology and geophysics. Surveys in Geophysics. 5, 37–82.

INGERSOLL, R.V., BULLAED, T.F., FORD, R.L., GRIMM, J.P., PICKLE, J.D. & SARES, S.W. (1984) the effect of grain size on detrital modes: a test of the Gazzi–Dickinson point-counting method. Journal of Sedimentary Petrology, 54, 103 –116.

ISACKS., B.L. (1988) Uplift of the central Andean Plateau and bending of the Bolivian Orocline, J. Geophys. Res, 93, 3211–3231.

JIMENEZ-MUNT, I., FERNANDEZ, M., SAURA, E., VERGES, J. & GARCIA-CASTELLANOS, D. (2012) 3-D lithospheric structure and regional/residual Bouger anomalies in the Arabia-Eurasia collision (Iran). Geophys. J. Int., 190, 1311–1324.

KODAMA., K.P. (2012) Paleomagnetism of Sedimentary Rocks: Process and Interpretation. Science, p 184.

KOSHNAW, R.I. & STOCKLI, D.F. (2018) Timing of the Arabia-Eurasia continental collision-Evidence from detrital zircon U-Pb geochronology of the Red Bed Series strata of the northwest Zagros hinterland, Kurdistan region of Iraq. Geology, 47, 47-50.

KRAUS., M.J. (1999) Paleosols in clastic sedimentary rocks: their geologic applications. Earth Science Reviews, 47, 41-70.

LAMB, S., HOKE, L., KENNAN, L. & DEWEY, J. (1997) Cenozoic Evolution of the Central Andes in Bolivia and Northern Chile, ed. JP Burg, M Ford, 121, 237–64.

LANGEREIS, C.G, KRIJGSMAN, W., MUTTONI, G. & MENNING, M. (2010) Magnetostratigraphy; concepts, definitions, and applications. Newsletter on Stratigraphy, 43/3, 207–233.

LARRASOANA, J.C., Pueyo, E.L. & PARES, J.M. (2004) An integrated AMS, structural, palaeo- and rock-magnetic study of Eocene marine marls from the Jaca-Pamplona basin (Pyrenees, N Spain); new insights into the timing of magnetic fabric acquisition in weakly deformed mudrocks. Geological Society, London, Special Publications, 238(1), 127.

LOWENSTEIN, T.K., & HARDIE, L.A. (1985) Criteria for the recognition of salt-pan evaporites. Sedimentology, 32, 627–644.

MADANIPOUR, S., EHLERS, T., YASSAGHI, A., REZAEIAN, M., ENKELMANN, E. & BAHROUDI, A. (2013) Synchronous deformation on orogenic plateau margins: insights from the Arabia-Eurasia collision. Tectonophysics, 608, 440–451.

MADANIPOUR, S., EHLERS, T.A., YASSAGHI, A. & ENKELMANN, E. (2017) Accelerated middle Miocene exhumation of the Talesh Mountains constrained by U-Th/He thermochronometry: Evidence for the Arabia-Eurasia collision in the NW Iranian Plateau. Tectonics, 36, 1538-1561.

MADANIPOUR, S., YASSAGHI, A., TODD EHLERS, T.A. & ENKELMAN, E. (2018) Tectonostratigraphy, structural, geometry and kinematics of the NW Iranian Plateau margin: Insight from the Talesh mountains, Iran. American Journal of Science, 318, 208-245.

MAIZELS., J. (1989) Sedimentology, paleoflow dynamics and flood history of jokulhlaup deposits; paleohydrology of Holocene sediment sequences in southern Iceland sandur deposits. Journal of Sedimentary Research, 59, 204-223.

MCFADDEN, P.L. & MCELHINNY, M.W. (1990) Classification of the reversal test in palaeomagnetism. Geophys. J. Int., 103, 725–729.

MEYER, B., TAPPONNIER, P., BOURJOT, L., ME´TIVER, F., GAUDEMER, Y., PELTZER, G., GUO, S. & Chen, Z. (1998) Crustal thickening in Gansu-Qinghai, lithospheric mantle subduction, and oblique, strike-slip controlled growth of the Tibet Plateau. Geophys. J. Int., 135, 1–47.

MIALL., A.D. (1978) Lithofacies types and vertical profie models in braided river deposits. Fluvial Sedimentology: Canadian Society Petrology Geology Memoir, 5, 597–604.

MIALL., A.D. (1985) Architectural-Element Analysis: A New Method of Facies Analysis Applied to Fluvial Deposits. Earth-Science Reviews, 22, 261-308.

MIALL., A.D. (1996) The Geology of Fluvial Deposits. SpringerVerlag, Berlin, XVI, 582 pp.

MIALL., A.D. (1997) A review of the braided river depositional environment. Earth Science Review, 13, 1–62.

MOLNAR, P., ENGLAND, PH. & MARTIOD, J. (1993) Mantle dynamics, uplift of the Tibetan Plateau, and the Indian Monsoon. Reviews of Geophysics, 31, 357-396.

MORLEY, C., KONGWUNG, B., JULAPOUR, A.A., ABDOLGHAFOURIAN, A., HAJIAN, M., WAPLES, D., WARREN, J., OTTERDOOM, H., SRISURIYON, K. & KAZEMI, H. (2009) Structural development of the major Late Cenozoic basin and transpressional belt in Central Iran: the Central Basin in the Qom-Saveh area. Geosphere, 5, 325–362.

MOUTHEREAU, F., LACOMBE, O. & VERGES, J. (2012) Building the Zagros collisional orogen: timing, strain distribution and the dynamics of Arabia/Eurasia plate convergence. Tectonophysics, 532-535, 27-60.

MOUTHEREAU, F., LACOMBE, O. & VERGES, J. (2012) Building the Zagros collisional orogen: timing, strain distribution and the dynamics of Arabia/Eurasia plate convergence. Tectonophysics, 532–535, 27–60.

NABATIAN, GH. GHADERI, M., NEUBAUER, F., HONARMAND, M., LIU, X., DONG, Y., JIANG, S.H.Y., QUADT, A.V. & BERNROIDER, M. (2014) Petrogenesis of Tarom high-potassic granitoids in the Alborz-Azarbaijan belt, Iran: Geochemical, U-Pb zircon and Sr–Nd–Pb isotopic constraints. Lithos, 184–187, 324-345.

OMRANI, H., MOAZZEN, M., OBERHANSLI, R., TSUJIMORI, T., BOUSQUET, R. & MOAYYED, M. (2013) Metamorphic history of glaucophane-paragonite-zoisite eclogites from the Shanderman area, northern Iran. Journal of Metamorphic Geology, 31, 791-812.

PARES., J.M. (2004) How deformed are weakly deformed mudrocks? Insights from magnetic magnetic anisotropy. In: Martin-Hernandez, F., Lüneburg, C., Aubourg, C., Jackson, M. (Eds.), Magnetic Fabrics: Methods and Applications. Geological Society, London, Special Publication, 238, 191–203.

PINGEL, H., ALONSO, R.N., ALTENBERGER, U., COTTLE, J. & STRECKER, M.R. (2019) Miocene to Quaternary basin evolution at the southeastern Andean Plateau (Puna) margin ca. 24°S lat, Northwestern Argentina. Basin Research, 32, 808-826.

PINGEL, H., SCHILDGEN, T. & STRECKER, M.R. (2019) Hella Wittmann, Pliocene–Pleistocene orographic control on denudation in northwest Argentina. Geology, 47, 359-362.

PIROUZ, M., AVOUAC, J-P., HASSANZADEH, J., KIRSCHVINK, J.L. & BAHROUDI, A. (2017) Early Neogene foreland of the Zagros, implications for the initial closure of the Neo-Tethys and kinematics of crustal shortening. Earth and Planetary Science Letters, 477, 168–182.

PUY-AQUIZA, M.J., MIRANDA-AVILES, R., GARCIA-BARRAGAN, J.C., LOZA-AGUIRRE, I., Li, Y. & ANA ZANOR, G. (2017) Facies analysis, stratigraphic architecture and depositional environments of the Guanajuato conglomerate in the Sierra de Guanajuato, Mexico. Boletín de la Sociedad Geológica Mexicana, 69, 385-408.

R. MERRILL, R., MC.FADDEN, P. & MCELHINNY, M. (1996) the Magnetic Field of the Earth: Paleomagnetism, the Core, and the Deep Mantle. International geophysics series ISSN 0074-6142; Academic Press, San Diego, p 531.

REINERS, P.W. & BRANDON, M.T. (2006) Using thermochronology to understand orogenic erosion. Annu. Rev. Earth Planet. Sci, 34, 419–66.

REUTER, M., PILLER, W. E., HARZHAUSER, M., MANDIC, O., BERNING, B., ROGL, F. (2009) The Oligo-/Miocene Qom Formation (Iran): Evidence for an early Burdigalian restriction of the Tethyan Seaway and closure of its Iranian gateways. International Journal of Earth Sciences, 98, 627–650.

REZAEIAN, M., CARTER, A., HOVIUS, N. & ALLEN, M.B. (2012) Cenozoic exhumation history of the Alborz Mountains, Iran: New cconstraints from low-temperature chronometry. Tectonics, 31, TC2004.

RIDGWAY, K.D., & DECELLES, P.G. (1993) Stream-dominated alluvial fan and lacustrine depositional systems in Cenozoic strike-slip basins, Denali fault system, Yukon Territory, Canada. Sedimentology, l40, 645-666.

RIEBEN., H. (1955), The geology of the Tehran plain. American Journal of Science, 253, 617–639.

Robert., A.M.M., LETOUZEY, J., KAVOOSI, M.A., SHERKATI, S.H. & MULLER, C. (2014) Structural evolution of the Kopeh Dagh fold-and-thrust belt (NE Iran) and interactions with the South Caspian Sea Basin and Amu Darya Basin. Marine and Petroleum Geology, Elsevier, 57, 68-87.

ROBION, P., GRELAUD, S. & FRIZON DE LAMOTTE, D. (2007) Pre-folding magnetic fabrics in fold and-thrust belts: Why the apparent internal deformation of the sedimentary rocks from the Minervois basin (NE — Pyrenees, France) is so high compared to the Potwar basin (SW — Himalaya, Pakistan)? Sediment. Geol, 196, 181–200.

ROYDEN., L. (1996) Coupling and decoupling of crust and mantle in convergent orogens: Implications for strain partitioning in the crust, J. Geophys. Res, 101, 17, 679–17, 705.

ROYDEN., L.H., BURCHFIEL, B. C., KING, R.W., WANG, E., CHEN, Z., SHEN, F. & LIU, Y. (1997) Surface deformation and lower crustal flow in Eastern Tibet. Science, 276 (5313), 788–790.

SAINT-BEZAR, B., HEBERT, R.L., AUBOURG, C., ROBION, P., SWENEN, R. FRIZON DE & LAMOTTE, D. (2002) Magnetic fabric and petrographic investigations of hematite-bearing sandstones within ramp-related folds: examples from the South Atlas Front (Morocco). J. Struct. Geol. 24, 1507–1520.

SCHILDGEN, T., ROBINSON, R.A.J., SAVIi, S., PHILLIPS, W.M., SPERNCER, J.Q.G., BOOKHANGEN, B., SCHERLER, D., TOFELDE, S., ALONSO, R.N., KUNIK, P.W., BINNIE, S.A. & STRECKER, M.R. (2016) Landscape response to late Pleistocene climate change in NW Argentina: sediment flux modulated by basin geometry and connectivity. J. Geo-phys. Res, 121, 392–414.

SIKS, B.C. & HORTON, B.K. (2011) Growth and fragmentation of the Andean foreland basin during eastward advance of fold-thrust deformation, Puna plateau and Eastern Cordillera, northern Argentina. Tectonic, 30.

SIKS, B.C. & HORTON, B.K. (2011) Growth and fragmentation of the Andean foreland basin during eastward advance of fold-thrust deformation, Puna plateau and Eastern Cordillera, northern Argentina. Tectonics, 30, TC6017.

SOBEL, E.R. & STRECKER, M.R. (2003) Uplift, exhumation and precipitation: Tectonic and climatic control of late Cenozoic landscape evolution in the northern Sierras Pampeanas, Argentina. Basin Research, 15, 431–451.

SOBEL, E.R., HILLEY, G.E. & STRECKER, M.R. (2003) Formation of internally drained contractional basins by aridity-limited bedrock incision. J. Geophys. Res. Solid Earth, 108, JB001883.

SOTO, R., LARRASOANA, J.C., ARLEGUI, L.E., BEAMUD, E., OLIVAURCIA, B. & SIMON, J.L. (2009) Reliability of magnetic fabric of weakly deformed mudrocks as a palaeostress indicator in compressive settings. J. Struct. Geol., 31, 512–522.

STANISTREET, I.G. & MCCARTHY, T.S. (1993) The Okavango Fan and the classification of subaerial fan systems. Sedimentary Geology, 85, 115–133.

STOCKLIN, J. & EFTEKHARNEZHAD, J. (1969) Geological map of Zanjan quadrangle. Geological Survey of Iran, Tehran, scale 1:250,000.

STRECKER, M.R., ALONSO, R., BOOKHAGEN, B., CARRAPA, B., COUTAND, I., HAIN, M.P., HILLEY, G.E., MORTIMER, E., SCHOENBOHM, L. & SOBEL, E.R. (2009) Does the topographic distribution of the central Andean Puna Plateau result from climatic or geodynamic processes. Geology, 37, 643–646.

STRECKER, M.R., ALONSO, R.N., BOOKHAGEN, B., CARRAPA, B., HILLEY, G.E., SOBEL, E.R., & TRAUTH, M.H. (2007) Tectonics and Climate of the Southern Central Andes. Annu. Rev. Earth Planet, 35, 747-787.

STREIT, R.L., BURBANK, D.W., STRECKER, M.R., ALONSO, R.N., COTTLE, J.M. & KULANDER-CLARK, A.R.C. (2015) Controls on intermontane basin filling, isolation and incision on the margin of the Puna plateau, NW Argentina (~23°S). Basin Research, 29, 131–155.

TARLING, D. H. & HROUDA, F. (1993) the Magnetic Anisotropy of Rocks. London: Chapman & Hall, 217 p.

THA, H.V, WYSOCKA, A., PHA, P.D., CUONG, N.Q. & ZIOLKOWSKI, P. (2015) Lithofacies and depositional environments of the Paleogene/Neogene sediments in the Hoanh Bo Basin (Quang Ninh province, NE Vietnam). Geology, Geophysics & Environment, 41, 353–369.

THIEDE, R., BOOKHAGEN, B., ARROWSMITH, J.R, SOBEL, E. & STRECKER, M.R. (2004) Climatic control on rapid exhumation along the southern Himalayan front. Earth Planet. Sci. Lett, 222, 791–806.

TODD., S.P. (1989) Stream-driven, high-density gravelly traction carpets: possible deposits in the Trabeg Conglomerate Formation, SW Ireland and some theoretical considerations of their origin. Sedimentology (IAS), 36, 513-735.

TOFELDE, S., SCHILDGEN, T.F., SAVI, S., PINGEL, H., WICKERT, A.D., BOOKHANGEN, B., WITTMANN, H., ALONSO, R.N., COTTLE, J. & STRECKER, M.R. (2017) 100kyrfluvial cut-and-fill terrace cycles since the Middle Pleistocene in the southern Central Andes, NW Argentina. Earth Planet. Sci. Lett, 473, 141–153.

VAN BAAK, C.G.C., VASILIEV, I., STOICA, M., KUIPER, K.F., FORTE, A.M., ALIYEVA, E. & KRIJGSMAN, W. (2013) A magnetostratigraphic time frame for Plio-Pleistocene transgressions in the South Caspian Basin, Azerbaijan. Glob. Planet. Chang, 103, 119 –134.

VERDEL, C., WERNICKE, B.P., HASSANZADEH, J. & GUEST, B. (2011) A Paleogene extensional arc flare-up in Iran. Tectonics, 30, TC3008.

VERNANT., P. (2004), Present-day crustal deformation and plate kinematics in the Middle East constrained by GPS measurements in Iran and north ern Oman, Geophys. J. Int., 157, 381–398.

VINCENT, S.J., MORTON, A.C., CARTER, A., GIBBS, S. & BARABADZE, T.G. (2007) Oligocene uplift of the western Greater Caucasus: An effect of initial Arabia– Eurasia collision. Terra Nova, 19, 160–166.

WHIPPLE, K.X. & MEADE, B.J. (2004) Controls on the strength of coupling among climate, erosion, and deformation in two-sided, frictional orogenic wedges at steadystate. J. Geophys. Res, 109, F1.

WILLETT., S.D. (1999) Orogeny and orography: The effects of erosion on the structure of mountain belts. J. Geophys. Res, 104, 28957–28981.

WILMSEN, M., FURSICHFRANZ, F.T., FURSICH, T., SEYED-EMAMI, K., MAJIDIFARD, M.R. & TAHERI, J. (2009) The Cimmerian Orogeny in northern Iran: Tectono-stratigraphic evidence from the foreland. Terra nova, 21, 211-218.

YASSAGHI, A. & MADANIPOUR, S. (2008) Influence of a transverse basement fault on along strike variations in the geometry of an inverted normal fault: Case study of the Mosha Fault, Central Alborz Range, Iran. J. Struct. Geol., 30, 1507–1519.

ZANCJI, A., ZANCHETTA, S., BERRA, F., MATTEI, M., GARZANTI. E., MOLYNEUX, S., NAWAB, A. & SABOURI, J. (2009) the Eo-Cimmerian (Late? Triassic) orogeny in North Iran. Geological Society, London, Special Publication, 312, 31-55.

A2. References of chapter 3:

Alimohammadian, H., Hamidi, Z., Aslani, A., Shahidi, A., Cifelli, F., and Mattei, M.: A tectonic origin of magnetic fabric in the Shemshak Group from Alborz Mts. (northern Iran), Journal of Asian Earth Science, 73, 419-428, http://doi.org/10.1016/j.jseaes.2013.05.014, 2013.

Allen, M., Jackson, J., and Walker, R.: Late Cenozoic re-organization of the Arabia-Eurasia collision and the comparison of short-term and long-term deformation rates, Tectonics, 23, TC2008, http://doi.org/10.1029/2003TC001530, 2004.

Averbuch, O., Frizon de Lamotte, D. and Kissel, C.: Magnetic fabric as a structural indicator of the deformation path within a fold–thrust structure: a test case from the Corbieres (NE Pyrenees, France), Journal of Structural Geology, 14, 461–474, https://doi.org/10.1016/0191-8141 (92)90106-7, 1992.

Ballato, P., Cifelli, F., Heidarzadeh, G.H., Ghassemi , M.R., Wickert, A.D. Hassanzadeh, J., Dupont-Nivet, G., Balling, P.H., Sudo, M., Gerold Zeilinger, G., Schmitt, A.K., Mattei, M., and Strecker, M.R.: Tectono-sedimentary evolution of the northern Iranian Plateau: Insights from middle-late Miocene foreland-basin deposits, Basin Research, 29, 417-446, http://doi.org/10.1111/bre.12180, 2016.

Ballato, P., Nowaczyk, N.R., Landgraf, A., Strecker, M.R., Friedrich, A., and Tabatabaei, S.H.: Tectonic control on sedimentary facies pattern and sediment accumulation rates in the Miocene foreland basin of the southern Alborz Mountains, northern Iran, 27:TC6001, https://doi.org/10.1029/2008TC002278, 2008.

Ballato, P., Stockli, D.F., Ghassemi, M.R., Landgraf, A., Hassanzadeh, J., Friedrich, A., and Tabatabaei. S.T.: Accommodation of transpressional strain in the Arabia-Eurasia collision zone: New constraints from (U-Th)/He thermochronology in the Alborz Mountains, N Iran, Tectonics, 32, 1–18, http://doi.org/10.1029/2012TC003159, 2013.

Ballato, P., Uba, C.E., Landgraf, A., Strecker, M.R, Sudo, M., Stockli, D.F., Friedrich, A., and Tabatabaei., S.T.: Arabia-Eurasia continental collision: Insights from late Tertiary foreland-basin evolution in the Alborz Mountains, northern Iran, Geological Society of America Bulletin, 123, 106–131, http://doi.org/10.1130/B30091.1, 2011.

Borradaile, G. J.: Magnetic susceptibility, petrofabrics and strain,Tectonophysics, 156, 1-20, https://doi.org/10.1016/0040-1951 (88)90279-X, 1988.

Borradaile, G.J., and Henry, B.: Tectonic applications of magnetic susceptibility and its anisotropy, Earth-Science Review, 42, 49-93, https://doi.org/10.1016/S0012-8252(96)00044-X, 1977.

Borradaile, G.J., and Henry, B.: Tectonic applications of magnetic susceptibility and its anisotropy. Earth Science Review, 42, 49-93, https://doi.org/10.1016/S0012-8252 (96)00044-X, 1997.

Borradaile, G.J., and Tarling, D.: Strain partitioning and magnetic fabrics in particulate flow, Canadian Journal of Earth Sciences, 21, 694-697, http://doi.org/10.1139/e84-075, 1984.

Borradaile, G.J.: Magnetic fabrics and petrofabrics: their orientation distributions and anisotropies.: Journal of Structural Geology, 23, 1581–1596, https://doi.org/10.1016/S0191-8141 (01)00019-0, 2001.

Brunet, M., Korotaev, M.V., Ershov, A.V., and. Nikishin, A.M.: The South Caspian Basin: a review of its evolution from subsidence modelling, Sedimentary Geology, 156, 119-148, https://doi.org/10.1016/S0037-0738 (02)00285-3, 2002.

Brunet, M.F., Wilmsen, M., and Granath J.W.: South Caspian to Central Iran Basins, Geological Society, London, Special Publications, 312, 1-6, https://doi.org/10.1144/SP312.1, 2009.

Caricchi, C.H., Cifelli, F., Kissel, C., Sagnotti, L., and Mattei, M.: Distinct magnetic fabric in weakly deformed sediments from extensional basins and fold-and-thrust structures in the Northern Apennine orogenic belt (Italy), 35, 238-256, https://doi.org/10.1002/2015TC003940, 2016.

Cifelli, F., Ballato, P., Alimohammadian, H., Sabouri, J., and Mattei, M.: Tectonic magnetic lineation and oroclinal bending of the Alborz range: Implications on the Iran-Southern Caspian geodynamics, Tectonics, 34, 116–132, http://doi.org/ 10.1002/2014TC003626, 2015.

Cifelli, F., Mattei, M., Chadima, M., Hirt, A.M., and Hansend, A.: The origin of tectonic lineation in extensional basins: Combined neutron texture and magnetic analyses on bun deformed Q clays, Earth and Planetary Science Letters, 235, 62– 78, https://doi.org/10.1016/j.epsl.2005.02.042, 2005.

Cifelli, F., Mattei, M., Chadima, M., Lenser, S., and Hirt, A.M.: The magnetic fabric in undeformed clays: AMS and neutron texture analyses from the Rif Chain (Morocco), Tectonophysics, 466, 79–88, http://doi.org/10.1016/j.tecto.2008.08.008, 2009.

Cifelli, F., Mattei, M., Hirt, A.M., and Gunther, A.: The origin of tectonic fabrics in ‘‘undeformed’’ clays: The early stages of deformation in extensional sedimentary basins, Geophysical Research Letters, 31, L09604, https://doi.org/10.1029/2004GL019609, 2004.

Cifelli, F., Rossetti, F., Mattei, M., Hirt, A. M., Funiciello, R. and Tortorici, L.: An AMS, structural and paleomagnetic study of quaternary deformation in eastern Sicily. Journal of Structural Geology 26, 29-46, http://doi.org/ 10.1016/S0191-8141(03)00092-0, 2004.

Forte, A.M., and Cowgill, E.: Late Cenozoic base-level variations of the Caspian Sea: a review of its history and proposed driving mechanisms, Palaeogeography, Palaeoclimatology, Palaeoecology, 386, 392–407, https://doi.org/10.1016/j.palaeo.2013.05.035, 2013.

Gilder, S., Chen, Y., and Sen, S..: Oligo-Miocene magnetostratigraphy and rock magnetism of the Xishuigou section, Subei (Gansu Province, western China), and implications for shallow inclinations in central Asia, Journal of Geophysical Research, 106 (B12), 30, 505–30, 521, 2001.

Gilder, S., Chen, Y., and Sen, S.: Oligo-Miocene magnetostratigraphy and rock magnetism of the Xishuigou section, Subei (Gansu Province, western China) and implications for shallow inclinations in central Asia, Journal of Geophysical research, Solid Earth, 106, 30505-30521, https://doi.org/10.1029/2001JB000325, 2001.

Graham, J.W.: Magnetic susceptibility anisotropy, an unexploited petrofabric element, Geol. Soc. Am. Bull, 65, 1257–1258, 1954.

Graham, J.W.: Significance of magnetic anisotropy in Appalachian sedimentary rocks, Geophys. Monogr, 10, American Geophysical Union, 627–648, https://doi.org/10.1029/GM010p0627, 1996.

Guest, B., Axen, G.J., Lam, P.S., and Hassanzadeh, J.: Late Cenozoic shortening in the west-central Alborz Mountains, northern Iran, by combined conjugate strike-slip and thin-skinned deformation, Geosphere, 2, 35–52, https://doi.org/10.1130/GES00019.1, 2006a.

Hassanzadeh, J., Stockli, D. F., Horton, B. K., Axen, G. J., Stockli, L. D., Grove, M., Schmitt, A.K., and Walker, J.D.: U-Pb zircon geochronology of late Neoproterozoic- Early Cambrian granitoids in Iran: Implications for paleogeography, magmatism, and exhumation history of Iranian basement, Tectonophysics, 451, 71–96, https://doi.org/10.1016/j.tecto.2007.11.062, 2007.

Hatzfeld, D., and Molnar, P.: Comparisons of the kinematics and deep structures of the Zagros and Himalaya and of the Iranian and Tibetan plateaus and geodynamic implications, Rev. Geophys., 48, RG2005, http://doi.org/10.1029/2009RG000304, 2010.

Henry, B.: Studies of Microtectonics, Anisotropy of Magnetic Susceptibility and Paleomagnetism of the Permian Dome de Barrot (France): Paleotectonic and Paleosedimentological, Implications, Tectonophysics, 17, 61-72., https://doi.org/10.1016/0040-1951 (73)90065-6, 1973.

Housen, B.A., van der Pluijm, B.A., and Essene, E.J.: Plastic behavior of magnetite and high strains obtained from magnetic fabrics in the Parry Sound shear zone, Ontario Grenville Province, Journal of Structural Geology, 17, 265–278, https://doi.org/10.1016/0191-8141 (94) E0045-Z, 1995.

Hrouda, F., and Janak, F.: The Changes in Shape of the Magnetic Susceptibility Ellipsoid during Progressive Metamorphism and Deformation, Tectonophysics, 34, 135-148, https://doi.org/10.1016/0040-1951 (76) 90181-5, 1976.

Hrouda, F., and kahan, S.: The magnetic fabric relationship between sedimentary and basement nappes in the High Tatra Mountains, N. Slovakia, Journal of Structural Geology, 13, 681-705, https://doi.org/10.1016/0191-8141 (91) 90016-C, 1991.

Hrouda, F.: Magnetic anisotropy of rocks and its application in geology and geophysics, Surveys in Geophysics, 5, 37–82, http://doi.org/10.1007/BF014502441982, 1982.

Hrouda, F.: Magnetic anisotropy of rocks and its application to geology and geophysics, Geophysical surveys, 5, 37– 82, https://doi.org/10.1007/BF01450244, 1982.

Hrouda, F.: Magnetic Anisotropy of Rocks and its geology and Geophysics, Geophysical Surveys, 5, 37-82, http://dx.doi.org/10.1007/BF01450244, 1982.

Hrouda, F.: The Magnetic Fabric in Some Folds, Physics of the Earth and Planetary Interiors, 17, 89-97, https://doi.org/10.1016/0031-9201(78)90050-X, 1978.

Hrouda, F.: The strain interpretation of magnetic anisotropy in rocks of the Nizky, Jesenik Mountains (Czechoslovakia). Sbornik Geologickych Ved, Uzita Geofzika, 16, 27-62, 1979.

Huang, B., Piper, J.D.A., Peng, S.H., Liu, T., Li, Z.H., Wang, O., and Rixiang, Z.: Magnetostratigraphic study of the Kuche Depression, Tarim Basin, and Cenozoic uplift of the Tian Shan Range, Western China, Earth and Planetary Science Letter, 251, 346-364, http://doi.org/:10.1016/j.epsl.2006.09.020, 2006.

Jelinek, V.: Characterization of the magnetic fabrics of rocks, Tectonophysics, 79, 63–67, https://doi.org/10.1016/0040-1951 (81)90110-4, 1981.

Jelínek, V.: Statistical processing of anisotropy of magnetic susceptibility measured on groups of specimens, Studia Geophysica et Geodaetica, 22, 50–62, https://doi.org/10.1007/BF01613632 1978.

Kanamatsu, T., Herroro-Bervera, E., Taira S. Saito, A., Ashi, J., and Furumoto, A.S.: Magnetic fabric development in the Tertiary Accretionary Complex in the Boso and Miura Peninsulas of central Japan, Geophysical Research Letters, 23, 471-474, https://doi.org/10.1029/96GL00147, 1996.

Kissel, C., Barrier, E., Laj, C., and Lee, T.Q.: Magnetic fabric in undeformed marine clays from compressional zones, Tectonics 5, 769–781, https://doi.org/10.1029/TC005i005p00769, 1986.

Kligfield, R., Lowrie, W., and Dalziel, I.W.D.: Magnetic Susceptibility as a Strain Indicator in, the Sudbury Basin, Ontario, Tectonophysics, 40, 287-308, https://doi.org/10.1016/0040-1951(77)90070-1, 1977.

Kligfield, R., Lowrie, W., and Pfiffner, O.A.: Magnetic properties of deformed oolitic limestones from the Swiss Alps: the correlation of magnetic anisotropy and strain, Eclogae Geologicae Helvetiae, 75, 127–157, http://doi.org/10.5169/seals-16522, 1982.

Landgraf, A., Ballato, P., Strecker, M.R., Friedrich, A., Tabatabaei, S.H., and Shahpasandzadeh M.: Fault-kinematic and geomorphic observations along the North Tehran Thrust and Mosha Fasham

Fault, Alborz mountains, Iran: implications for fault-system evolution and interaction in a changing tectonic regime, Geophysical Journal International, 177, 676-690, https://doi.org/10.1111/j.1365-246X.2009.04089.x, 2009.

Lee T., and Angelier J.: Tectonic significance of magnetic susceptibility fabrics in Plio-Quaternary mudstones of southwestern foothills, Taiwan, Earth, Planets and Space, 52, 527-538, http://doi.org/10.1186/BF03351660, 2000.

Madanipour, S., Ehlers, T.A., Yassaghi, A. and E. Enkelmann, E.: Accelerated middle Miocene exhumation of the Talesh Mountains constrained by U-Th/He thermochronometry: Evidence for the Arabia-Eurasia collision in the NW Iranian Plateau, Tectonics, 36, 1538-1561. https://doi.org/10.1002/2016TC004291, 2017.

Madanipour, S., Ehlers, T.A., Yassaghi, A., and Enkelmann, E.: Accelerated middle Miocene exhumation of the Talesh Mountains constrained by U-Th/He thermochronometry: Evidence for the Arabia-Eurasia in the NW Iranian Plateau, Tectonics, 36, 1538-1561, https://doi.org/10.1002/2016TC004291, 2017.

Madanipour, S., Yassaghi, A., Ehlers, T.A., and Enkelmann, E.:Tectonostratigraphy, structural geolmetry and kinematics of the NW Iranian Plateau: Insights from the Talesh Mountainas, Iran, American Journal of Science, 318, 208-245, http://doi.org/10.2475/02.2018.02, 2018.

Martin-Hernandez, F., Lüneburg, C., Aubourg, C., and Jackson, M.: Magnetic Fabrics: Methods and Applications. Geological Society, London, Special Publication, 238, 1-7, http://doi.org/10.1144/GSL.SP.2004.238. 01.13, 2004.

Mattei, M., Sagnotti, L., Faccenna, C., and Funiciello, R.: Magnetic fabric of weakly deformed clay-rich sediments in the Italian peninsula: relationship with compressional and extensional tectonics, Tectonophysics, 271, 107–122, https://doi.org/10.1016/S0040-1951 (96)00244-2, 1997.

McQuarrie, N., and van Hinsbergen, D.J.J.: Retrodeforming the Arabia-Eurasia collision zone: Age of collision versus magnitude of continental subduction, Geology, 41, 315–318, https://doi.org/10.1130/G33591.1, 2013.

Mouthereau, F., Lacombe, O., and Vergés, J.: Building the Zagros collisional orogen: Timing, strain distribution and the dynamics of Arabia/Eurasia plate convergence, Tectonophysics, 532–535, 27–60, http://doi.org/10.1016/j.tecto.2012.01.022, 2012.

Oliva-Urcia, B., Larrasoana, J.C., Pueyo, E.L., Gil, A., Mata, P., Pares, J.M., Schleicher, A.M., and Pueyo, O.: Disentangling magnetic subfabrics and their link to deformation processes in cleaved sedimentary rocks from the Internal Sierras (west central Pyrenees, Spain), Journal of Structural Geology, 31, 163–176, http://doi.org/ 10.1016/j.jsg.2008.11.002, 2009.

Parés, J.M., and Van Der Pluijm, B.A.: Evaluating magnetic lineations (AMS) in deformed rocks, Tectonophysics, 350, 283–298, http://dx.doi.org/10.1016/S0040-1951 (02)00119-1, 2002.

Pares, J.M., van der Pluijm, B.A. and Dinar es-Turell, J.: Evolution of`magnetic fabrics during incipient deformation of mudrocks (Pyrenees, northern Spain), Tectonophysics, 307, 1–14, https://doi.org/10.1016/S0040-1951 (99)00115-8, 1999.

Parés, J.M.: How deformed are weakly deformed mud rocks? Insights from magnetic magnetic anisotropy, Geological Society London Special Publications, 238, 191-203, http://doi.org/ 10.1144/GSL.SP.2004.238.01.13, 2004.

Rashid, H., Cifelli, F., and Mattei, M.: Late folding-related magnetic foliation in the active Ferdows (northeastern Iran) thrust–fold system; Journal of Asian Earth Sciences, 108, 48–57, https://doi.org/10.1016/j.jseaes.2015.04.023, 2015.

Reuter, M., Piller, W.E., Harzhauser, M., Mandic, O., Berning, B., Rögl, F., Kroh, A., Aubry, M., Wielandt-Schuster,U., and Hamedani, A.: The Oligo-Miocene Qom Formation (Iran): Evidence for an early Burdigalian restriction of the Tethyan Seaway and closure of its Iranian gateways, International Journal of Earth Sciences, 98, 627–650, http://doi.org/10.1007/s00531-007-0269-9, 2009.

Rezaeian, M., Carter, A., Hovious, N., and Allen, M.: Cenozoic exhumation history low-temperature chronometry, Tectonics, 31, TC2004, http://doi.org/ 10.1029/2011TC002974, 2012.

Rieben, H.: the geology of the Tehran plain: American Journal of Science, 253, 617–639, http://doi.org/10.2475/ajs.253.11.617 1955.

Robion, P., Grelaud, S., and Frizon de Lamotte, D.: Pre-folding magnetic fabrics in foldand-thrust belts: Why the apparent internal deformation of the sedimentary rocks from the Minervois basin (NE-Pyrenees, France) is so high compared to the Potwar basin (SW — Himalaya, Pakistan)? Sediment, Geol, 196, 181–200, https://doi.org/10.1016/j.sedgeo.2006.08.007, 2007.

Sagnotti, L., and Speranza, F.: Magnetic fabric analysis of the Plio-Pleistocene clayey units of the Sant'Arcangelo basin, southern Italy, Physics of the Earth and Planetary Interiors, 77, 165-176, ttps://doi.org/10.1016/0031-9201(93)90096-R,1993.

Sagnotti, L., Mattei, M., Faccenna, C., and Funiciello, R.: Paleomagnetic Evidence for No Tectonic Rotation of the Central Tyrrhenian Margin since Upper Pliocene, Geophysical Research Letters, 21, 481-484, https://doi.org/10.1029/94GL00393, 1994.

Sagnotti, L., Speranza, F., Winkler, A., Mattei, M., and Funiciello, R.: Magnetic fabric of clay sediments from the external northern Apennines (Italy), Physics of the Earth and Planetary Interiors, 105, 73–93, https://doi.org/10.1016/S0031-9201 (97)00071-X, 1998.

Saint-Bezar, B., Hebert, R.L., Aubourg, C., Robion, P., Swenen, R., and Frizon de Lamotte, D.: Magnetic fabric and petrographic investigations of hematite-bearing sandstones within ramp-related folds: examples from the South Atlas Front (Morocco), J. Struct. Geol, 24, 1507–1520, http://dx.doi.org/10.1016/S0191- 8141(01)00140-7, 2002.

Salvini, F., Billi, A., and Wise, D.U.: Strike-slip fault-propagation cleavage in carbonate rocks: The Mattinata Fault zone, southern Apennines, Italy, Journal of Structural Geology, 21, 1731 –1749, https://doi.org/10.1016/S0191-8141(99)00120-0, 1999.

Soto, R., Larrasoańa, J.C., Arleguí, L.E., Beamud, E., Oliva-Urcia, B. and Simón, J.L.: Reliability of magnetic fabric of weakly deformed mudrocks as a palaeostress indicator in compressive settings, Journal of Structural Geology, 31, 512-522, http://doi.org/10.1016/j.jsg.2009.03.006, 2009.

Storti, F., Rossetti, F., Läufer, A.L., and Salvini, F.: Consistent kinematic architecture in the damage zones of intraplate strike-slip fault systems in North Victoria Land, Antarctica and implications for fault zone evolution, Journal of Structural Geology, 28, 50–63, https://doi. org/10.1016/j.jsg.2005.09.004, 2005.

Tarling, D. H., and Hrouda, F.: The Magnetic Anisotropy of Rocks, Chapman & Hall, London, 217 p, https://doi.org/10.1002/gj.3350300111, 1995.

Verdel, C., Wernicke, B.P., Hassanzadeh, J., and Guest, B.: A Paleogene extensional arc flare-up in Iran, Tectonics, 30, TC3008, https://doi.org/10.1029/2010TC002809, 2011.

Zanchi, A., Zanchetta, S., Berra, F., Mattei, M., Garzanti. E., Molyneux, S., Nawab, A., and Sabouri, J.: The Eo-Cimmerian (Late? Triassic) orogeny in North Iran, Geological Society, London, Special Publication, 312, 31-55, https://doi.org/10.1144/SP312.3, 2009.

A3. References of chapter 4:

Bilardello, D., and Jackson, M.: What do the Mumpsies do?, The IRM Quarterly (fall), 23, 2013.

Day, R., Fuller, M., and Schmidt, V.A.: Hysteresis properties of titanomagnetites: grain size and composition dependence, Physics of the Earth and Planetary Interiors 13, 260–267, 1977.

Deng, C., Zhu, R., Verosub, K.L., Singer, M.J. and Vidic, N.J.: Mineral magnetic properties of loess/paleosol couplets of the central loessplateau of China over the last 1.2 Myr,J, Geophys. Res., 109, B01103, 2004.

Dunlop, D.J. and Özdemir, Ö. : Rock Magnetism Fundamentals and Frontiers, Geological Magazine, Cambridge University Press, Cambridge, 135, 287-300, 1977.

Dunlop, D.J.: Theory and application of the day plot (Mrs/Ms versus Hcr/Hc): 1. Theoretical curves and tests using titanomagnetite data, Journal of Geophysical Research, 107, 2002.

Heslop, D., Roberts, A.P., Chang, L., Davies, M., Abrajevitch, A., and Deckker, P.D.: Quantifying magnetite magnetofossil contributions to sedimentary magnetizations, Earth and Planetary Science Letters, 382, 58–65, 2013.

Maher, B.: Environmental magnetism and climate change, Contemporary Physics, 48, 247-274, 2007.

Moreno, E., Thouveny, N., Delanghe, D., Mccave, N., and Shackleton, N.J.: Climatic and oceanographic changes in the Northeast Atlantic reflected by magnetic properties of sediments deposited on on the Portuguese Margin during the last 340 Ka, Earth and Planetary Science Letters, 202, 465-480, 2002.

Roberts, A.P., Cui, Y., and Verosub, K.L.: Wasp-waisted hysteresis loops: Mineral magnetic characteristics and discrimination of components in mixed magnetic systems. Journal of Geophysical Research, 100, 17909–17924, 1995.

Tauxe, L., Herbert, T., Shackleton, N.J., and Kok, Y.S.: Astronomical calibration of the Matuyama–Brunhes boundary: consequences for magnetic remanence acquisition in marine carbonates and the Asian loess sequences, Earth and Planetary Science Letters 140, 133–146, 1996.

Tauxe, L., Neal Bertram, H., and Seberino, C.: Physical interpretation of hysteresis loops: Micromagnetic modeling of fine particle magnetism, Geochemistry Geophysics, Geosystems, 3, 1-22, 2002.

Wang, D., Van der Voo; R.: The hysteresis properties of multidomain magnetite and titanomagnetite/titanomaghemite in mid-ocean ridge basalts, Earth and Planetary Science Letters, 220, 175-184, 2004.

Yu, Y., and Tauxe, L.: on the use of magnetic transient hysteresis in paleomagnetism for granulometry, Geochemistry Geophysics Geosystems, 60, 2005.

Zan, j., Fang, X., Yang, S.H., and Yan, M.: Bulk particle size distribution and magnetic properties of particle-sized fractions from loess and paleosol samples in Central Asia, Geochemistry Geophysics Geosystems, 16, 101-111, 2015.

APPENDIX

In the following we provide a detailed description of the analytical procedures for each methodology used in this thesis. Furthermore we provide the raw data in form of tables and figures.

A1. Zircon U-Pb-dating

Mineral separation was performed according to standard techniques (crushing, sieving, water table, magnetic separation and heavy liquids as needed) at the Institute of Earth and Environmental Science of the University of Potsdam. Zircons grains where sent to the the Geochronology Laboratory in the Department of Earth and Space Sciences, University of California Los Angeles for the sample preparation and the laboratory measurements. Epoxy grain mounts of hand-selected zircons were gently ground to expose grain interiors and were given final polish with 1 µm diamond. After ultrasonic cleaning, grains were surveyed for internal compositional zonations and/or inclusions via cathodoluminescence (CL) imaging. Mounts were then coated with ~100 Å of Au. U-Pb ages were determined based on U, Pb, and Th isotopic spot measurements using the UCLA CAMECA ims 1270 ionprobe following the analytical procedure explained in Schmitt et al. (2003). Each analytical run collected data for ten cycles, and age calculations were performed by means of ISOPLOT (Ludwig, 2003). The final ages listed in Table 3 of chapter 2 represent the weighted mean at the 95% confidence level for a given number of aliquots ranging from two to seven (Figure A1.1; Mahon, 1996).

References

Ludwig, K.R., 2003, User’s Manual for Isoplot/Ex, A geochronological toolkit for Microsoft Excel Berkeley Geochronology Center Special Publication, v. 4, Berkeley Geochronology Center, 2455 Ridge Road, Berkeley, CA 94709, USA.

Schmitt, A.K., Grove,M., Harrison, T.M., Lovera, O.M., Hulen, J. & Waters, M. (2003) The Geysers–Cobb Mountain magma system, California (Part 1): U-Pb zircon ages of volcanic rocks, conditions of zircon crystallization and magma residence times. Geochimica et Cosmochimica Acta, 67, 3423–3442.

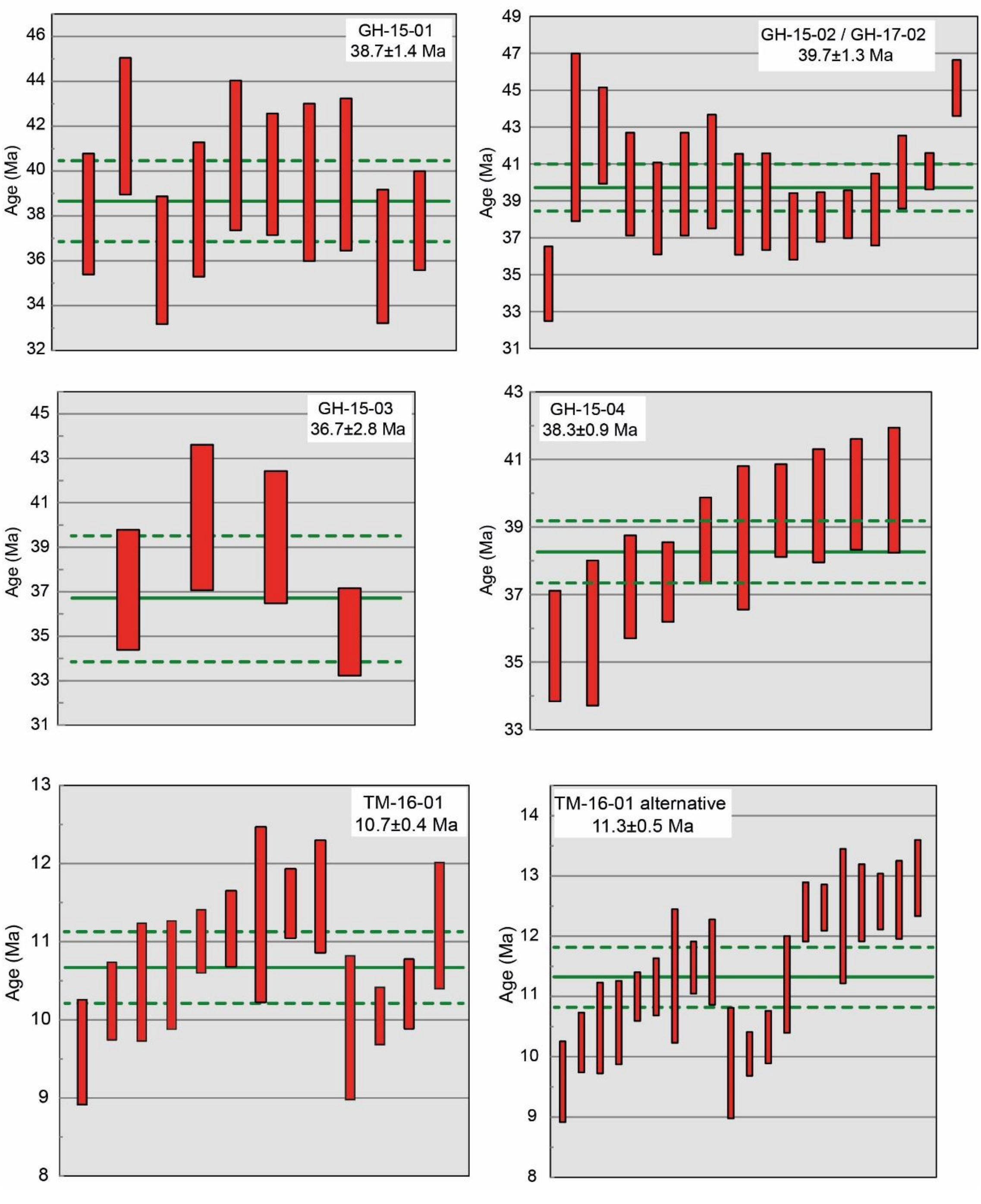

Figure A1.1: Weighted averages for the analyzed samples shown with a green lines and associated error (in two sigmas) in a dashed green line. The red boxes display the raw data of selected grains (2 sigma error). For sample TM-16-01, two possible solutions are shown (see chapter 2, section geochronology for details).

A2. Zircon U-Pb-dating

A total of 539 oriented samples were collected from the three investigated stratigraphic section (TV, GH and KA section) for a combined stratigraphic thickness of 1185 m. The mean sampling interval is typically ~. 3m with at least two cores at each site. In case of poor outcrop conditions or in sectors composed mostly of coarse-grained sediments the sampling intervals was as large as ∼ 5-6 m. All the samples were cored with a portable gasoline-powered drill. The orientations of the cores were measured by using a magnetic compass to determine both azimuth of core axis (declination) and dip of the core axis (inclination) and also corrected for ~ 5^0 E present day declination using magnetic field calculators (www.ngdc.noaa).

Magnetic measurements were then performed using a 2-G Enterprises superconducting rock magnetometer equipped with DC-SQUID coils within a magnetically shielded room at the Alpine Laboratory of Palaeomagnetism (ALP) in Peveragno and at the laboratory of Paleomagnetism and Environmental Magnetism of the Institute of Geophysics and Volcanology (INGV) in Rome, both in Italy. After measuring the Normal Remanent Magnetization (NRM), samples were subjected to stepwise (up to 15 steps) thermal demagnetization, using heating routine increments (150°C up to a temperature of 480°C and 30–50°C increments above 480°C) until the signal decreased below the instrumental detection limit or random changes of the paleomagnetic directions occurred. A set of sister specimens were chosen for AF demagnetization. Stepwise alternating field (AF) demagnetizations were done using a three-axis demagnetizer with a maximum field of up to 100/120 mT, coupled with a 2G–DCSQUID magnetometer. Data processing was conducted by means of Rema soft program and led to the isolating the stable polarity directions of the characteristic remanent magnetization (ChRM) by using the principal component analysis (Kirschvink, 1980), data statistical analysis by means of Fisher statistics (Fisher, 1953), and finally the calculation of the Virtual Geomagnetic Pole (VGP) from the ChRM vectors.

References

FISHER, R.A. (1953) Dispersion on a sphere, Proceedings of the Royal Society of London, Series A, 217, 295–305.

KIRSCHVINK, J.L. (1980) the least-squares line and plane and the analysis of palaeomagnetic data, Geophysical Journal of the Royal Astronomical Society, 62, 699-718.

A3. Sandstone petrography

Six sandstone samples collected from the KA and GH sections in the Tarom basin were analyzed under a polarized microscope in transmitted light. (Table A3.1). In each sample, 400 points were counted by using the Gazzi-Dickinson method (Ingersoll et al. 1984) The results of the modal analysis are plotted in the ternary diagrams of Garzanti (2019) and Dickinson (1985) in order to identify the local tectonic setting and the sediment provenance area (Table 1; see also Figure 12 of chapter 2).

	QFL; Garzanti (2019)			QtFL-c; Dickinson (1985)		
Sample Number	Q	F	L	Qt	F	L-c
KA-16-02	5	31	64	4	32	64
KA-16-04	1	27	72	1	27	72
KA-16-05	5	20	75	5	20	75
GH-16-01	9	10	81	13	12	75
GH-16-09	11	5	83	15	7	78
GH-16-10A	13	4	83	15	4	81

Table A3.1: Sandstone composition of the KA and GH stratigraphic studied sections in the Tarom Basin. (1) QFL by Garzanti (2019); (Q) Total quartz grains (Qm = monocrystalline + Qp = polycrystalline), (F): Total feldspar grains (P = plagioclase + K-feldspars), (L) Total lithic fragments. (2) QtFL- by Dickinson (1985); (Qt) Total quartzose grains (Qm + Qp), (F) Total feldspar grains (P + K), L-c: Total lithic fragments (excluding carbonates).

Sample Number	Lm	Lv	Ls
KA-16-02	5	89	6
KA-16-04	6	93	1
KA-16-05	7	88	5
GH-16-01	20	39	41
GH-16-09	20	13	67
GH-16-10A	36	17	47

Table A3.2: Lm-Lv-Ls ternary plot for the Tarom basin (Lm = metamorphic; Lv = volcanic; Ls = sedimentary).

References

DICKINSON., W.R. (1985) Interpreting provenance relations from detrital modes of sandstones. In: Zuffa, G.G. (Ed.), Provenance of arenites. Reidel, Dordrecht, NATO ASI Series, 148, 333–361.

GARZANTI., E.D. (2019) Petrographic classifiation of sand and sandstone. Earth-Science Reviews, 192, 545–563.

INGERSOLL, R.V., BULLAED, T.F., FORD, R.L., GRIMM, J.P., PICKLE, J.D. & SARES, S.W. (1984) the effect of grain size on detrital modes: a test of the Gazzi–Dickinson point-counting method. Journal of Sedimentary Petrology, 54, 103 –116.